Development of new cryogenic detectors to extend the physics reach of the CRESST experiment

Elia Bertoldo

München 2020

Development of new cryogenic detectors to extend the physics reach of the CRESST experiment

Elia Bertoldo

Dissertation
an der Physik
der Ludwig–Maximilians–Universität
München

vorgelegt von
Elia Bertoldo
aus Schio

München, den 29.10.2020

The work presented in this thesis was carried out in the CRESST group at the Max Planck Institut für Physik (Werner-Heisenberg-Institut)

Erstgutachter: Prof. Dr. Otmar Biebel
Zweitgutachter: Prof. Dr. Wolfgang Dünnweber
Tag der mündlichen Prüfung: 14.12.2020

Contents

Zusammenfassung

Die umfangreiche Präsenz Dunkler Materie ist eines der größten ungelösten wissenschaftlichen Rätsel unserer Zeit. Es lässt sich auf kosmologische und astronomische Beobachtungen zurückführen, die zwar die Existenz von Dunkler Materie belegen, jedoch keinen Aufschluss über ihre Natur liefern. Es ist lediglich bekannt, dass diese unsichtbare Materie gravitativ mit herkömmlicher Materie wechselwirkt. Einer der aktuellen Ansätze versucht daher dunkle Materie durch Teilchenphysik als aus einem oder mehreren Elementarteilchen zusammengesetzt zu erklären. Jedoch kann die Teilchenphysik keine offensichtliche Lösung anbieten, da keines der zum heutigen Zeitpunkt bekannten Teilchen als Hauptbestandteil Dunkle Materie in Frage kommt.

Zahlreiche Theorien machen Vorhersagen über die Existenz bisher unentdeckter Teilchen, welche als Lösung des Rätsels um die dunklen Materie dienen könnten. Die Bandbreite möglicher Massen und Interaktionen dieser Teilchen ist enorm. Da es keine Gründe gibt, ein mögliches Teilchen einem anderen Teilchen als Erklärung vorzuziehen, ist der einzige realistische Weg zur Entdeckung die Konzeption verschiedener Experimente, die möglichst viele der in Frage kommenden Kandidaten abdecken.

Eines der erfolgreichsten Experimente, das sich an der Suche nach solchen hypothetischen Teilchen Dunkle Materie beteiligt, ist CRESST. Das Experiment verwendet hoch-sensitive kryogene Detektoren, die auf die Detektion von Teilchen dunkler Materie, welche die Erde erreichen, ausgerichtet sind. Die Grundidee besteht darin, dass die Teilchen schlussendlich mit einem der Detektoren in einem unterirdischen Labor auf der Erde interagieren können und so eine schwache Spur hinterlassen. Zum jetzigen Zeitpunkt befindet sich CRESST in der dritten Phase der experimentellen Suche, CRESST-III, und verwendet szintillierende $CaWO_4$ Kristalle in Verbindung mit supraleitenden Thermometern.

In den letzten Jahrzehnten lag der Fokus von CRESST vor allem darauf, eine bestimmte Art von Wechselwirkungen zwischen dunkler und herkömmlicher Materie zu untersuchen, welche als spin-unabhängig bezeichnet werden. Dennoch hat CRESST in den vergangenen Jahren eine innovative Technik entwickelt, die einen breiteren Bereich an Wechselwirkungen in der Astroteilchenphysik zur Erforschung eröffnet hat. Eine der naheliegenden Erweiterungen für die Suche nach Dunkler Materie durch CRESST ist die Untersuchung von spin-abhängigen Interaktionen, was durch die Verwendung anderer Detektorkristalle erreicht werden kann. Darüber hinaus können die von CRESST entwickelten supraleitenden Thermometer für die Untersuchung nahezu jedes physikalischen Phänomens verwendet werden, wenn ein niedriger Energieschwellenwert sowie eine hohe Energieauflösung erforderlich ist. Eine Anwendung von CRESST-ähnlichen Thermometern ist die Suche nach solaren Axionen mit Hilfe von geeigneten Detektorkristallen.

In der vorliegenden Arbeit beschäftigt sich Kapitel 1 mit den kosmologischen Fragestellungen, die durch dunkle Materie im Universum entstehen. Besonderes Augenmerk liegt auf dem Nachweis der Existenz Dunkler Materie und der Interpretation ihrer Natur. Besondere Bedeutung wird hier den Argumenten für die Existenz von Dunkle-Materie-Teilchen sowie möglichen Kandidaten, die diese Rolle im Universum einnehmen könnten, zugewiesen. Kapitel 2 gibt einen kurzen Überblick über die experimentellen Methoden zur Untersuchung Dunkler Materie im Falle der Teilcheninterpretation, insbesondere Experimente zur direkten Suche Dunkler Materie. Kapitel 3 ist kryogenen Detektoren, welche oft bei der Suche nach Dunkler Materie sowie im gesamten Feld der Astroteilchenphysik Anwendung finden, gewidmet. Nach einer generellen Beschreibung wird der Leser in die Detektoren von CRESST-III eingeführt, da ein Großteil der Arbeit in dieser Dissertation mit ähnlichen Detektoren durchgeführt wurde.
Die vorliegende Arbeit stellt eine kumulative Disseration dar. Somit bestehen Kapitel 4-7 aus Artikeln, welche in Peer-Review-Fachzeitschriften veröffentlicht wurden. Kapitel 4 und 5 beschäftigen sich mit der Erforschung des Parameterraums für spinabhängige Wechselwirkung Dunkler Materie mit Lithium-enthaltenden Kristallen. Der erste Artikel in Kapitel 4 stellt die physikalischen Ergebnisse vor, die mit einem Li_2MoO_4 Kristall erzielt werden konnten. Li_2MoO_4 findet als Absorber in vielen kryogenen Detektoren Anwendung. In Kapitel 5 konnten diese wissenschaftlichen Ergebnisse durch den Einsatz von neu entwickelten kryogenen Detektoren, welche $LiAlO_2$ verwenden, noch weiter verbessert werden. Jedoch stellte $LiAlO_2$ zum damaligen Zeitpunkt einen neuartigen Typ von Absorber für kryogene Detektoren dar, weswegen eine umfangreiche kryogene Charakterisierung notwendig war, um die Eigenschaften des Kristalls zu verstehen.

Kapitel 6 und 7 befassen sich dagegen mit der Entwicklung eines kryogenen Detektors, welcher speziell für die Untersuchung der resonanten Absorption von solaren Axionen durch ^{169}Tm entworfen worden ist. In Kapitel 6 werden die ersten Untersuchungen der kryogenen Eigenschaften eines $Tm_3Al_5O_{12}$ Kristalls vorgestellt. In Kapitel 7 werden neue kompetitive Grenzen für die Kopplungskonstanten zwischen Axionen und Elektronen beziehungsweise Photonen hergeleitet, die erzielt werden konnten, indem der selbe Thulium-enthaltenden Kristall mit einem empfindlicheren Thermometern verwendet wurde.
Abschließend fasst Kapitel 8 die vorgestellten Ergebnisse zusammen und bietet Perspektiven in den beiden zuvor diskutieren Forschungsansätzen.

Abstract

The vast presence of dark matter in the Universe is nowadays one of the biggest unresolved mysteries of science. The dark matter problem stems from cosmological and astronomical observations which, however, do not provide any information about the nature of dark matter. The only broad information is that this invisible matter interacts gravitationally with ordinary matter. As such, one of the ongoing attempts is to solve this problem through particle physics, meaning that dark matter would be composed by one or more elementary particles. Unfortunately, there is not an obvious solution offered by particle physics, since none of the particles known today can be the main component of dark matter.
There are multiple theories predicting the existence of particles not yet discovered which would solve the dark matter puzzle: these particles can have a vast range of masses and interactions with ordinary matter. Since there is no reason to favor a particle candidate over another, the only realistic path to a discovery is to realize a range of different experiments that can investigate as many of these candidates as possible.
One of the most successful experiments involved in the search for hypothetical dark matter particles is CRESST. This experiment employs extremely sensitive cryogenic detectors aimed at detecting dark matter particles reaching Earth. The idea is that these dark matter particles can eventually interact with one of the detectors placed inside an underground laboratory on Earth, leaving a feeble trace. Nowadays, CRESST is in its third generation of experimental search, CRESST-III, and employs scintillating $CaWO_4$ crystals instrumented with superconducting thermometers.
In the past decades, CRESST has mostly focused on probing a specific type of interactions between dark matter particles and ordinary matter, called spin-independent interactions. However, CRESST in the years has developed a cutting-edge technology which allows the exploration of a wider range of interactions in astroparticle physics. One of the straightforward expansion of the CRESST dark matter search is the investigation of spin-dependent interactions, which can be performed with the adoption of different target crystals. Furthermore, the superconducting thermometers developed by CRESST can be used to probe almost any physical phenomenon that requires a low energy threshold in combination with a high energy resolution. One of the application of CRESST-like thermometers is the search of solar axions employing a suitable target crystal.

In this thesis, Chapter 1 is dedicated to the cosmological problem posed by dark matter in the Universe with special focus on the evidence of the existence of dark matter and the interpretations of its nature. Particular relevance is given to the case of the existence of a dark matter particle and the plausible candidates to fill this role. Chapter 2 briefly explores the experimental techniques used to study dark matter in the case of the particle interpretation, with special focus on

direct search experiments. Chapter 3 is dedicated to the description of cryogenic detectors, which are widely used in the field of dark matter search and in the whole field of astroparticle physics. After a general description, CRESST-III detectors are introduced, since most of the original work of this thesis was carried out employing detectors of a similar type.
This thesis is presented in the form of a cumulative thesis. As such, Chapters 4–7 are articles published in peer reviewed journals. Chapter 4 and 5 are dedicated to the exploration of the parameter space for spin-dependent dark matter interactions with lithium-containing crystals. The first paper, presented in Chapter 4, is dedicated to the results obtained with a Li_2MoO_4 crystal, a widely used absorber for cryogenic detectors. In Chapter 5, the physics results obtained with Li_2MoO_4 were improved thanks to the development of a new cryogenic detector employing $LiAlO_2$. However, $LiAlO_2$ was a novel type of absorbers for cryogenic detectors, so it was also necessary to carry out an extensive cryogenic characterization to understand the properties of the crystal.
Chapter 6 and 7 are instead dedicated to the development of a cryogenic detector designed to study the resonant absorption of solar axions by ^{169}Tm. In Chapter 6, the first test of the cryogenic properties of a $Tm_3Al_5O_{12}$ crystal is presented. In Chapter 7 new competitive limits on the axion coupling constants to electrons and photons are derived, after the same thulium-containing crystal used in Chapter 6 was instrumented with a more sensitive thermometer.
Finally, in Chapter 8 the conclusions are drawn along with some future perspectives on the two lines of research presented before.

Chapter 1

Dark matter

Since 1933 many scientists have tried to find a final answer to a pressing problem: the apparent presence in the Universe of invisible matter, commonly known as *dark matter*. The quest nowadays is still ongoing and, even if pieces of evidence about the dark matter existence have piled up in the last decades, there is still no consensus about its nature.
Most of the developed theories point towards a particle not included in the Standard Model of Particle Physics (SM). Indirect observations show that these hypothetical particles interact gravitationally with ordinary matter. The complexity of this puzzle is even enhanced by the fact that many scientists speculate that the effects attributed to dark matter could be instead caused by something different than an unidentified particle.

In this chapter a short introduction about the evidence of dark matter and the theories about its nature will be presented, with a primary focus on the hypothesis regarding the abundant presence of a mysterious particle in the Universe.

1.1 A brief history of the dark matter concept

Fritz Zwicky was arguably the pioneer of dark matter research: in 1933 he was studying the redshift of numerous galaxies, when he noticed a large velocity dispersion in the Coma Cluster. Zwicky used the virial theorem to calculate the total mass of the cluster, the potential energy, the average kinetic energy of galaxies inside the cluster, and finally the resulting velocity dispersion: the calculated velocity dispersion was around 80 km/s, while the observed was much higher, around 1000 km/s. This discrepancy led Zwicky to the following conclusion: "*If this would be confirmed, we would get the surprising result that dark matter is present in much greater amount than luminous matter.*" [1, 2], where with dark matter he meant "*cool and cold stars, macroscopic and microscopic solid bodies, and gases*" inside the cluster [2, 3]. It is evident that Zwicky was quite far from the way we currently think about dark matter, despite seeing for the first time a piece of evidence we still take into account today. This, we will see, is a recurrent situation in this field of research: even if there is a common ground for the evidence, the interpretation of it vary immensely.
In 1936, another astronomer, Sinclair Smith, found similar discrepancy when studying the Virgo Cluster and himself too concluded that there should have been "*internebular material, either uniformly distributed or in the form of great clouds of low*

luminosity surrounding the [galaxies]" [4] to explain the anomalous mass-to-light ratio. In the following decades many astronomers debated the validity of these results and many other tried to solve the mystery, but it was with the results published by Vera Rubin and Kent Ford in 1970 [5] that finally the idea of a vast presence of dark matter in the Universe started to catch on.
The two astronomers measured the rotation curve, i.e. the orbital speed of visible stars versus their distance from the center of the galaxy, of Andromeda, a spiral galaxy close to the Milky Way. At large distances from the center there was the expectation that the velocities of visible objects would start to decrease, since most of the mass was concentrated in the center of the galaxy, but the data showed otherwise, with flat rotation curves even at large distances; further measurements highlighted the same pattern in numerous galaxies [6]. At this point, many options were considered to explain the astronomical observations and the scientific community mostly focused on large bodies, such as faint stars, black holes, and comets [7].
The first shift of focus from astronomical bodies to particles took place in the 70s, when neutrinos were for the first time scrutinized as a possible dark matter candidate [8, 9]. These were isolated attempts inside a broader debate which was revolving around the cosmological role of neutrinos [10, 11, 12, 13, 14, 15, 16]. During that era of excitement it did not take too long to finally adopt neutrinos as a legitimate explanation for dark matter [17], especially after the imprecise estimation of the electron-neutrino mass from an experiment measuring the beta spectrum end point of tritium ($m_{\nu_e} \sim 30\,\text{eV}$) [18]. This is another general trend in dark matter research: the debate has a very fast pace and the competition is quite high both in the theoretical formulation and the experimental research.
During the 80s it was already becoming clear that Standard Model neutrinos were likely not the right candidate to constitute the majority of dark matter because of cosmological constraints [19]. Nevertheless, the idea that dark matter was composed by an elusive particle not included in the Standard Model was set. In 1981, Heinz Pagels and Joel Primack speculated that it could be the gravitino, a new particle predicted by Supersimmetry [20], while in 1993, Scott Dodelson and Lawrence Widrow theorized the existence of a sterile neutrinos to solve the dark matter problem [21]. The development of Supersimmetry was in particular very relevant for the research carried out in the last 30 years. With the advent of the Minimal Supersymmetric Standard Model (MSSM) [22], four particles generally known as neutralinos gained most of the attention from the community. Another candidate under the spotlight in the last decades is the axion, a hypothetical particle introduced in 1977 to solve the strong CP problem in Quantum Chromodynamics (QCD) [23, 24, 25, 26]. Nowadays, the list of different hypothetical particles is long and some of them are presented more extensively in Section 1.5.
The reader should always keep in mind that, while most of the community believes the dark matter is constituted by one or more elusive particles, other plausible theories solving the dark matter mystery involve the vast presence of Primordial Black Holes in the Universe [27, 28] or a reformulation of gravitational laws [29].

1.2 The ΛCDM model

The core idea of an expanding Universe was introduced for the first time by Georges Lemaitre in 1927 [30, 31]. The idea was then developed into more structured models

in the 40s by George Gamow and collaborators [32, 33]. In these first cosmological models, the key idea of a Big Bang and a following Big Bang Nucleosynthesis (BBN) are already present. In 1981, Alan Guth expanded what was called *the standard model of hot big-bang cosmology* proposing the Inflation [34], a sudden exponential expansion of the early Universe. At this point, most of the history of the Universe was already outlined. In the last decades of the 20th century, a standard model of cosmology was developed, thanks to new data and updated theories. Nowadays, we commonly refer to this model as the ΛCDM model. However, there were two key additions that were missing in the first cosmological models: dark matter and dark energy. In fact, it became more and more evident that to explain multiple cosmological observations pure-baryonic models were insufficient. This is also reflected in the name of the model, Λ being the cosmological constant expressing the energy density of the space linked to dark energy and CDM referring to Cold Dark Matter, whose existence is postulated by the model.
This model relies on a set of six minimal independent parameters: the baryon density $\Omega_b h^2$, the cold dark matter density $\Omega_c h^2$, the optical depth τ, the perturbation amplitude $\ln(10^{10} A_s)$, the observed angular size of the sound horizon at recombination $100\theta_{MC}$, and the scalar spectra index n_s [35, 36]. The other cosmological parameters of interest, such as the Hubble constant or the dark energy density, can be promptly derived from these base parameters. It has to be noted that the model itself is based on the presence of dark matter and dark energy on a purely quantitative way, but tells very little about their nature.

Albeit we do not know the microphysics of dark matter, we know that it has to still hold some macroscopic properties to properly fit well in the ΛCDM model [37]:

- It is *dark*, meaning that is does not emit electromagnetic radiation.
- It is *cold*, meaning that it was nonrelativistic at the time when galaxies started to form.
- It does not interact with ordinary matter through any known interaction but the gravitational one and, possibly, the weak interaction.
- It has to be stable, meaning that the minimum requirement is that it should have a lifetime larger than the age of the Universe or, in other words, that it is observationally stable.
- Interactions within the dark matter sector have to be suppressed.

1.3 Evidence of dark matter

Having introduced the most widely accepted cosmological model, in this section the data on which it is based upon will be presented, with particular emphasis on the evidence pointing at the presence of dark matter in the Universe.
For conciseness, some other important observations will be omitted, such as the Bullet Cluster [38, 39], the Lyman-alpha forest [40], and the gravitational lensing of galaxy clusters [41, 42], .

1.3.1 Temperature anisotropies of the Cosmic Microwave Background

In 1965 Penzias and Wilson published the first observation [43] of an isotropic noise caused by a residual photon background with a ∼3 K temperature. This is the first evidence of the Cosmic Microwave Background (CMB), which permeates the Universe. Nowadays, CMB is one of the most powerful cosmological probes and arguably the strongest evidence supporting the presence of dark matter in the Universe. CMB radiation originated ∼380 Ky after the Big Bang, when Thomson scatterings between photons and electrons started to become ineffective due to the sharp drop in the free electron density [44]. Contrary to what was inferred from the first observations, CMB is actually not perfectly isotropic, but presents temperature anisotropies, see Figure 1.1. These anisotropies store a relevant amount of cosmological information, which was brought to light thanks to a series of precision measurements carried out by various satellite experiments such as COBE [45], WMAP [46], and PLANCK [35].

Before what is defined as *the time of the last scattering*, the Universe was made of a plasma mostly containing photons, electrons, and baryons. Photons were coupled with electrons via Thomson scatterings and electrons were coupled with baryons via Coulomb interactions. Once the temperature of the Universe fell to a level where the electrons and protons could bind to form neutral atoms, matter and radiation decoupled. At this point, photons could propagate freely and we still observe them today as a snapshot of the early Universe. In fact, these photons still carry the information about the temperature fluctuations of the Universe at the time of last scattering. Today, those temperature fluctuations are visible as temperature anisotropies in the CMB radiation.

From the map of CMB anisotropies it is possible to derive an angular power spectrum, see Figure 1.2: this spectrum has multiple peaks and features, which give us valuable constraints on the evolution and composition of the Universe. The power spectrum is remarkably well fitted using the parameters of the ΛCDM model, one of which is the density of cold dark matter. In other words, not only the power spectrum would not have the same shape without the presence of non-baryonic cold dark matter, but it also tells us with high precision the amount of cold dark matter present in the Universe. From the latest CMB data [35, 36] we can see that dark matter accounts for the 26.5% of the energy density of the Universe. From the same data, we also assume that 68.9% of the total energy density is made of dark energy, an unknown form of energy which permeates the Universe. The baryonic matter, instead, only accounts for 4.9% of the total energy density.

1.3.2 Baryon Acoustic Oscillations and Structure Formation

Baryon Acoustic Oscillations (BAO) are closely linked to the CMB. In fact, the same fluctuations responsible for the temperature anisotropies in the CMB can still be seen in the spatial distribution of matter in the Universe today.

In the Early Universe, before the hydrogen formation, baryons and electrons were bound together in a primordial plasma. This plasma was denser where dark matter was present and, as a result, there were overdense regions of matter. In this scenario, the overdense regions were attracting more and more matter due to their gravitational pull, but photons were also interacting stronger where matter was denser,

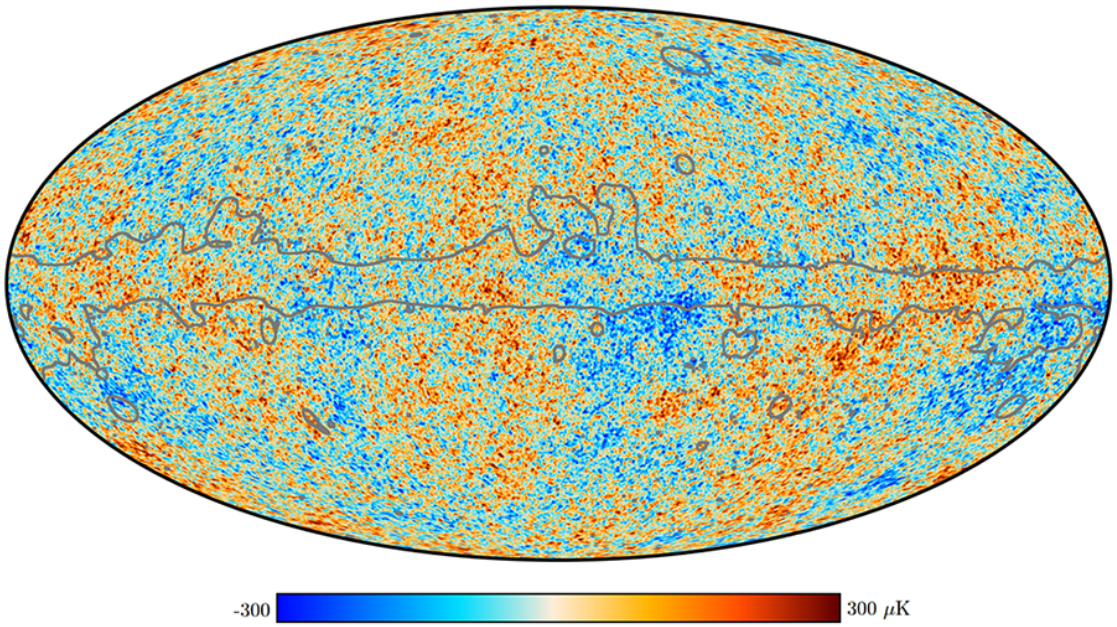

Figure 1.1: Fluctuations around the mean temperature T_0=2.7 K [47] in the CMB sky measured by PLANCK [48]. Blue (colder) spots indicate the presence of denser regions in the early Universe, red (hotter) spots the presence of regions with a lower density. Figure from [48].

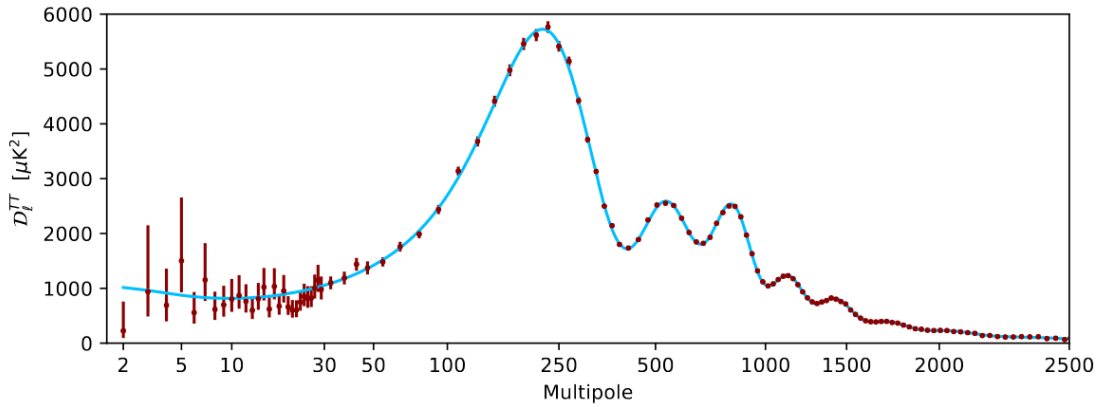

Figure 1.2: Angular power spectrum of CMB temperature fluctuations measured by PLANCK [48]. The spectrum is remarkably well fitted using the parameters of the ΛCDM model. Figure from [48].

causing an increase in heat and a resulting outward pressure. This means that, after the matter-radiation decoupling, the baryonic matter was organized in spherical shells centered around dark matter clumps. The radius of these shells is also referred as *sound horizon* and corresponds to the comoving distance that a sound wave can travel between the Big Bang and the time of the last scattering [49]. Both the dark matter clumps and the baryonic shells acted as seeds for the formation of large-scale structures like galaxies and galaxy clusters. As such, it is expected that galaxies are more likely to be observed at a certain distance from each other: this distance is equal to the sound horizon.
The SDSS Collaboration measured an excess of galaxies at a distance of $\sim$150 Mpc between each other [49], a clear signature in favor of the model of structure formation just described. Furthermore, this means that the sound horizon today is equal to $\sim$150 Mpc, providing a standard ruler with which it is possible to measure the Universe expansion. This observation is complementary to the CMB measurement and another strong evidence in favor of the ΛCDM model [50].

Another important piece of evidence for the existence of dark matter is the formation of large structures. Our understanding today is that each galaxy forms within a dark matter halo and its growth is linked to the halo itself [51]. Structure formation is an extremely complicated process and for this reason it is studied mostly by advanced cosmological simulations. As it is possible to see from Figure 1.3, modern galaxy formation simulations are able to correctly reproduce numerous observational results [52].
Furthermore, the time at which the galaxies started to form can be considered another proof in favor of dark matter. In fact, the presence of dark matter allows the formation of galaxies earlier than in an Universe constituted only by ordinary matter, consistently with the oldest galaxies observed [36].

1.3.3 Big Bang Nucleosynthesis

One of the earliest and most convincing evidence supporting the Big Bang theory is related to the abundance of light elements in the Universe [33, 36]. The formation of light elements such as ^{2}H (D), ^{3}He, ^{4}He, and ^{7}Li is commonly referred as Big Bang Nucleosynthesis and took place $\sim$3 minutes after the Big Bang [44]. The BBN mostly created ^{4}He, with a primordial mass fraction around 25%; D, ^{3}He, and ^{7}Li instead had abundances of respectively 10^{-5}, 10^{-5}, and 10^{-10} by number relative to H [36]. The abundances of light elements depend essentially on one parameter, the baryon-to-photon ratio η. This cosmological parameter can be derived using the CMB data [35] and then used to predict the light elements abundances. These predicted abundances are in remarkable agreement with the observations, with the notable exception of ^{7}Li [53].
However, η can also be independently constrained by the observation of the deuterium content in specific areas of the Universe. In fact, deuterium is formed only during BBN, which means that any observation provides a lower limit on its primordial abundance. By observing the hydrogen-to-deuterium ratio D/H in primordial-like systems, it is possible to constrain η, which provides a measure of the baryon density $\Omega_b h^2$. Finally, from the baryon density extrapolated with this method it is possible to infer that most matter in the Universe is dark and has a non-baryonic nature [36].

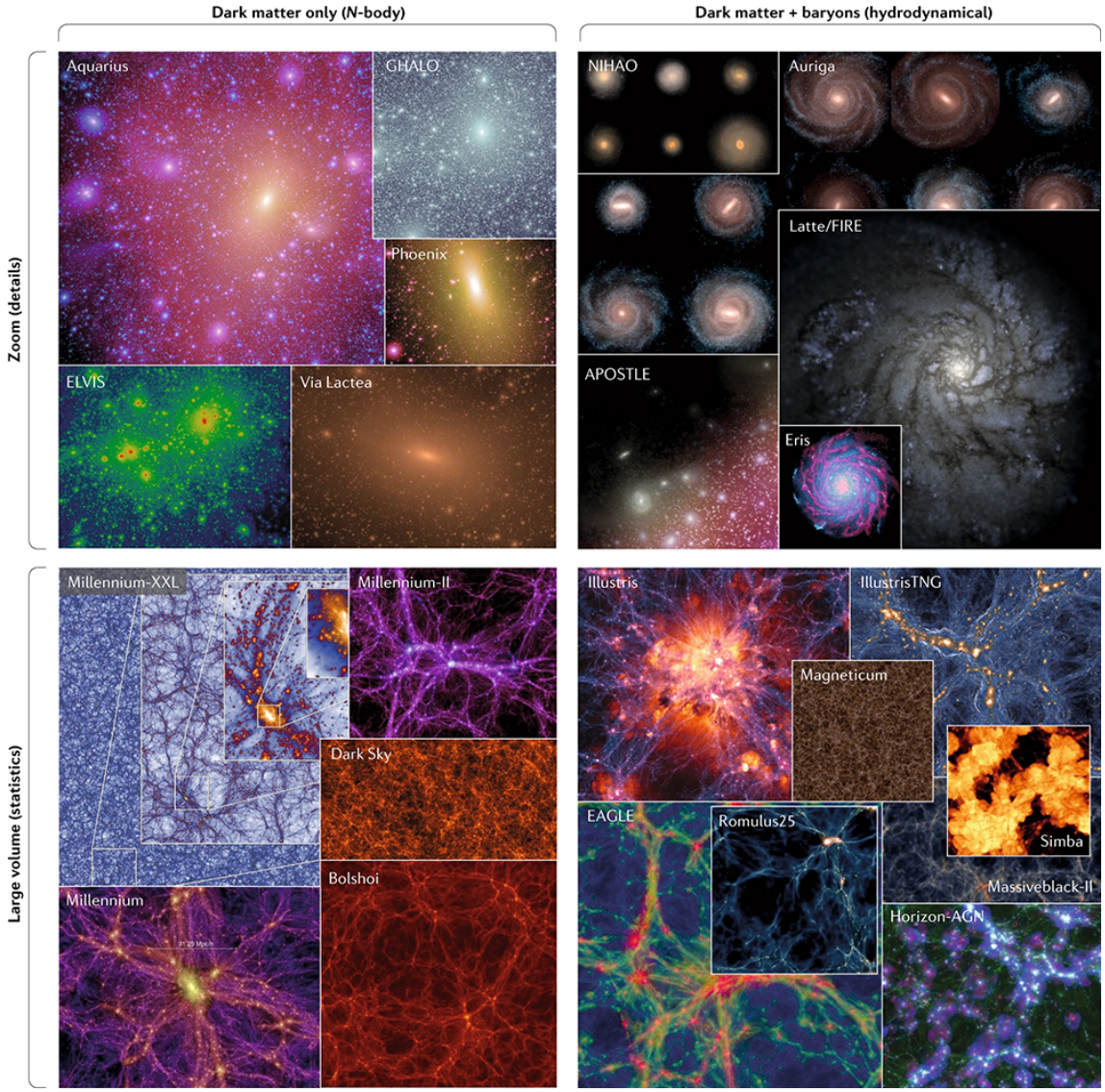

Figure 1.3: Graphic depictions of various galaxy formation simulations. On top there are small scale simulations and on the bottom large scale simulations. On the left simulations only accounting for the presence of dark matter are shown, while on the right they are also accounting the presence of baryonic matter. Figure from [52]

1.3.4 Velocity dispersion and rotation curves of galaxies

Two of the oldest pieces of evidence for the existence of dark matter, see Section 1.1, come from the observation of the velocity dispersion of galaxy inside the clusters and the rotation curves of spiral galaxies. Although these are two separate observations, they rely on the same basic discrepancy: the velocity of certain astronomical objects is exceeding the one expected when taking into account only the gravitational interactions induced by the surrounding luminous matter.

Modern data [54] confirm the first observations, pointing that the visible matter of a galaxy is embedded in a larger and more massive dark matter halo.

1.4 Dark matter interpretations

The amount of evidence pointing towards the existence of dark matter is remarkable, however there is no clear consensus among the scientific community on the nature of dark matter itself. In other words, dark matter is an accepted problem from an astronomical and cosmological point of view, but many different theories about its nature coexist. These theories offer a wide range of solutions to the dark matter problem, as depicted by Figure 1.4.
In general, we can distinguish theories which configure dark matter as a particle [55], as macroscopic objects [27, 28], or as an incomplete formulation of General Relativity [29]. This landscape is also complicated by the fact that most of these theories are broad and flexible enough to be re-tuned in light of new experimental data. For this reason, it is necessary to adopt an enormous experimental effort in all directions in order to solve the dark matter puzzle [56].

Since this thesis is centered around the direct detection of dark matter particles, it will focus solely on the particle dark matter case, but the reader should always keep in mind that there are alternatives to this scenario and the solution of the dark matter puzzle might even be a mixture of the different interpretations [36].

1.5 Dark matter candidates in the particle interpretation

Over the last decades a great deal of hypothetical particles never detected so far has been invoked to solve the dark matter mystery. This development is mostly due to the fact that none of the known elementary particles included in the Standard Model can well fit the cosmological observations consolidated in the ΛCDM model. It is beyond the scope of this thesis to discuss all the candidates invoked so far, thus only a selection of these candidates will be presented here, motivated by both historical relevance and current research interest: WIMPs, light dark matter, axions, and sterile neutrinos.

1.5.1 WIMPs

Weakly Interacting Massive Particles (WIMPs) are a broad class of hypothetical particles which can interact with ordinary matter through any interaction as weak

Figure 1.4: There are numerous valid ways to explain the dark matter nature and most, but not all of them, are consistent with the particle interpretation. Figure from [56].

or weaker than the weak interaction. This means that WIMPs interact gravitationally with matter, as expected for a dark matter candidate, and it is not excluded that they might be subject to a new interaction not yet discovered.
WIMPs are generally included in the 10 GeV–1 TeV mass range [55] and are historically the most studied dark matter candidate because of the so called *WIMP miracle*. The WIMP miracle is the surprising coincidence that a hypothetical particle coupling only through an interaction on the weak scale and with a mass close to the electroweak scale can broadly match the dark matter properties required by the ΛCDM model [57]. In fact, if one or more kinds of WIMPs exist, they would be created in the hot early Universe along with the other particles of the Standard Model and they would have roughly the same dark matter density inferred from cosmological observations.
There are numerous hypothetical particles falling inside the WIMP paradigm, but the most popular are related to supersymmetric extensions of the Standard Model or the presence of extra spatial dimensions [57]. Nowadays, a significant number of WIMP models is currently severely constrained or even ruled out in light of the experimental searches carried out over the last decade [58].

1.5.2 Light dark matter

In general, it is possible to have a dark matter candidate similar to WIMPs without requiring weak interactions or particles with masses close to the electroweak scale: these hypothetical particles could have masses in the 10 MeV–10 TeV range and even be subject to strong interactions [57]. This, of course, leaves room for an even more extensive experimental search and relaxes a bit the null results obtained so far.
The mass of WIMPs is constrained by the Lee-Weinberg bound [14], which imposes ≥ 2 GeV in order to fit the cosmological observations. However, nowadays there are multiple models that can predict a viable dark matter particle candidate while evading the Lee-Weinberg bound [59].
For example, gravitinos are one of the prime example of WIMPs predicted by supersymmetric models, but some subsets of supersymmetric theories, denominated gauge-mediated supersymmetry breaking (GMSB) models, predict the existence of light gravitinos in the eV–keV mass range [55]. These light gravitinos are a viable dark matter candidate and in one specific case, the one-component gravitino scenario (ΛWDM) with mass $\gtrsim$2 keV, this particle could be the main dark matter component [55].
Another path to obtain a viable light dark matter candidate, is the *SIMP miracle* [60]. In this case, the dark matter candidate is a Strongly Interacting Massive Particle (SIMP) which would also be a thermal relic. For this particular paradigm, the freeze-out process is a $3 \longrightarrow 2$ annihilation process in the dark sector, which is consistent with a dark matter particle with mass $\lesssim 1$ GeV and strong self interactions [60].
One last example of a viable light dark matter scenario, is asymmetric dark matter [61, 62, 63]. These are a set of models in which the relic density is strictly related to the baryon asymmetry present in our Universe nowadays. Currently, the dark matter density is about 5 times the one of visible matter. The visible matter

density we observe today, however, is highly dependent on a tiny excess of baryons over anti-baryons in the early Universe: in fact, the visible matter that we observe is what remains after all the anti-baryons annihilated with the corresponding number of baryons. Asymmetric dark matter models draw a comparison to the visible matter evolution, stating that the dark matter density observed today is similarly originated by a dark matter particle-antiparticle asymmetry in the early Universe. The mass scale of this candidate is $\sim$5 GeV, but if there are very different asymmetries in the visible and dark sectors, then the dark matter particles could also be much heavier or much lighter [62].

1.5.3 Axions

Following the introduction of the Peccei-Quinn mechanism to solve the strong CP problem [23, 24], Frank Wilczek and Steven Weinberg independently realized that one implication of this solution would be the existence of a very light and long-lived pseudoscalar boson [25, 26]. The new boson is the axion and it did not take long to realize that this particle could be an extremely valid dark matter candidate [64]. Similarly for the WIMPs, nowadays the term axion can be attributed to a broad class of scenarios introduced by a variety of theories, but in the most general sense it can be described as a light pseudoscalar field [65].
Since the Peccei-Quinn-Wilczek-Weinberg (PQWW) axion existence was quickly ruled out, the most popular axion models nowadays are the Kim-Shifman-Vainstein-Zakharov (KSVZ) and the Dine-Fischler-Srednicki-Zhitnitskii (DFSZ) [66]. One key observation to be made is that these axions might exist without being the main component of cold dark matter, *only* solving the strong CP problem [67]. Nevertheless, they currently constitute one of the most exciting domain of research for experimental particle physics.
A class of particles similar to the axions, generally labeled as Axion-Like Particles (ALPs), is also a realistic dark matter candidate, even though ALPs do not necessarily solve the strong CP problem [68, 69]. Axions or ALPs would not be thermally produced in the early Universe, a significant difference compared to most WIMPs scenarios [65, 69].

1.5.4 Sterile Neutrinos

The neutrino was the first particle to be scrutinized as a solution for the dark matter problem [8, 9]. Today, we know that the neutrinos included in the Standard Model can only make up a tiny fraction, between 0.5% and 1.6%, of the total dark matter of the Universe [70]. However, one of the simplest models which includes dark matter is the Standard Model with the addition of the right-handed neutrinos [21, 69], generally called *sterile neutrinos*. In fact, the SM contemplates only three left-handed neutrinos ν_e, ν_μ, and ν_τ, which are missing their right-handed counterparts. This is an odd circumstance, since all the other fermions included in the SM have both left and right-handed components [21].
Sterile neutrinos could exist with a vast range of masses, but in order to be a good dark matter candidate they should have a mass around the keV scale [69, 71]. Similarly to axions, sterile neutrinos are not thermally produced in the early Universe, but they can be produced with the right dark matter relic density via a

number of different mechanisms [71].

Chapter 2

Experimental techniques for dark matter detection

In this chapter a condensed overview on the possible types of experimental searches for dark matter is presented, with a special focus on the detection techniques for three main candidates: WIMPs, light dark matter, and axions. These detection techniques try to unveil interactions between dark matter and ordinary matter, besides gravitational interactions. It has to be noted that we could also live in a Universe in which dark matter particles interact only gravitationally with ordinary matter. In fact gravitational particle production in an expanding Universe can lead to the correct relic abundance for dark matter [72]. If this is the case, acquiring any information on the microphysics of dark matter would be extremely challenging [73], due to the extremely low energies involved in this kind of interactions.

2.1 Detection Principles

From a microphysics standpoint any detectable dark matter interaction with ordinary matter must take place with one or more particles included in the Standard Model. Furthermore, any detectable self-interaction between dark matter particles must produce one or more particles included in the Standard Model. Starting from these basic concepts, three main types of experimental approaches to the detection of dark matter can be distinguished: dark matter production, indirect detection, and direct detection (see Figure 2.1).

2.1.1 Dark matter production

This technique takes advantage of particle accelerators. The main idea of using particle accelerators to find dark matter is simple, but somewhat limited. In fact, by reproducing extreme energies and conditions there is the hope to finally find evidence of interactions beyond the ones included in the Standard Model.
The limitation which arises following this kind of approach is that it would be nearly impossible to prove that the novel particles are indeed the dark matter particles. In fact, in the case of production of new particles inside an accelerator, the only information would be that such particles were stable enough to exit the detector, but the requirement for a good dark matter candidate is much more stringent, since the particles must have a lifetime at least comparable to the one of the Universe [55].

However, an eventual discovery of physics beyond the Standard Model would provide an invaluable input on the mass scale to the other two experimental paths, the direct and indirect detection [74].

2.1.2 Indirect detection

Indirect detection is an approach aimed at detecting Standard Model particles emitted by dark matter self-annihilation or decay taking place in some specific areas of the Universe with a large dark matter density, such as galactic centers or stellar cores [75]. The annihilation products typically under investigation are gamma-rays, neutrinos, positrons, and antiprotons [75, 76]. Each of these products need dedicated experiments and are subject to different challenges.
Gamma-rays produced in a dark matter self-annihilation are unlikely to be observed directly from Earth, since photons in the GeV–TeV range would be stopped inside the planet's atmosphere [75]. For this reason, there are dedicated space-based experiments currently investigating the gamma flux coming from specific areas of the Universe. A prime example of this approach is the observation of Milky Way's dwarf galaxies [77] performed by the Fermi satellite [78]. However, there are also ground-based telescopes focused on indirectly detecting the incoming flux of highly energetic photons, such as H.E.S.S. [79], VERITAS [80], and MAGIC [81]. Space-based experiments and ground-based telescopes provide strong bounds over a wide range of energies for a variety of annihilation channels [82].
Positrons and anti-protons can also be used to detect dark matter annihilation, but they offer a clear disadvantage compared to gamma-rays and neutrinos. In fact, as charged particles, they are diffused by galactic magnetic fields. This means that in case of a distinctive signature in the flux of positrons or anti-protons, it would not be possible to pinpoint the source of these events [75]. The most stringent limits on these annihilation channels are provided by the AMS-02 experiment [83] installed on the International Space Station.
Indirect searches based on neutrinos offer the clear advantage that these particles hardly interact before reaching our planet, even offering the possibility to observe them in low-background experiments situated underground. This, however, is also a clear disadvantage, since large size experimental volumes are required in order to detect a satisfying number of events. Indirect searches for neutrinos are based on the idea that dark matter particles could accumulate inside cosmological bodies. There, the dark matter particles can annihilate and all the products are immediately absorbed, with the exception of neutrinos which can escape freely [55]. Examples of this kind of searches are the one performed by IceCube [84] and Super-Kamiokande [85]. It has to be noted that these observations, under certain assumptions, can directly compete with direct detection experiments [55].
Overall, the biggest drawback for indirect detection is the presence of large astrophysical backgrounds, which could mimick a dark matter signal [37]. Furthermore, indirect detection might not be suited to probe effectively all the particle dark matter candidates. One example of this is asymmetric dark matter: the self-annihilation of dark matter particles would be irrelevant, giving the small amount of dark matter antiparticles currently present in the Universe, which would result in an absence of a detectable signal for indirect detection experiments [63].

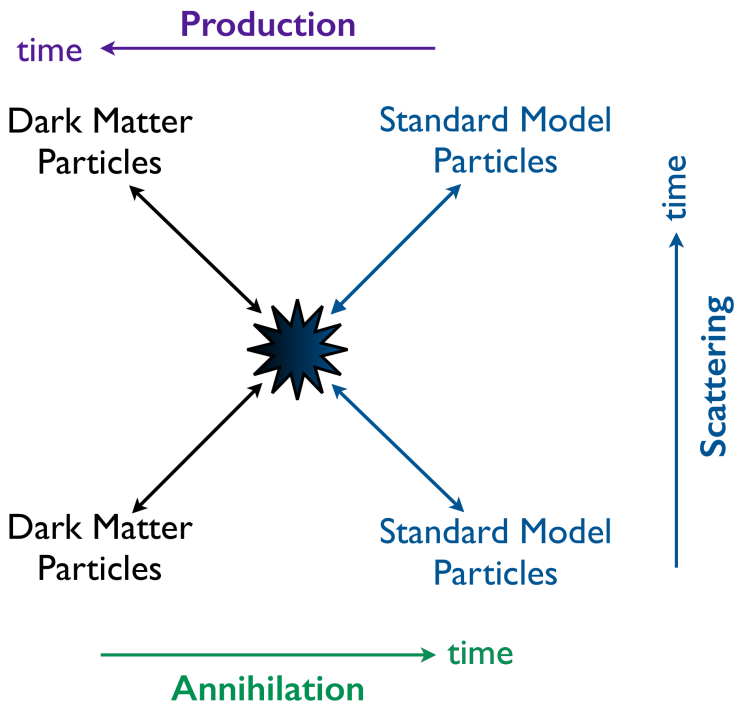

Figure 2.1: A schematic visualization of the three experimental approaches to dark matter search. Dark matter production exploits the collisions of Standard Model particles to create dark matter particles. Indirect detection studies the flux of Standard Model particles to acquire information about the dark matter self-annihilation. Direct detection focuses on the scattering between dark matter and Standard Model particles. Figure from [88]

2.1.3 Direct detection

Today, the most popular approach to dark matter search is arguably the direct detection. This type of approach focuses on the detection of a scattering between a dark matter particle and a certain target material located on Earth.
The first proposal of direct dark matter detection was laid out for WIMPs by Mark Goodman and Edward Witten [86], following the work on neutral-current neutrino detectors proposed by Andrzej Drukier and Leo Stodolsky [87]. Currently, the core principle is still very similar: a dark matter particle traveling inside our galaxy might elastically scatter against a nucleus of a given experimental target, transfering a detectable amount of energy. This amount of energy, however, should be quite small, in the 1–100 keV range for a dark matter particle with a mass close to the weak scale. Furthermore, similarly to neutrinos, the neutral dark matter particles should rarely undergo any scattering with ordinary matter. To tackle these two main challenges, most direct search experiments employ extremely sensitive detectors with large experimental volumes located in underground laboratories, see Section 2.2.
Nowadays, direct dark matter search is not only limited to the study of interactions between dark matter particles and nuclei, nor only focused on WIMPs, but instead involves a variety of experimental efforts tailored around numerous dark matter candidates.

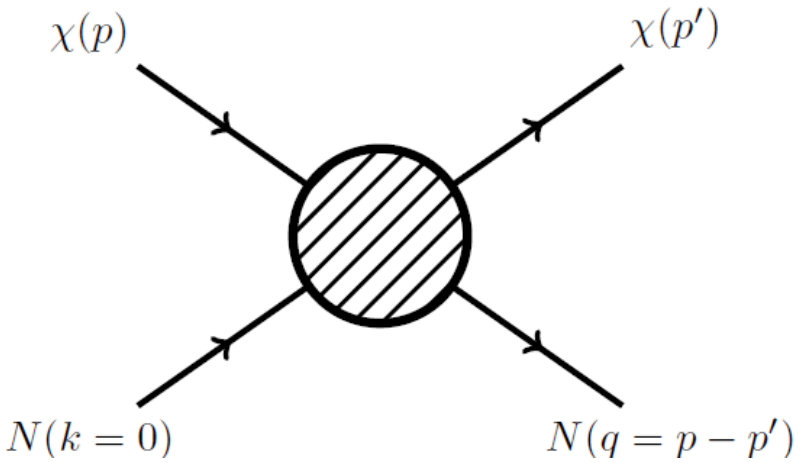

Figure 2.2: Schematic representation of the scattering kinematics between a dark matter particle χ and a nucleus N. The nucleus is assumed at rest initially and carries a momentum q after the scattering, while the dark matter particle has a momentum p before the interaction and scatters off with a momentum p'. Figure from [37].

2.1.4 Interactions with nuclei

A key aspect of dark matter scattering with nuclei is the kinematics involved in the process. We can schematize this type of interactions by assuming that the nucleus N of the experimental target is at rest, initially, while the dark matter particle χ has a certain momentum $p{=}m_\chi v$, see Figure 2.2. After the interaction, the nucleus will have a certain momentum q, given by the difference between the momentum of the incoming dark matter particle p and the momentum of the same dark matter particle after the scattering p'. We can then write:

$$E_i = E_\chi = \frac{\mathbf{p}^2}{2m_\chi} = \frac{\mathbf{p'}^2}{2m_\chi} + \frac{\mathbf{q}^2}{2m_N} = E'_\chi + E_N = E_f \tag{2.1}$$

where E_i is the total energy before the scattering and E_f is the total energy after the scattering. It is now useful to define the reduced mass of the χ-N system:

$$\mu_N = \frac{m_\chi m_N}{m_\chi + m_N} \tag{2.2}$$

The energy detectable by an experiment is the one carried by the nucleus after the scattering E_N. The maximum energy acquired by the nucleus after the scattering can be expressed, see [37], as:

$$E_N^{max} = \frac{2\mu_N^2 v_{max}^2}{m_N} \tag{2.3}$$

Nuclei have a ∼1–200 GeV mass range, while the mass of the incoming dark matter particle is unknown. The maximum velocity is equal to the escape velocity in the Milky Way which is estimated to be $v_{max}{=}v_{esc}{=}544$ km/s [89]. If we now consider the typical mass range for WIMPs, 10–1000 GeV, we can see that the maximum recoil energy is ∼5–7 keV for the lightest nucleus and ∼3–910 keV for the heaviest. However, if considering WIMP-like particles with lighter masses, in the 0.1-1 GeV

range, the maximum recoil energy dramatically reduces for the heaviest nucleus down to $3{\cdot}10^{-4}$–$3{\cdot}10^{-2}$ keV, while it only decreases to $5{\cdot}10^{-2}$–1.6 keV for the lightest nucleus. In short, this tells us that:

- a successful dark matter experiment must be sensitive to $\mathcal{O}(keV)$ recoils.
- different nuclei, hence different targets, are best suited for probing different dark matter masses.
- heavy nuclei have larger interaction rates with dark matter particles, if the kinematics of the scattering is not taking into account.
- all direct dark matter search experiments based on the detection of scatterings off nuclei eventually become blind at low dark matter masses, when E_N^{max} becomes lower than the energy threshold of the experiment E_{Th}, due to kinematics. This is more relevant the heavier the nucleus.

Another interesting observation can be made calculating $q_{max} = 2\mu_N v_{max}$, which equals to ∼30–600 MeV/c for a heavy nucleus undergoing a scattering with a typical WIMP. This can be translated into a De Broglie length of $1/\mathrm{q}_{max}$ ∼2–40 fm, comparable to the size of a typical atom which lies in the ∼2–12 fm range. The fact that these two lengths are comparable, means that there is the need to introduce a form factor which takes into consideration the shape of the nucleus. However, for light nuclei q_{max} lowers to ∼3 MeV/c and the De Broglie length increases to ∼400 fm, meaning that in this case the dark matter particle interacts coherently with the whole nucleus [37]. A similar effect can be observed for the scattering of dark matter particles with masses of $\mathcal{O}(GeV)$, regardless of the nucleus involved in the interaction, since the De Broglie length is $\gtrsim$400 fm.

All the key elements to design a dark matter experiment come from the scattering rate. In general, the differential scattering rate of dark matter particles off nuclei is given by [90]:

$$\frac{dR}{dE_N} = \frac{\rho_0 M}{m_N m_\chi} \int_{v_{min}}^{v_{esc}} v f(v) \frac{d\sigma}{dE_N} dv \tag{2.4}$$

Some of the quantities appearing in this equation are related to astrophysics and cannot be changed, such as the dark matter density in the Milky Way ρ_0=0.3 GeV/c^2/cm^3 [91], the escape velocity v_{esc}, or the velocity distribution of dark matter particles in the laboratory frame *f(v)*. It has also to be noted that these quantities are subject to uncertainties and are only valid in the context of the Standard Halo Model (SHM) [92]. Other quantities, like the detector mass M, the mass of the nucleus m_N, and the minimum velocity v_{min} depend strictly on the target employed by the experiment. The minimum velocity is particularly important and defined as:

$$v_{min} = \sqrt{\frac{m_N E_N}{2\mu_N}} \tag{2.5}$$

The physical meaning of this quantity is that this velocity is the minimum needed to cause a nucleus recoil with energy E_N, but it can easily be interpreted as the minimum velocity for a dark matter particle with mass m_χ to cause a detectable nucleus recoil in a specific detector. In fact, since all the events with $E_N < E_{Th}$ cannot

be detected, they will not contribute to the measured rate. So, for any given dark matter mass, an experiment can only detect scatterings of dark matter particles with $v \geq v_{min}$.

The differential cross section $d\sigma/dE_N$ appearing in Equation 2.4 is also extremely relevant. Different cross sections are related to different types of interactions between dark matter particles and nuclei, with the main distinction usually being made between spin-independent and spin-dependent interactions. Before introducing these interactions, it is important to specify that spin-independent and spin-dependent interactions are included in a more general set of theories describing the possible 4-point-interactions in a dark matter-nucleon interaction [90]. These theories fall under the name of Effective Field Theory (EFT) and provide 18 operators $\hat{\mathcal{O}}_i$ which can describe the dark matter-nucleon interaction [93]. Of these operators, $\hat{\mathcal{O}}_1$ and $\hat{\mathcal{O}}_4$ correspond respectively to the standard spin-independent and spin-dependent interactions.

Spin-independent interactions

In general, the differential cross section for interactions not depending on the nuclear spin can be written as [94]:

$$\frac{d\sigma}{dE_N} = \frac{2m_N}{\pi v^2}[Zf_p + (A-Z)f_n]^2 F^2(q) \tag{2.6}$$

where f_p and f_n are respectively the dark matter coupling to protons and neutrons, Z is the atomic number of a given nucleus, A is its mass number, and $F^2(q)$ is the nuclear form factor.
Spin-independent interactions between dark matter particles and nuclei have been the most studied at the experimental level in the past decades. One of the main reason for this is that this particular type of interaction takes advantage of the coherence of the scattering. In fact, if $f_p = f_n$ [94], Equation 2.6 becomes:

$$\frac{d\sigma}{dE_N} = \frac{2m_N}{\pi v^2}A^2 F^2(q) \tag{2.7}$$

In this case, the dark matter-nucleon interaction is constructive over the whole nucleus, meaning that the expected rate for an experiment is proportional to A^2. However, depending on the value of q, the coherence of the interaction is in part suppressed by the nuclear form factor [37], see Figure 2.3.

For an experiment it is particularly advantageous to probe spin-independent interactions because this type of interactions is usually the one providing the highest expected rate. Furthermore, since these interactions do not depend on the nuclear spin, there is no constraints in the target selection.

Spin-dependent interactions

The typical differential cross section for spin-dependent interactions is [94]:

$$\frac{d\sigma}{dE_N} = \frac{16m_N}{\pi v^2}G_F^2 \frac{J}{(J+1)}[a_p\langle S_p\rangle + a_n\langle S_n\rangle]^2 F_{SD}^2(q) \tag{2.8}$$

where G_F is the Fermi coupling constant, J is the nuclear spin, a_p and a_n are respectively the effective coupling of dark matter to protons and neutrons, $\langle S_p\rangle$ and

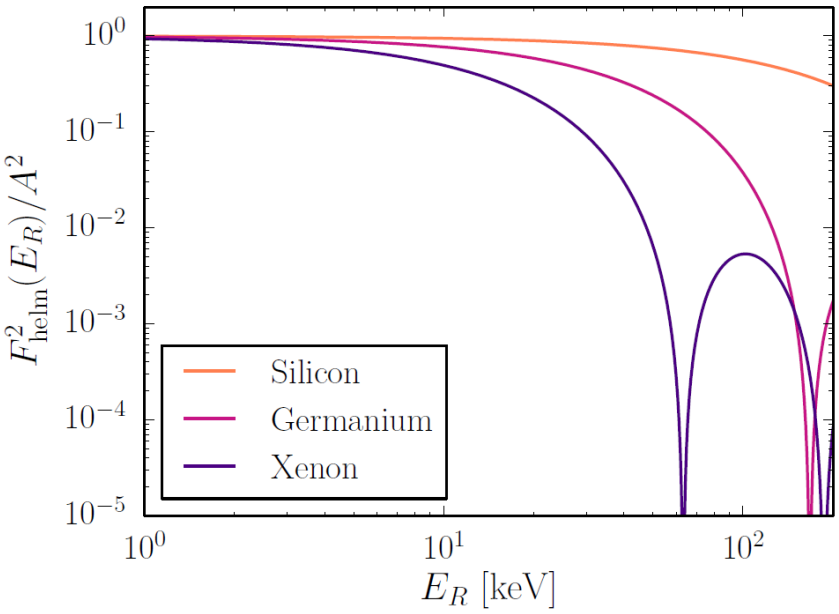

Figure 2.3: Helm form factor calculated for Silicon (A=23), Germanium (A=73), and Xenon (A=131). It is possible to see that for low recoil energies (< 10 keV) the coherence suppression is low for all nuclei. At higher recoil energies, instead, the suppression is more relevant the higher the mass of the nucleus. Figure from [37].

$\langle S_n \rangle$ are the average spin contribution of protons and neutrons, and $F^2_{SD}(q)$ is the nuclear form factor for spin-dependent interactions.
This cross section, in principle, requires detailed nuclear calculations in order to achieve the most accurate description of the interaction, see [95, 96]. However, for most nuclei they are not needed [97], since reasonably accurate estimates can be made using the *Odd-Group Model* [98]. This model assumes that all the nuclear spin of isotopes with odd A is carried by the unpaired type of nucleons: if the number of neutrons is odd, then it is the neutrons that carry the nuclear spin (a_p=0, a_n=1), and vice versa if the protons are in odd number (a_p=1, a_n=0). Basically, all the contributions to the interaction arising from the nucleons are discounted with the exception of one unpaired proton, if Z is odd, or neutron, if Z is even. In the first case these interactions are commonly referred as *proton-only* and in the latter as *neutron-only* interactions.
From Equation 2.8 it can be noticed immediately the lack of A^2, compared to the spin-independent cross section. This means that, while the recoil for a dark matter particle is still elastic and with the whole nucleus, the expected rate does not increase if the nucleus size increases. This is very intuitive since, as stated before, the interaction is essentially carried by a single nucleon. Furthermore, Equation 2.8 tells us that any target with a nuclear spin J=0 is insensitive to spin-dependent interactions. The last thing to point out is that $\langle S_p \rangle$ and $\langle S_n \rangle$ cannot exceed 1/2, since they are the spin contributions of a single proton or neutron.
Clearly, probing spin-dependent interactions poses more challenges than doing so for spin-independent interactions. First, the lack of the coherence term in the cross section means that for a target nucleus in the 10–100 GeV mass range the expected rate is suppressed by 3–5 orders of magnitude if compared to the one expected for

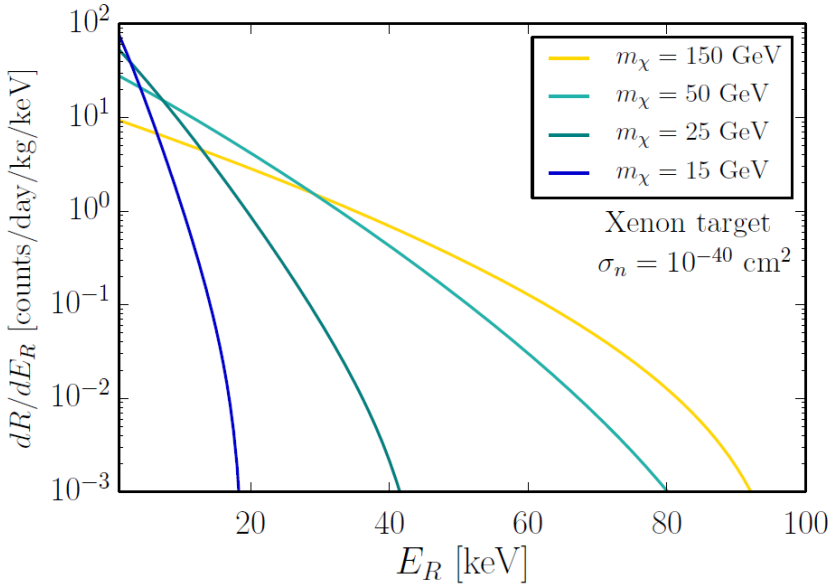

Figure 2.4: Expected recoil spectrum calculated for a Xenon target in case of spin-independent interactions induced by dark matter particles with different masses. Figure from [37].

spin-independent interactions. The second limitation is given by the restriction of the suitable targets for an experiment, since a large fraction of isotopes have J=0. A comprehensive list of suitable target isotopes to probe spin-dependent interactions can be found in [99], but the ones mostly employed by direct search experiments so far are ^{19}F, ^{73}Ge, ^{129}Xe, and ^{131}Xe.
In light of these challenges, it is quite obvious that in the past decades experiments have focused in large part on probing spin-independent interactions. This is even more clear when considering the fact that in some theoretical models spin-independent and spin-dependent interactions are correlated [100], which means that experimental efforts are more fruitful if concentrated on the easiest interactions to probe. However, once some of the theoretical requirements are relaxed, such as the dark matter particle holding electroweak charges, models where the spin-dependent interactions are the only viable interactions do exist [101].

2.1.5 Annual modulation

The expected spectrum in case of dark matter interactions with a detector is a generic quasi-exponential rise towards the low energy with a slope that depends on the dark matter particle mass, see Figure 2.4. Unfortunately, this type of signature is quite bland.
In case a potential signal is experimentally detected, a significant help might come from the study of the annual modulation of this signal. In fact, in the laboratory frame the dark matter velocities are oriented opposite with respect to the Sun's motion [94]. This results in a *wind* of dark matter particles, such that the Earth moves towards this wind during summer and moves away from it during the winter, see Figure 2.5. This can be seen when converting the Galactic-frame velocity distribution *f(v)* of Equation 2.4 in the lab-frame velocity distribution $\widetilde{f}(v,t)$, where

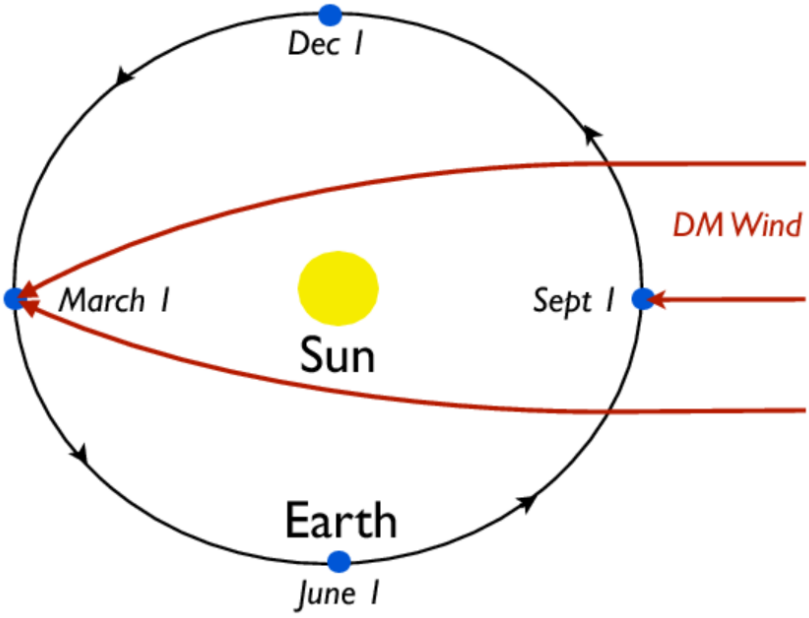

Figure 2.5: Schematic representation depicting the direction of the dark matter *wind* to the respect of the annual motion of the Earth around the Sun and the gravitational focusing of dark matter particles induced by the presence of the Sun. Figure from [102].

the time dependence is due to the variation of the velocity of the Earth around the Sun [94]. In short, during summer we expect to see more high-velocity dark matter particles than in winter, which means we can expect a higher number of detected events above threshold in June compared to December. However, there is also a competing effect caused by the gravitational focusing due to the presence of the Sun (see Figure 2.5), which is stronger for slower dark matter particles and could shift the maximum number of detected events towards March, while shifting the minimum towards September [102].
The most controversial result in direct dark matter search is the annual modulation of events detected by the DAMA experiment with a confidence level of 12.9 σ [103]. While this signal could be in principle compatible with the annual modulation of a dark matter signal, it is incompatible with numerous other experimental observations [90] without invoking highly fine-tuned theoretical models [104].
Overall, the DAMA case is an excellent example that dark matter search is extremely challenging and not even the presence of an annually modulated signal is enough to claim a definitive dark matter detection. For this reason, direct dark matter detection can be realized only when a collective experimental effort produces a consistent result.

2.2 Direct search experiments

This section is dedicated to the experiments currently searching for interactions between dark matter particles and an experimental target. Originally, these experiments were designed to detect WIMPs, but their physics reach can easily be extended to light dark matter and other dark matter candidates.

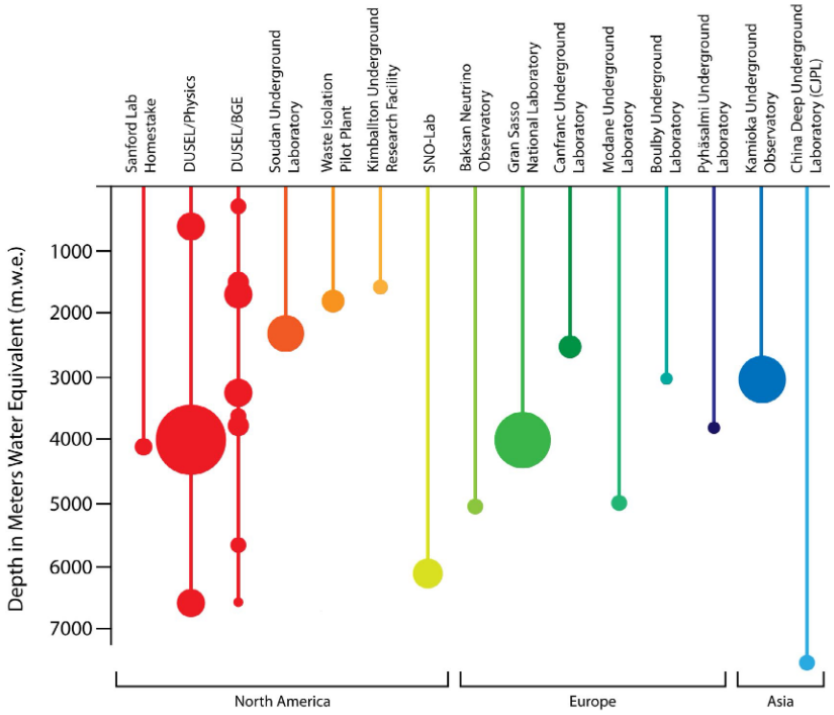

Figure 2.6: A list of existing and proposed underground laboratories divided by geographic areas with the relative size (circles) and depth in meters water equivalent [105]. Currently, the deepest operational laboratory is CJPL located in China, while the largest is LNGS located in Italy. Figure from [105].

The shared feature of these experiments is that they are located in deep-underground laboratories, in order to suppress the background induced by cosmic rays, see Figure 2.6. Otherwise, a wide variety of experimental techniques is employed in the field of direct detection, so it is useful to divide them in some categories: noble liquid detectors, bubble chambers, proportional counters, and cryogenic detectors.

2.2.1 Noble liquid detectors

Experiments using liquefied noble gases have been arguably the most successful in the direct dark matter search for WIMPs so far. These experiments employ either argon ($A \simeq 40$) or xenon ($A \simeq 131$) which are both excellent scintillators, but other noble gases could also be suitable targets [106]. In standard conditions, these elements assume a gaseous state which would prevent the design of a large-exposure experiment, but they can be conveniently liquefied to very dense targets. Argon becomes liquid at 87.2 K and xenon at 162.5 K [90], so both can be easily liquefied only using liquid nitrogen.
A particle interacting with a noble liquid produces heat, scintillation, and ionization. Current experiments are not able to measure heat, but focus instead on detecting scintillation and ionization signals. Liquid noble gases experiments can be divided in two main categories based on which detector they use to measure these signals: single phase detectors or dual-phase Time Projection Chambers (TPCs), see Figure 2.7.
Single phase detectors only measure the primary scintillation (S_1) caused by the

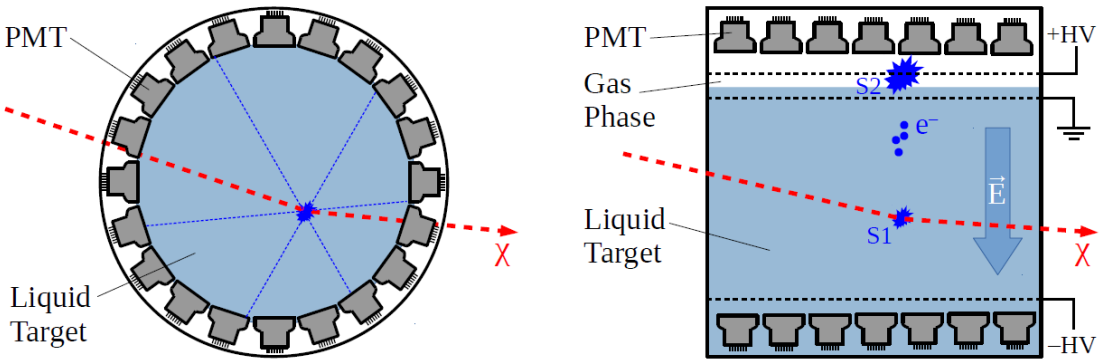

Figure 2.7: Left: sketch of an interaction between a dark matter particle and a liquid noble gas inside a single-phase detector. This detector measures the primary scintillation induced by the interaction via an array of photosensors surrounding the experimental volume. Right: sketch of an interaction between a dark matter particle and a liquid noble gas inside a double-phase TPC. In this case, apart from measuring the primary scintillation with the photosensors, the electrons produced in the ionization of the medium are drifted via a strong electric field towards a volume filled with gas. There, the electrons can cause a secondary scintillation signal that is measured by the surrounding photosensors. Figure from [90].

scattering of a particle inside the experimental medium, while experiments employing dual-phase TPCs can also measure the ionization signal (S_2) by extracting the electrons produced in the interaction via a strong electric field. Both the primary scintillation and ionization signals are generally measured with photomultiplier tubes (PMTs), but some experiments are planning to shift in the future to silicon photomultipliers (SIPMs) [107, 108].
Example of experiments using single-phase detectors are XMASS [109] for xenon and DEAP-3600 [110] for argon. Experiments employing dual-phase TPCs with a xenon target are PANDAX [111], XENON1T [112], and LUX/LZ [113], while DarkSide [114] is based on argon.

2.2.2 Bubble chambers

Bubble chambers for dark matter search employ superheated fluids kept above the boiling point in a metastable state. Examples of suitable targets are CF_3I, C_3F_8, C_4F_{10}, C_2ClF_5, and C_3ClF_8 [90]. When a particle interacts with the fluid, it can deposit enough energy to cause a local phase transition which will result in the formation of a bubble, see Figure 2.8. This method of detection is extremely convenient, since the bubble formation can be tuned to take place only in the presence of a nuclear recoil induced by α particles, neutrons, or dark matter particles. The bubbles are detected through cameras and the images can be used to determine the spatial coordinates of the events. Acoustic sensors can also be employed to record sound emissions caused by bubble nucleation: this technique is very effective in suppressing background events, since nuclear recoils induced by α particles have a very distinctive signature [115].
The drawback of this kind of detectors is the inability of detecting the recoil energy, which means that they can only be used as counters of events above a certain

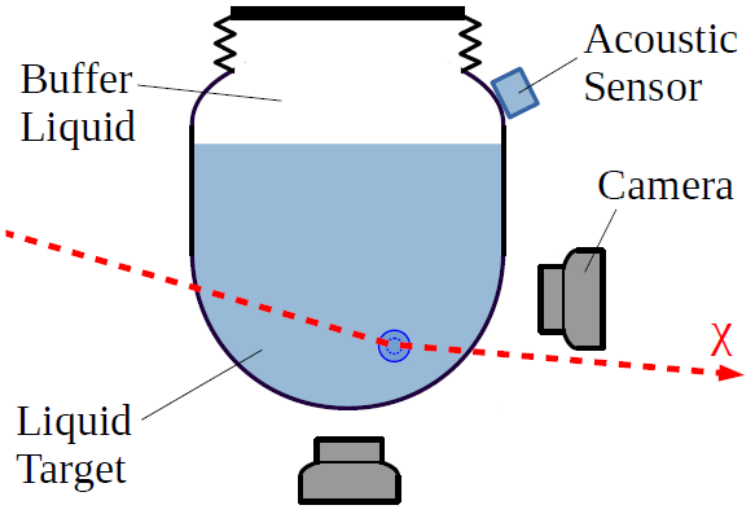

Figure 2.8: Sketch of a dark matter interaction taking place with a superheated fluid inside a bubble chamber. The nuclear recoil induced by a dark matter particles causes the formation of a bubble if the recoil energy is above a certain energy threshold. Bubbles are detected using cameras, while acoustic sensors are used to suppress the background induced by α particles. Figure from [90].

energy threshold. Furthermore, after each event the bubble chamber has to be compressed and subsequently decompressed, causing a substantial dead time. Despite these challenges, the PICO-60 experiment has achieved a world-leading sensitivity for dark matter-proton spin-dependent interactions with ^{19}F [116].

2.2.3 Spherical Proportional Counters

Spherical Proportional Counters (SPCs) are constituted by a spherical vessel filled with pressurized gas. The vessel is grounded and constitutes the cathode, while at the centre of the sphere there is a small resistive body acting as anode. The anode is supported by a metallic rod through which a high voltage is injected [117]: in this way the electric field inside the detector varies as $1/r^2$, where r is the distance from the center. This sharp change in the electric field divides the detector volumes into two regions: the amplification region and the drift region.
When a particle interacts inside the volume, it causes the ionization of the gas followed by the emission of primary electrons. These electrons drift towards the amplification region where they acquire enough energy to produce a ions-electrons avalanche. The ions resulting from the avalanche drift towards the cathode and induce the signal, which is read via the high voltage wire, see Figure 2.9. Any particle interaction detected in a SPC has two distinctive observables: the amplitude of the signal, correlated to the energy deposition, and its rise time, correlated to the position of the interaction [117].
Advantages of this kind of detectors are the high radiopurity of the materials employed for its construction, the flexibility in the choice of the target gas (Ne, He, H, CH_4), and the possibility to achieve energy thresholds for nuclear recoils $<$1 keV.
While these detectors can be used for a variety of applications, the main experiment

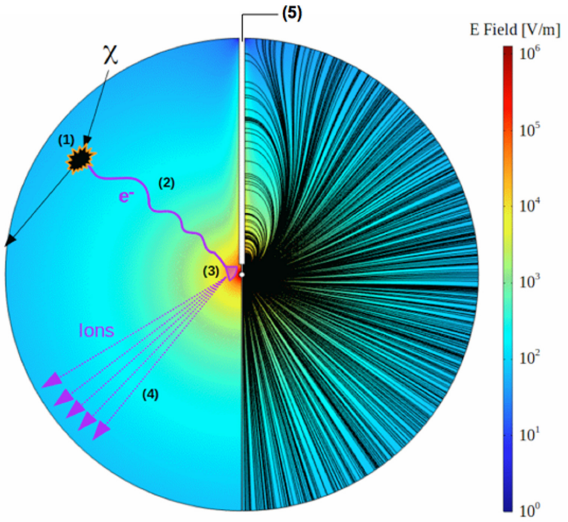

Figure 2.9: Sketch of an interaction between a dark matter particle and the gas inside a Spherical Proportional Counter. After the scattering there is the production of a primary electron (1), which drifts towards the center (2). When the electron reaches the amplification region it produces a ion-electron avalanche (3). The positive ions drift then towards the outer vessel (4) inducing the signal read through the high voltage wire (5). Figure from [119].

of this kind involved in direct dark matter search is NEWS-G [118].

2.2.4 Cryogenic detectors

Cryogenic detectors have been among the first detectors to be employed in direct dark matter search. These detectors are based on crystalline targets cooled down to temperatures below 50 mK and coupled with mainly two different kind of sensors: Transition Edge Sensors (TES) and Neutron Transmutation Doped (NTD) germanium thermistors [90]. These sensors detect the heat signal induced by particle interactions inside the crystals, see Figure 2.10, and are able to detect tiny energy depositions with high energy resolutions. To ensure an effective background rejection, experiments of this kind also detect a second signal coming from particle interactions inside the target. Depending on the experiment, in fact, the ionization or the scintillation produced by particle interactions within the crystals are measured in coincidence with the heat signal: from the ratio of these signals it is possible, in most cases, to distinguish electronic recoils events from nuclear recoil events which are generally associated with dark matter interactions in the target.
The most prominent experiments of this kind are currently SuperCDMS [120], EDELWEISS-II [121], and CRESST-III [122].
Since this thesis focuses on novel physics results obtained with cryogenic detectors, the underlying physical aspects of this particular class of detectors will be explained in more detail in Chapter 3.

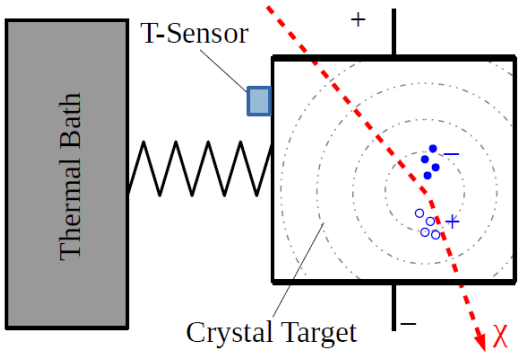

Figure 2.10: Sketch of a particle interaction taking place inside a crystal thermally coupled to a thermal bath in the ∼10 mK range. The particle interaction produces a heat increase which is measured by a sensor placed on the crystal's surface. The particle interaction can also cause ionization or scintillation that can be used for particle discrimination and background rejection. Figure from [90].

2.3 Experimental searches for Axions and ALPs

If axions exist, they introduce a modification to Quantum Electrodynamics (QED) allowing the interaction with photons inside an external magnetic field. Thus, a photon traveling through a transverse magnetic field can oscillate in a real or virtual axion and vice versa [123].
This means that valid strategies for axion discovery can revolve around purely laboratory-based experiments, see Section 2.3.1. However, this is not the only viable path to axion discovery. In fact, stars could be intense sources of axions, which could be then converted to photons in the presence of a magnetic field, see Section 2.3.3. Furthermore, if dark matter is constituted by axions, there would be the presence of a large number of cosmological axions which could be detected through various experimental techniques, see Section 2.3.2.
A summary of the limits set by various experiments can be seen in Figure 2.13.

2.3.1 Purely laboratory-based experiments

Purely laboratory based experiments do not try to detect axions from cosmological or astrophysical sources, but instead try to study the axion-photon interactions in a laboratory.
One striking implication of the axion-photon oscillation is the possibility to perform *light shining through a wall* (LSW) experiments [68, 123]. The idea is to point a light source towards an opaque wall and try to convert the photons into axions or ALPs. At this point, the axions or ALPs can pass through the wall with minimal interactions and be reconverted back to photons which can be detected, see Figure 2.11. These experiments usually employ lasers emitting visible light, which means that they are sensitive to particles with meV masses [68]. Examples of this experimental approach are the ALPS [124] and GammeV [125] experiments.
Alternatively to reconverting the axions into photons, a viable detection method is to study the polarization of the light beam through the transverse magnetic field [36]. In fact, in the case of photon-axion conversion, there should be an anomalous im-

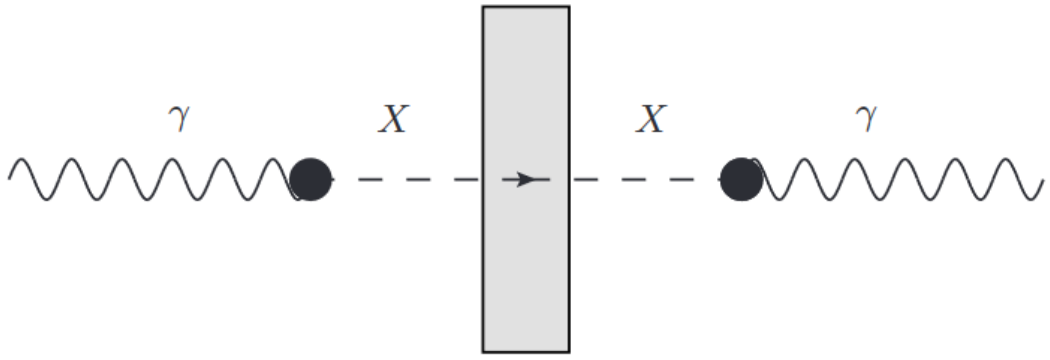

Figure 2.11: Sketch of a *light shining through a wall* experiment. A photon γ is converted into an axion or ALP X. The particle X is then reconverted back to a photon, which can be finally detected.Figure from [68].

pact on the dichroism and birefringence of the polarized light. An example of this approach is the PVLAS experiment [126].

2.3.2 Solar axions search

There are several mechanisms that could contribute to the axion production inside stars. In case of hadronic axion models, such as the KSVZ axion, the main production process is the Primakoff conversion of plasma photons into axions [127]. In case of axion models predicting an axion-electron coupling at the tree level, there are a number of processes, called ABC reactions, of comparable importance to the Primakoff conversion, see Figure 2.12 [128]. The last production process is related to specific isotopes which can be found inside the Sun, In fact, monoenergetic axions can be produced by nuclear M1 transitions of ^{7}Li (478 keV), ^{23}Na (440 keV), ^{55}Mn (126 keV), ^{57}Fe (14.4 keV), and ^{83}Kr (9.4 keV) [129, 130, 131]. If these reactions are taking place inside the Sun, there should be a significant flux of axions with energies in the 1–15 keV range investing our planet [127].
Currently, the most effective way to detect these solar axions is trough helioscopes, which rely on the production of these particles inside the Sun [68]. These experiments are based on Earth and employ detectors pointed at the Sun, which acts as a powerful axion source. To obtain a detectable signal, intense magnetic fields are employed in the experimental setup to convert solar axions into photons. The main example of this approach is the CAST experiment at CERN [132].
Other techniques which can be used to study solar axions involve the detection of an axion interaction with an experimental target. This kind of experiments share a lot of similarities with direct search experiments for dark matter particles and can search for a number of different interactions. One strategy is to look for characteristic Bragg patterns in a crystalline target [133, 134, 135, 136], a second strategy is to look for the axio-electric effect in the target [137, 138, 139], and another one for the re-conversion of monocromatic axions into photons employing targets containing ^{7}Li [130, 140], ^{57}Fe [141], or ^{83}Kr [131]. The last strategy is to take advantage of the resonant absorption of axions by isotopes with low energetic excited nuclear

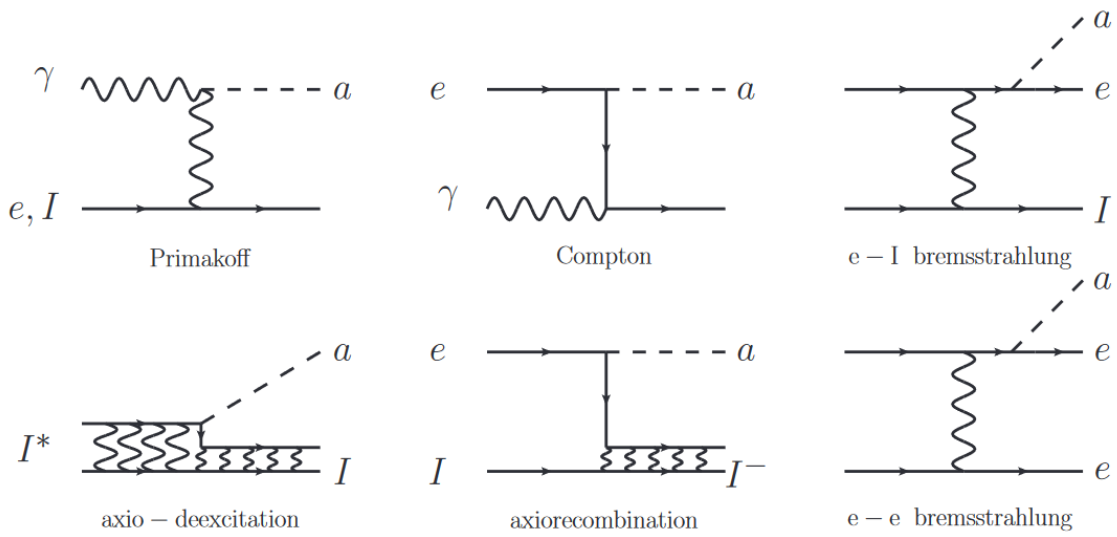

Figure 2.12: Feynman diagrams of reactions producing solar axions in non-hadronic axion models. From top left: Primakoff conversion, Compton scattering, axio-Bremsstrahlung in an electron-ion collision, atomic axio-deexcitation, atomic axio-recombination, and axio-Bremsstrahlung in an electron-electron collision. In hadronic axion models the only relevant process is the Primakoff conversion. Figure from [128].

states (<15 keV), such as ^{57}Fe [142], ^{83}Kr [143], or ^{169}Tm [144]. However, all the experiments aimed at detecting interactions of solar axions with a target are not yet sensitive enough to probe the QCD axions parameter space not excluded by astrophysical bounds [127].

2.3.3 Cosmological axions search

In the right mass range ($m_A \sim 20\mu$eV), the axion can account for the entire dark matter density of the Universe [127]. In this mass range a detection would be troublesome for conventional experiments, but Pierre Sikivie in 1983 showed a viable path to axion dark matter detection by employing a microwave cavity permeated by a strong magnetic field [145]. In such a cavity the axions could resonantly convert, leading to a detectable quasi-monochromatic microwave signal [127].
These experiments usually fall under the name of haloscopes. A prime example of a haloscope is the ADMX experiment, which has set limits for the QCD axion (KSVZ model) in the 1.9–3.53 μeV mass range [146, 147]. A new type of haloscopes, called dielectric haloscopes [148], are also being developed and will investigate the 40–400 μm mass range in the next future. One example of a dielectric haloscope is the MADMAX experiment [149].

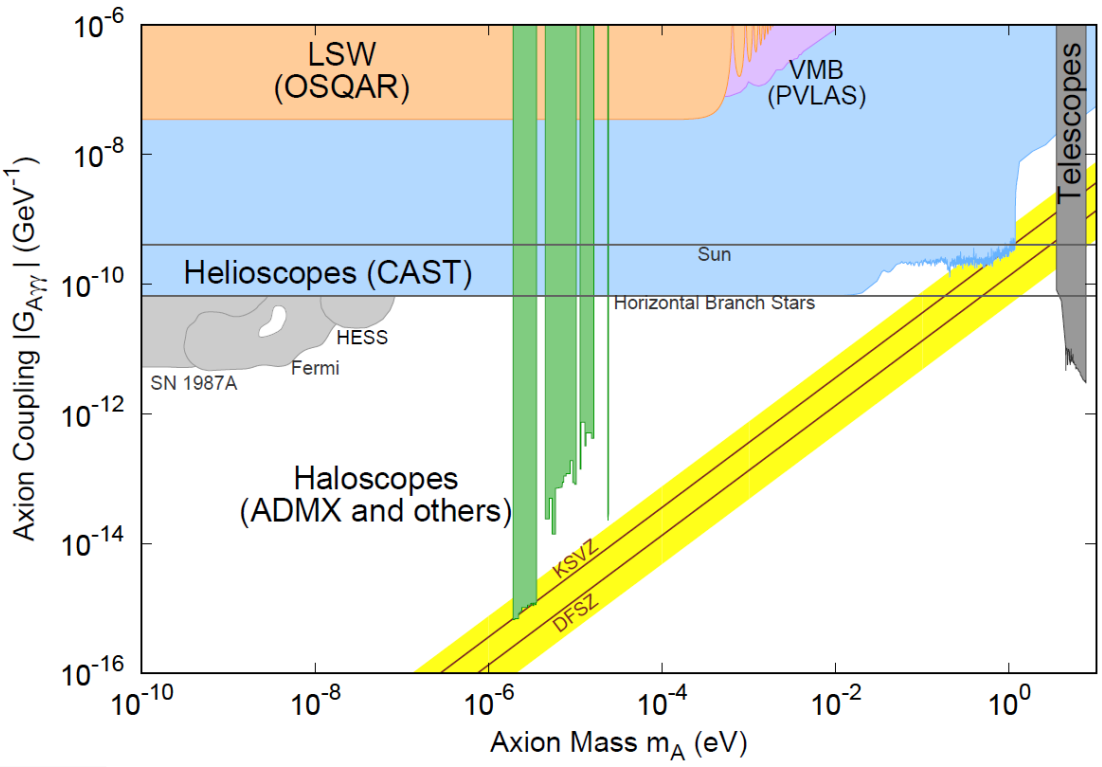

Figure 2.13: Summary of limits and bounds set on the axion-photon coupling $G_{A\gamma\gamma}$ versus the axion mass m_A by various experiments and astrophysical observations. Helioscopes are more effective probes than LSW and photon polarization experiments at all masses. Haloscopes are more effective than helioscopes at probing $\sim \mu$eV axions. For masses $\gtrsim 10^{-2}$ eV, experiments studying the interaction of axions with an experimental target can be a viable path, but they are currently not surpassing existing cosmological bounds. Figure from [36].

Chapter 3

Cryogenic detectors for astroparticle physics

Cryogenic detectors, often called low-temperature calorimeters or bolometers, are one of the most important type of detectors in the field of astroparticle physics. These detectors are particularly useful because of their excellent energy resolutions and low energy thresholds. However, they also require challenging operation environments and are difficult to employ in large-scale experiments.
In this chapter, the detection principles and the possible applications of these detectors will be presented along with their advantages and limits.

3.1 Design principles

The basic concept of a cryogenic detector is extremely simple and yet very effective. A solid-state absorber, also called target, is instrumented with a thermometer and connected to a thermal reservoir commonly referred as thermal bath. When a particle interacts in the absorber, there is the production of phonons, collective excitations associated to the vibrational modes of a crystal lattice. These phonons have energies ranging from μeV, in case of *thermal* phonons, to meV, in case of *athermal* phonons (also referred to as *nonequilibrium* or *nonthermal* phonons) [150]. The only requirement to detect a signal induced by a particle is that the thermometer must be sensitive enough to distinguish the phonons generated in a particle interaction over the thermal phonon noise. For this reason, these devices are normally operated at cryogenic temperatures $\lesssim$50 mK.
Let now consider an absorber with heat capacity *C(T)* connected to a thermal bath with temperature T_0 through a thermal conductance *G(T)*, see Figure 3.1. Then, an incident particle depositing an energy E will produce a rise in temperature:

$$\Delta T = \frac{E}{C(T)} e^{-\frac{t}{\tau(T)}} \tag{3.1}$$

where $\tau(T) = C(T)/G(T)$.
The main piece of information given by Equation 3.1 is that this detector works if *C(T)* is small enough.

Now, for an ideal dielectric crystal, the heat capacity can be expressed as:

$$C = 9Nk_B \left(\frac{T}{T_D}\right)^3 \int_0^{T/T_D} \frac{x^4 e^x}{(e^x - 1)^2} dx \tag{3.2}$$

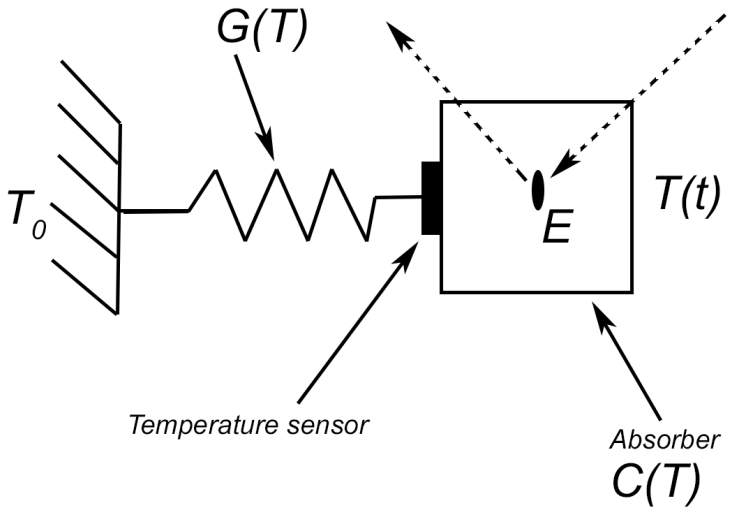

Figure 3.1: Sketch of a typical cryogenic detector. An absorber with heat capacity *C(T)* is connected to a thermal bath at a temperature T_0 through a thermal conductance *G(T)*. A temperature sensor is coupled to the absorber such that it can measure it temperature changes. In case of a particle interaction in the absorber, the energy deposited in the interaction is detected by measuring the temperature rise of the absorber.

where N is the number of nuclei, k_B is the Boltzmann constant, and T_D is the Debye temperature. For a material with a Debye temperature high enough at a temperature low enough, such that $T_D \gg T$, Equation 3.2 becomes [151]:

$$C = 1944 \left(\frac{M}{m}\right) \left(\frac{T}{T_D}\right)^3 \tag{3.3}$$

where M is the molecular weight of the absorber and m its mass.
From Equation 3.3 we can immediately see that the requirement for a successful experiment in this simple model, apart from operating the detector at the lowest possible temperature, is to employ an absorber with a large T_D.
The energy resolution $\sigma(E)$ of this kind of detectors is determined by two different factors: the fluctuations in the intrinsic phonon background of the absorber and the fluctuations of the phonons created in a particle interaction of a given energy [150]. The phonon noise in the absorber does not depend on the energy deposited by a particle interaction, but is a property of the detector. For a 10 g germanium crystal at 10 mK it can be calculated to be ∼1 eV [150]. The phonon fluctuations due to an energy deposition have a sub-dominant effect in an ideal detector and are estimated to be ∼0.03 eV for E=1 keV [150]. However, in a real detector part of the energy deposited could be lost due to the escape of electrons and photons, part could be trapped in metastable states, and part could be missed due to a slow thermalization of the athermal phonons.
Even in the real detector scenario, these devices offer nearly unmatchable energy resolutions and energy thresholds. Furthermore, they rely on the measurement of heat in the target, while most of other detectors require the ionization of the target. This means that in the case of low-ionizing or non-ionizing particles they

still guarantee an accurate energy reconstruction. Finally, a wide variety of material can be employed as absorbers.
The drawbacks of these detectors is that they need to be operated at extremely low temperatures, usually achieved with dilution refrigerators [152], and that the maximum size of a detector is somewhat limited. In fact, it is challenging to develop large size crystals and the heat capacity increases proportionally to the mass of the absorber. For this reason, in order to achieve a large exposure, experiments usually employ arrays of nearly identical ∼1–1000 g detectors.

3.1.1 Equilibrium thermal detectors

The design principle just described is the basis of equilibrium thermal detectors [153]. These detectors are usually designed in a way that any energy deposition inside the absorber is thermalized on timescales shorter than $\tau(T) = C(T)/G(T)$ [70]. These detectors can be operated in two different modes: calorimetric or bolometric.
If the equilibrium detector is used to measure an energy deposited E in the absorber by a particle, it is usually considered a calorimeter. In this case the energy deposition is well thermalized in the absorber, such that all excitations from the interaction are allowed to decay to near thermal equilibrium [154]. Meanwhile, a perfectly-coupled thermometer measures the temperature change in the absorber, before the absorber-thermometer system is returned to the initial state through the weak thermal link to the thermal bath [153]. Equilibrium calorimeters are employed for all applications requiring extremely high energy resolutions, such as experiments measuring the beta decay endpoint with high precision to derive the neutrino mass [154, 155].
If, instead, the equilibrium detector is used to measure a constant power P deposited in the absorber, it is usually considered a bolometer. In this case:

$$\Delta T = \frac{P}{C(T)} e^{-\frac{t}{\tau(T)}} \tag{3.4}$$

Equilibrium bolometers are employed for all applications requiring high precision in power measurements, as for the measurements of the CMB radiation [70].

3.1.2 Nonequilibrium detectors

Thermal detectors can also be operated as nonequilibrium detectors. Most of the design principles described for equilibrium detectors also apply to this kind, however there is a key difference: in nonequilibrium detectors the signal is mostly driven by athermal phonons.
Nonequilibrium devices are faster compared to equilibrium detectors, since the thermal equilibrium can take a very long time to establish at low temperatures [153]. This is a great advantage for all the experiments that are negatively impacted by the pile-up.
In addition, nonequilibrium detectors can employ absorbers with larger heat capacity compared to equilibrium thermal detectors, since the athermal phonons carrying the signal are not thermalized within the absorber [70]. In fact, when a particle interacts within the absorber, high-frequency phonons are created. These phonons promptly decay into acoustical athermal phonons, which ballistically spread in an isotropic way inside the absorber and eventually interacting with the thermal sensor [70]. This is a key advantage for all the experiments which are heavily influenced

by the target mass employed, such as direct dark matter search and neutrinoless double beta decay experiments.
However, these clear advantages come at certain costs: nonequilibrium detectors may suffer from position dependence and achieve lower energy resolutions compared to equilibrium detectors [153].

3.2 Thermal sensors

The key component of a cryogenic detector is the thermal sensor. The thermal sensor has to measure the ΔT induced by a particle interaction and convert it into an electrical signal. Examples of thermal sensors are Metallic Magnetic Calorimeters (MMCs) [156], Neutron Transmutation Doped thermistors (NTDs) [157, 158], and Transition Edge Sensors (TES) [159]. All of these sensors can be used for the design of both equilibrium and nonequilibrium detectors.
The two type of thermal sensors that have been used for the experimental work presented in this thesis are NTDs and TES.

3.2.1 Neutron Transmutation Doped thermistors (NTDs)

The NTD is a small piece of a highly doped semiconductor [151]. As a result, the resistance is strongly dependent on the temperature, see Figure 3.2, which can be constantly monitored by measuring the voltage drop of the bias current running through the NTD [160].
NTDs are commonly produced from small germanium crystals which are doped by thermal neutron irradiation [150]: this method ensures an uniform doping and the production of a large amount of doping sites within the crystal.
This type of sensors have a wide variety of applications, ranging from direct dark matter search experiments, as in EDELWEISS [121], to neutrinoless double beta decay experiments like CUORE [161], and even astrophysical applications, like in the High Frequency Instrument of PLANCK [162].

3.2.2 Transition Edge Sensors (TES)

TES are a thin strip of a superconducting material directly deposited on the absorber. These strips can be made in almost any shape and size, employing a variety of materials such as aluminum, titanium, and tungsten [150].
TES are operated in the transition from the normal conducting phase to the superconducting phase, such that any small change in temperature corresponds to a large change in resistance, see Figure 3.3.
TES can offer higher sensitivities and lower energy thresholds compared to NTDs, but they are intrinsically subject to non-linear behaviour. Furthermore they have a more limited energy range of operation, since this parameter is strongly tied to the relatively small width of the transition, and a narrow temperature range where they can be operated.
TES have a wide variety of applications as well, from direct dark matter search experiments, such as SuperCDMS [120] and CRESST-III [122], to astrophysical applications, like in BICEP2 [165].

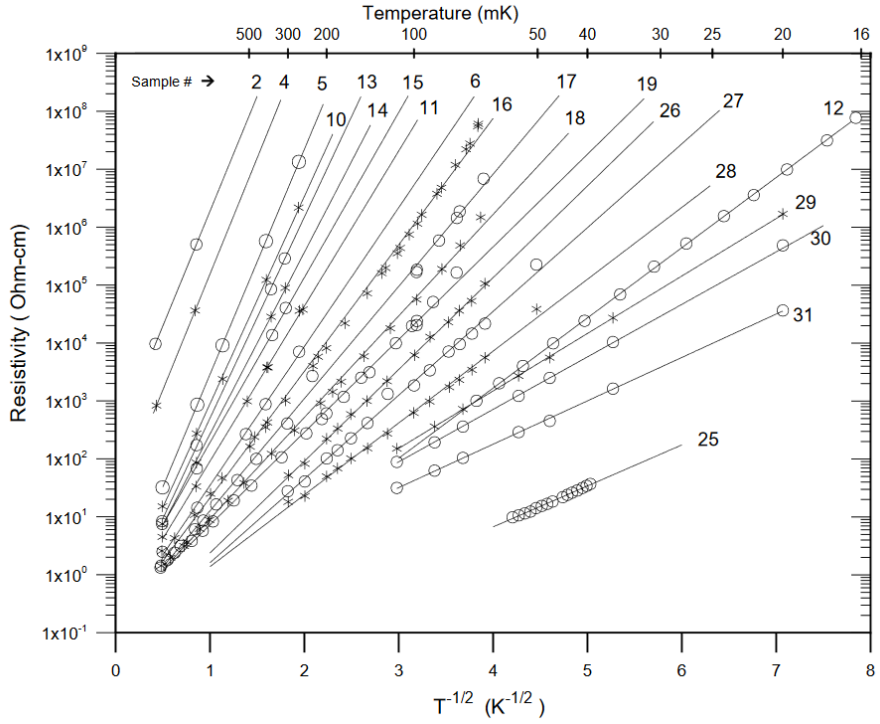

Figure 3.2: Resistivity as a function of temperature for multiple NTD germanium thermistors exposed to different neutron irradiation. Figure from [163].

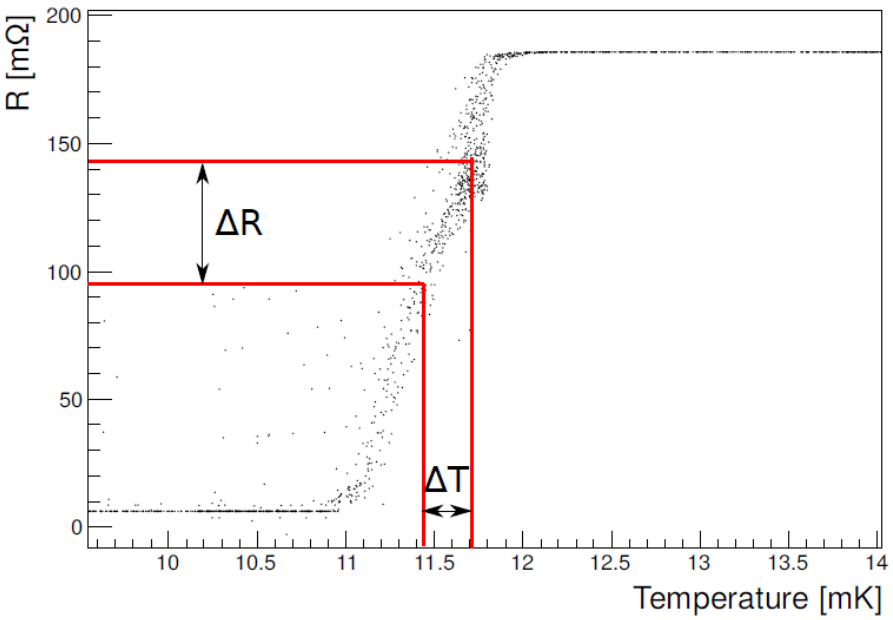

Figure 3.3: Resistance as a function of temperature for a tungsten TES. Figure from [164].

3.3 CRESST-III detectors

The work presented in this thesis was conducted in the framework of the CRESST experiment. As such, most of the techniques, solutions, and technologies used here are based upon the ones developed within the collaboration in the last two decades. For this reason, it is needed to introduce the CRESST detectors, with a special focus on the ones produced for the third generation of the experiment, CRESST-III [122].

CRESST-III employs (20×20×10) mm^3 $CaWO_4$ and Al_2O_3, scintillating absorbers instrumented with TESs. TESs can be made with a variety of superconducting materials, however, as we have seen in Section 3.1, it is desirable to operate the detector at the lowest viable temperature. For this reason, the TESs employed in CRESST are made of a single tungsten film. These tungsten TESs have a transition temperature T_C ∼15 mK, see Figure 3.3, which offers an ideal trade off between a low transition temperature and the possibility to steadily maintain the operation temperature in a dilution refrigerator.
On top of the tungsten layer, two aluminum pads are deposited with the double function of increasing the phonon collection efficiency and as bondpads for the aluminum wires through which the bias voltage is injected. The thermal conductance *G(T)* is realized with a deposited thin-gold stripe to be connected to the thermal bath via a gold bond wire. The thermal bath has to be kept at a temperature T_0 lower than the transition temperature, in order to be able to cool down the detector to the desired temperature of operation after each energy deposition. As such, the temperature can be locally set higher than T_0 thanks to a gold heater directly deposited on the vicinity of the TES. In fact, injecting a current through the heater allows to increase the temperature of each detector to its desired value. Once set, the operation temperature is then maintained over time thanks to a custom-made feedback loop. An energy deposition in the absorber induces variations of resistance of the TES, which are read out using a customized DC SQUID system [166].
A sketch of a typical CRESST-III TES is shown in Figure 3.4.

A CRESST-III detector is not only designed to detect the heat generated in a particle interaction within the absorber, but also to detect any scintillation produced in such interactions. As a result, each absorber is coupled with a CRESST-III light detector [167]. These light detectors are made of a thin (20×20×0.4) mm^3 sapphire crystal coated with a thin layer of silicon in order to enhance the absorption of the scintillation produced in the main absorber. Each light detector is instrumented with a TES similar to the one described above, but with a modified geometry in order to match the different crystal size.
The simultaneous measurement of heat and scintillation allows to perform particle discrimination, which is used to reject background-induced events. However, since only ∼2% of the total energy deposited by a particle is typically detected as a light signal [168], an effective particle discrimination at lower energies becomes impossible to achieve.

3.3.1 Signal creation in CRESST-III detectors

The cryogenic detectors employed by CRESST-III are typical nonequilibrium detectors which employ TESs as thermal sensors. A detailed thermal model describing the signal formation in a CRESST-like detector can be found in [169]. Two popula-

tions of phonons are relevant for the signal creation: the thermal and the athermal phonons.
The athermal phonon are spreading isotropically in the absorber after a particle interaction: when they enter the thermometer they are absorbed by the free electrons present in the thin film. Thus, the temperature of the thermometer increases, which leads to a detectable signal. However not all the energy carried over by the phonons can be detected, since part of the energy entering in the thermometer is subsequently lost via the thermal link and part is going back to the absorber in the form of thermal phonons.
Thermal phonons are the last stage into which phonons decay after being created in a particle interaction. The thermal phonons can also enter the thermometer and increase its temperature, but, due to the electron-photon decoupling, at low temperatures the sensor is much less sensitive to these phonons than to the athermal ones.
To sum up, the signal which can be detected after a particle interaction in the absorber is linked to the temperature variation of the electronic system of the thermometer and this temperature variation is induced by both the athermal and the thermal phonons. A typical pulse registered by a CRESST-like detector is then the sum of a higher and faster athermal component and a lower and slower thermal component [169].
Similarly to equilibrium thermal detectors, CRESST-like detectors can be used in two different modes: calorimetric or bolometric. The calorimetric mode, which is the one employed by CRESST-III detectors [122], is when the lifetime of athermal phonons is much shorter that the time it takes the film to thermally relax. The calorimetric mode offers a higher sensitivity, thus lower energy thresholds, than the bolometric mode.
The bolometric mode, which was employed in CRESST-II detectors [170], is the opposite case, when lifetime of the athermal phonons is much longer that the time it takes the film to thermally relax. The bolometric mode is characterized by a lower sensitivity than the calorimetric mode, but faster pulses, which can reduce the pile-up in the detector, allowing the employment of larger absorbers.

3.4 Cryogenic detectors for dark matter search

To introduce the applications of cryogenic detectors for direct dark matter search, it is instructive to understand the current state of the art in this field of research. As it is possible to see from Figures 3.5 and 3.6, liquid noble gas experiments dominate the experimental sensitivity for dark matter particles with masses $\gtrsim$5 GeV. In this mass range, cryogenic dark matter experiments simply cannot keep up with the large exposures offered by these experiments. However, liquid noble gas experiments are limited by the energy thresholds they can achieve, meaning that cryogenic experiments become competitive again when it comes to study light dark matter, especially in the sub-GeV mass range. This is true for the study of both spin-independent and spin-dependent interactions, with the exception that for spin-dependent interactions bubble chambers experiments can challenge liquid noble gas experiments.
This whole picture is somewhat limited to this current phase, with the community focused on the exclusion of large sectors of the parameter space. However, in case a positive signal is found, cryogenic detectors, provided that they can match the

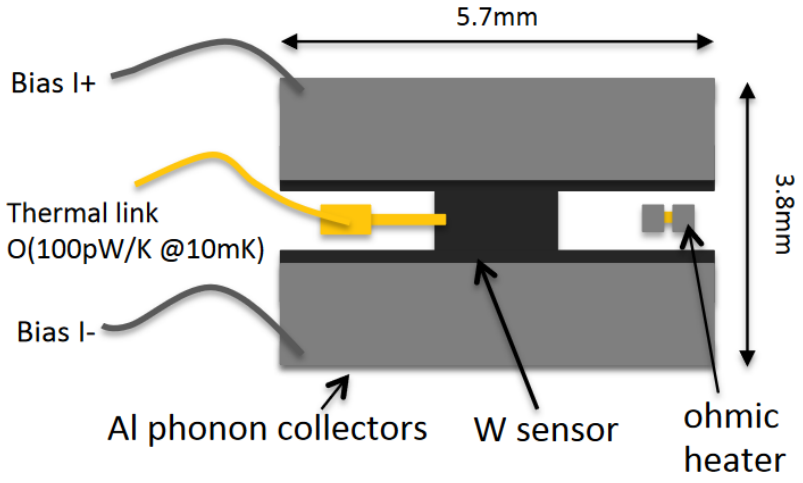

Figure 3.4: Sketch of a CRESST-III TES. In black the tungsten film with a T_C ∼15 mK. On top of this layer two aluminum pads, which serve also as phonon collector, are deposited. The thermal link between the TES and the thermal bath is realized with a thin strip of gold bonded with a gold wire. Finally, a heater is deposited close to the TES to locally increase the TES temperature to the desired point of operation. Figure from [171].

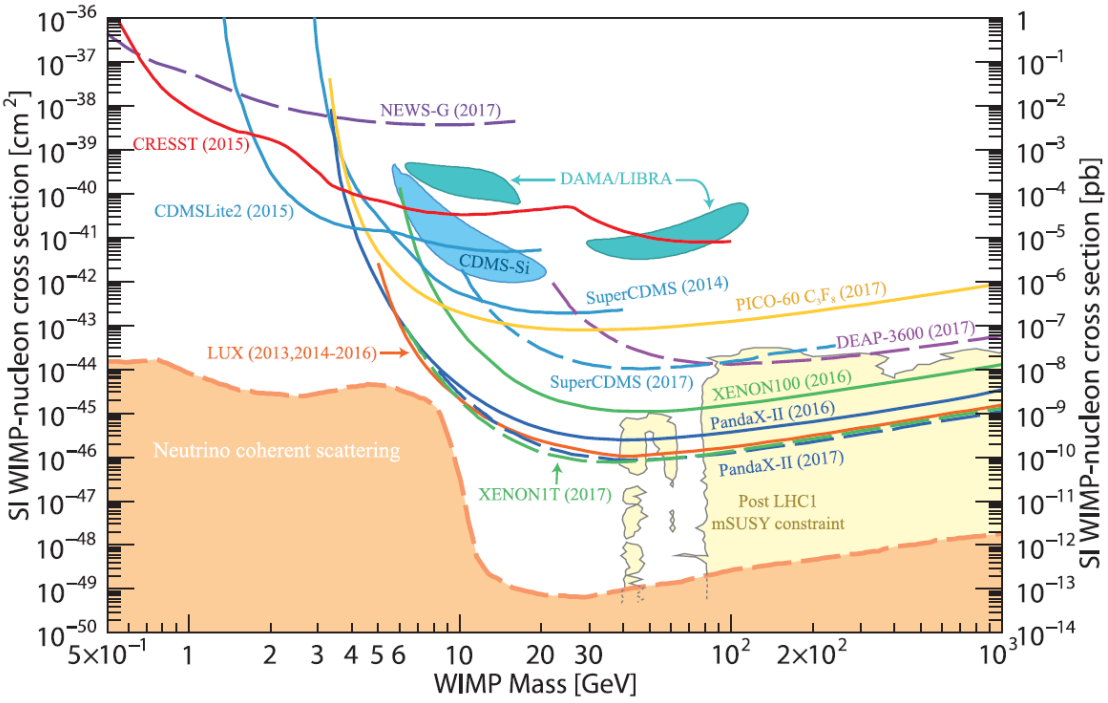

Figure 3.5: Limits set by various experiments on the spin-independent dark matter-nucleon cross section for dark matter masses in the 1–1000 GeV range. For masses $\gtrsim$5 GeV the sensitivity of liquid noble gas experiments is several orders of magnitude greater than the one achieved by the best experiments based on cryogenic detectors. Figure from [36].

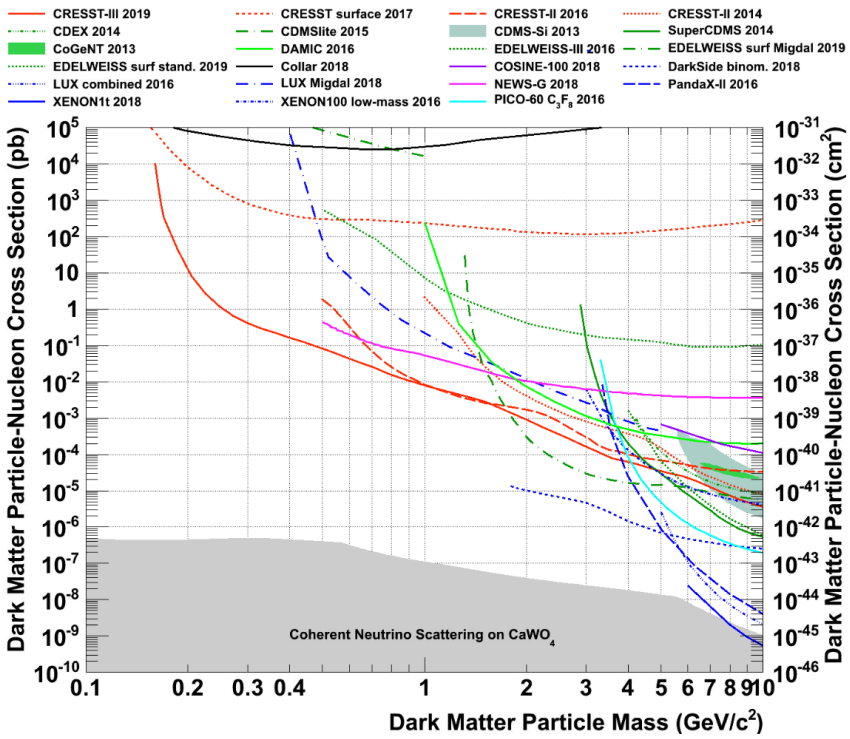

Figure 3.6: Limits set by various experiments on the spin-independent dark matter-nucleon cross section for dark matter masses in the 0.1–10 GeV range. In the sub-GeV range, CRESST-III is currently the leading experiment. Figure from [122].

liquid noble gas experiments exposure in the future, can become a powerful tool to study the properties of dark matter particles in the whole mass range thanks to their excellent energy resolution and flexibility in the target selection.
In the sub-GeV mass range, SPCs can offer similar advantages than cryogenic detectors, but they have also similar limitations regarding to the achievable exposure. The energy thresholds that cryogenic detectors can achieve are truly impressive. In the most extreme cases, they can detect elastic scatterings off the target nuclei with energy thresholds almost two orders lower than the best energy thresholds for liquid noble gas experiments. For example, a 23.6 g $CaWO_4$ crystal instrumented with a TES reached a 30.1 eV threshold [122], while a 33.4 g germanium crystal instrumented with a NTD thermistor recently reached a ∼60 eV threshold [172]. Despite these excellent performances, cryogenic detectors are as well limited in the exploration of light dark matter masses. Even assuming the best case scenario, a ∼1 eV threshold for nuclear recoils for a target containing ^{1}H, the minimum dark matter mass which can be studied is ∼10 MeV. For even lighter masses, one viable path to extend the search for dark matter-nucleon interactions might revolve around the study of inelastic nuclear recoils which can cause Bremsstrahlung [173] or Migdal effect [174]. Another viable path might instead contemplate the study of other type of interactions between a dark matter particle and the absorber, such as electron transitions and single phonon excitations [175].

3.5 Novel applications for CRESST-like detectors

CRESST-III is currently the leading cryogenic experiment for the direct search of sub-GeV dark matter. This is true for both the study of spin-independent and *neutron-only* spin-dependent interactions with ordinary matter [122].
Most of CRESST's success stems from the cutting edge technology for the deposition of superconducting thermometers developed over the years. One of the key advantage over other experiments of this technology is its flexibility, allowing the design of new detectors based on a vast number of targets. In fact, the absorbers traditionally employed in CRESST are $CaWO_4$ and Al_2O_3, but most dielectric materials can be employed in place of those absorbers. This is a somewhat unique occurrence among direct search experiments, since most are strictly tied to the experimental technique they developed and do not have a lot of room for the employment of new targets, with some notable exceptions such as the NEWS-G experiment [118]. Moreover, CRESST-like detectors based on the similar concepts of the one used for dark matter detection can be used for a variety of other experiments in astroparticle physics. In fact, they have recently been proposed for new experiments dedicated to the precise measurement of coherent elastic neutrino–nucleus scattering, see NUCLEUS [176], or the detection of neutrinos from core-collapse supernovae, see RES-NOVA [177].

In this thesis, the development of two different kinds of CRESST-like detectors aimed at the exploration of new physics is presented. One set of prototypes were dedicated to the expansion of the dark matter search reach of the CRESST-III experiment, while the second set of prototypes was designed to study solar axions.

CRESST-III in its current form [122] is an experiment fully optimized for the investigation of spin-independent dark matter interactions, but to study spin-dependent interactions there is the need to employ absorbers containing specific isotopes that are sensitive to spin-dependent interactions. Furthermore, to effectively study these interactions in the sub-GeV mass range it is mandatory to select only light isotopes with high natural abundance. As such, the ideal target to probe spin-dependent interactions in the sub-GeV range would be ^{1}H for *proton-only* interactions and ^{9}Be for *neutron-only* interactions [99]. However, this poses a different problem, since crystals containing ^{1}H are not available.
One solution is to adopt the next best ideal target: ^{7}Li. ^{7}Li is extremely sensitive to *proton-only* spin-dependent dark matter interactions, has high natural abundance, is light, and is readily available in many different crystals that can be employed for dark matter search. Furthermore, lithium-containing crystal are also containing ^{6}Li, an isotope that can be used to study neutrons thanks to its relatively high neutron capture cross section. Since neutrons can be a problematic background for direct dark matter search, a lithium-containing crystal can have in principle many advantages: it can probe spin-independent and spin-dependent interactions simultaneously, while also detecting the flow of neutrons directly inside the experimental setup. For all these reasons, in the past couple years a series of prototypes based on lithium-containing crystals were developed at Max Planck Institute for Physics in Munich, Germany. The first of these prototypes employed a Li_2MoO_4 absorber instrumented with a NTD thermistor. The work, presented in Chapter 4, has served as a proof of principle of the potential for a detector of this kind, with the first results for spin-dependent dark matter interactions in the sub-GeV range obtained with a cryogenic detector. However, to develop detectors similar to the ones currently em-

ployed by the CRESST-III experiment, it was necessary to replace Li_2MoO_4 with a crystal not affected by a large higroscopicity, which was preventing the deposition of CRESST-like TESs on the absorber. This problem prompted the characterization of a novel absorber for cryogenic detectors, $LiAlO_2$, which is presented along with improved dark matter results in Chapter 5. This crystal was also used to build a large prototype for the measurement of neutrons in underground laboratories and those results are also presented in the same chapter.

The second part of the thesis is dedicated to the development of a detector prototype designed to detect solar axions. The principle of detection, the resonant absorption of solar axions by ^{169}Tm, was already adopted recently by some small scale experiments [144, 178]. A solar axion flowing through a thulium-containing material can be absorbed causing the excitation of the nuclear state of ^{169}Tm to the first excited state. At this point, ^{169}Tm relaxes back to its nuclear ground state emitting a 8.41 keV photon, which can be detected by various photon sensors. However, the previous experiments were severely limited by their detection efficiency and by their small exposure. This is mostly due to the fact that ^{169}Tm, the source of the signal in the case of a solar axion absorption, was not embedded in the detector, but was measured with a photon sensor placed at a certain distance. Cryogenic detectors can easily solve these problems while also ensuring a high energy resolution in the keV range. In fact, since ^{169}Tm is contained in the absorber, the detector efficiency is close to 1 and the experimental exposure can be increased by the development of an array of detectors.
In Chapter 6 the development of a cryogenic detector based on a $Tm_3Al_5O_{12}$ crystal is presented. This crystal was instrumented with a NTD thermistor to study its cryogenic properties and in this work it was possible to acquire the first calibrated energy spectrum with a detector of this kind. After this, there was a development aimed at reaching the experimental design required to investigate solar axions. For this reason, a CRESST-like TES was deposited on a $Tm_3Al_5O_{12}$ absorber and the detector was tested for the first time at Max Planck Institute for Physics. The detector matched the required specifications and as such it was possible to derive competitive limits for solar axions, as shown in Chapter 7.

Chapter 4

Results on spin-dependent dark matter interactions with Li_2MoO_4

The content of this chapter was published as a collaborative effort in The European Physical Journal C (see [179]).
I wrote the majority of Sections 4.2, 4.4, 4.5, 4.6.
I designed the copper holder used for this cryogenic detector and, with the supervision of my day-by-day supervisor Dr. Michele Mancuso, I glued the NTD sensor, bonded the Light Detector, assembled the detector module. Together, we installed the detector module in the dilution refrigerator, operated the dilution refrigerator, installed the calibration source, and acquired the data.
My main original contribution is, in general, the idea to use ^7Li for studying sub-GeV dark matter interactions. In this regard, I independently performed back-of-the-envelope calculations showing that the data acquired would lead to a competitive result with the respect of existing experiments. In this process, I also spent a substantial amount of time studying the existing literature in order to find the appropriate spin-coefficients to use for the limit calculations. The theoretical framework was fully developed by Dr. Vanessa Zema, who wrote the relevant section of this paper.
I triggered the data acquired. Subsequently, me and Dr. Michele Mancuso performed independent analysis of the background data, reaching consistent conclusions. From the obtained energy spectrum, our colleague Dr. Florian Reindl derived the dark matter limits presented in this work.
I personally analyzed the calibration data obtained with the ^{57}Co γ-source, deriving the calibration factor used for the energy spectrum. As such, I prepared Figure 4.2.

4.1 Abstract

In this work, we want to highlight the potential of lithium as a target for spin-dependent dark matter search in cryogenic experiments, with a special focus on the low-mass region of the parameter space.
We operated a prototype detector module based on a Li_2MoO_4 target crystal in an above-ground laboratory. Despite the high background environment, the detector sets a competitive limit on spin-dependent interactions of dark matter particles with protons and neutrons for masses between $0.8\,GeV/c^2$ and $1.5\,GeV/c^2$.

4.2 Introduction

In recent decades a significant experimental effort has been dedicated to the direct search of dark matter by multiple experiments. Most searches have focused on the dark matter particle mass range between $\sim$10 GeV/c^2 and $\sim$100 GeV/c^2 [160], but recently an increasing interest points towards models involving lighter particles [61, 180, 57]. More emphasis is also being given to interactions between dark matter particles and ordinary matter beyond the classic spin-independent interactions [181, 182, 93, 183]. In this work we present a first investigation of spin-dependent interactions in the low dark matter particle mass range using well established cryogenic detection technologies with a target crystal containing lithium. To our knowledge, lithium has previously been used only in [184] and [140] for direct dark matter detection.

The cryogenic detector technology used for direct detection of dark matter has demonstrated to be ideal to probe spin-independent interactions in the low mass ($\lesssim$ 10 GeV/c^2) parameter space. Different target materials are used by various experiments: CRESST opted for $CaWO_4$ [122], EDELWEISS for germanium [185], and CDMS based its technology on both germanium and silicon [120]. However, this technology is not yet fully exploited to investigate spin-dependent interactions in the very same region of the parameter space due to the target materials employed. Light elements are in general penalized in probing spin-independent cross sections for dark matter-nucleus elastic scattering because the expected rate scales with the square of the mass number ($\sim A^2$) [186]. This disadvantage is in part mitigated by kinematics for low dark matter masses: the lighter the element, the larger the transferred momentum due to elastic scattering of dark matter particles on nuclei. On the other hand, for spin-dependent interactions the expected rate is proportional to the nucleon spin coefficients ($\sim \langle S_{p/n} \rangle^2$), which differ from one isotope to the other and do not favour heavy ones [99]. Spin-dependent interactions can be tested only on isotopes with a nuclear ground state angular momentum $J_N \neq 0$ [86, 187, 98], therefore only a restricted number of elements fulfills this requirement. Since the scattering kinematics remains the same as in spin-independent interactions, it follows that certain light elements are potentially highly favoured to probe the low mass spin-dependent dark matter parameter space ($\lesssim$ 10 GeV/c^2). Hence, the ideal target to test spin-dependent interactions should be constituted of an element with $J_N \neq 0$, $\langle S_{p/n} \rangle = 1/2$, and the lowest possible mass.

Currently, lithium is the lightest element contained in inorganic crystals that can be operated at cryogenic temperatures [188, 184, 189, 190, 191]. Its most abundant isotope is ^{7}Li (92.41% natural abundance [192]) with nuclear angular momentum $J_N = 3/2$ and $\langle S_p \rangle$ close to 1/2 [99]. For all these reasons, lithium-based crystals are very well suited to probe spin-dependent interactions. Other light elements which can be competitive for spin-dependent dark matter search at low masses are hydrogen, which can be found in organic liquid scintillators [193], and helium, which could be employed in a gaseous ionization detector.

We present the cryogenic operation of a prototype detector module based on a Li_2MoO_4 target crystal, which was originally developed for the CUPID-0/Mo experiment (the very same crystal is labeled *LMO-3* in [194]). The results presented in this work set the most stringent limits with cryogenic detectors for spin-dependent dark matter interactions with protons below 1.5 GeV/c^2.

4.3 Theoretical Framework

In the scenario typically assumed to calculate the sensitivity of a given direct detection experiment [122, 195, 196, 197, 198, 199, 200, 172], a spin 1/2 dark matter particle interacts with the nuclei of the target. At quantum level, the dark matter particle interacts with the quarks and these interactions are mediated by a heavy boson. In this framework, the differential spin-dependent elastic cross section of dark matter particles with nuclei is proportional to the non-relativistic limit of the transition amplitude between initial and final states of the axial-vector current term [98, 96]. In most dark matter scenarios the event rate is dominated by the spin-independent cross sections, which tends to explain why the majority of the existing experiments are designed to probe this type of interactions. However, it has been shown that in some models spin-dependent interactions can provide the largest contribution to the event rate [101]. These types of scenarios strongly motivate the investigation of spin-dependent dark matter interactions.

The differential spin-dependent cross section as function of the transferred momentum q is [97, 98, 86]:

$$\frac{d\sigma^{SD}}{dq^2} = \frac{8G_F^2}{(2J_N+1)v^2} S_A(q) \tag{4.1}$$

where G_F is the Fermi coupling constant, J_N is the nuclear ground state angular momentum, v is the dark matter particle-nucleus relative velocity, $S_A(q)$ is the axial-vector structure function. The axial-vector structure function is

$$S_A(q) = a_0^2\, S_{00}(q) + a_0 a_1\, S_{01}(q) + a_1^2\, S_{11}(q) \tag{4.2}$$

where a_0 and a_1 are the coefficients of the isoscalar-isovector parametrization of the quark axial-vector current computed among the initial and final nuclear states and $S_{ij}(q)$ are functions obtained by nuclear calculations. The value of these coefficients depends on the dark matter-quark interaction model. Even considering the maximum transferred momentum q_{max}, i.e. q evaluated at the escape velocity v_{esc} and for dark matter mass m_χ equal to the mass of the nucleus m_N, the axial-vector structure function for light nuclei is anyhow $S_A(q_{max}) \simeq S_A(0)$, therefore we can safely assume the $q^2 \to 0$ limit, that is equivalent to assume a form factor $F(q) = S_A(q)/S_A(0) = 1$. In this limit,

$$S_A(0) = \frac{(J_N+1)(2J_N+1)}{4\pi J_N} |(a_0+a_1)\,\langle S_p\rangle + (a_0-a_1)\langle S_n\rangle|^2 \tag{4.3}$$

where $a_p = a_0 + a_1$ and $a_n = a_0 - a_1$. The fixed values $a_p = 2$, $a_n = 0$ and $a_p = 0$, $a_n = 2$ (equivalent to $a_0 = a_1 = 1$ and $a_0 = -a_1 = 1$) are commonly imposed for convenience and labeled as *proton-only* and *neutron-only* interactions, respectively. Finally, $\langle S_p\rangle$ and $\langle S_n\rangle$ are the spin matrix elements arising from the *proton-only* and *neutron-only* interactions. These spin matrix elements are a key factor to accurately calculate the cross sections for spin-dependent interactions, but, despite modern developments in the estimation of the nuclear matrix elements (e.g. including two-body currents, as in [96]), the only available literature on lithium is still the one cited in [99]. We will refer to the most advanced calculation ($\langle S_p\rangle = 0.497$, $\langle S_n\rangle = 0.004$) [201] to derive the experimental results presented in this work. The lack of updated calculations can likely be attributed to the absence of lithium-based

experiments in the current panorama. In light of this work, however, we strongly encourage the computation of the nuclear matrix elements for ^{6}Li (7.59% natural abundance [192]) and ^{7}Li (92.41% natural abundance [192]) employing up-to-date techniques.
With this premise, we can compute the expected differential count rate for dark matter-nuclei spin-dependent interactions [202]. Taking into account all the numerical coefficients, the number of counts per (kg·keV·day) for dark matter spin-dependent interactions is

$$\frac{dR}{dE_R} = \frac{\xi}{A}\left(\frac{\rho_0}{m_\chi}\right) 2m_T \left(\frac{J_N+1}{3J_N}\right)\left(\frac{\langle S_{p/n}\rangle^2}{\mu^2_{p/n}}\right)\sigma^{SD}_{p/n}\eta(v_{min}) \tag{4.4}$$

where E_R is the recoil energy, A the target mass number, and ξ a normalization factor; $n = \rho_0/m_\chi$ is the number density of incoming particles, where ρ_0 is the local dark matter mass density and m_χ the dark matter mass; m_T is the target mass, $\mu^2_{p/n}$ the nucleon-dark matter reduced mass, and $\sigma^{SD}_{p/n}$ the dark matter-proton/neutron cross section. Finally, $\eta(v_{min})$ is the mean inverse velocity in the Standard Halo Model [203] where v_{min} is the minimal velocity required to transfer a recoil energy E_R [204].

4.4 Experimental setup

We operated a small scintillating crystal of Li_2MoO_4 with a size of (10×10×10) mm^3 and mass of 2.66 g as cryogenic detector. The crystal constitutes the main absorber of a scintillating cryogenic calorimeter detector module [171]. This detector was operated at the Max Planck Institute (MPI) for Physics in Munich, Germany, in a dilution refrigerator Kelvinox400HA from Oxford Instruments installed in an above-ground laboratory without shielding against environmental and cosmic radiation (see [205] and references therein for details of the cryogenic infrastructure).

The Li_2MoO_4 crystal is held in a copper holder using bronze clamps. The internal surfaces of the holder are covered by a reflector[1] to enhance the light collection efficiency. The crystal is instrumented with a (1×1×3) mm^3 Neutron Transmutation Doped (NTD) germanium thermistor [157] glued[2] on one surface: this sensor measures temperature variations induced by particle interactions inside the target crystal. Li_2MoO_4 is also a scintillator at cryogenic temperatures [188, 206], so a fraction of the energy deposited by particle interactions is converted into scintillation light. The light is detected using a CRESST-III light detector (LD) [167], made of a (20×20×0.3) mm^3 sapphire wafer coated on one face with a 1 μm thick silicon layer (Silicon-on-Sapphire, SOS) where a Transition Edge Sensor (TES), used as thermal sensor, is deposited. The sapphire side of the LD is facing the upper side of the Li_2MoO_4 crystal. Electrical and thermal connections are provided to the LD and the NTD via 25 μm diameter aluminum and gold bond wires, respectively. The temperature of the NTD is read out by measuring the voltage drop of the sensor with a commercial differential voltage amplifier [3] while applying a constant bias current through the NTD. The readout of the LD, instead, is obtained with a commercial

[1] 3M's Vikuiti^{TM} Enhanced Specular Reflector
[2] GP 12 Allzweck-Epoxidkleber
[3] Stanford Research System https://www.thinksrs.com/products/sr560.html

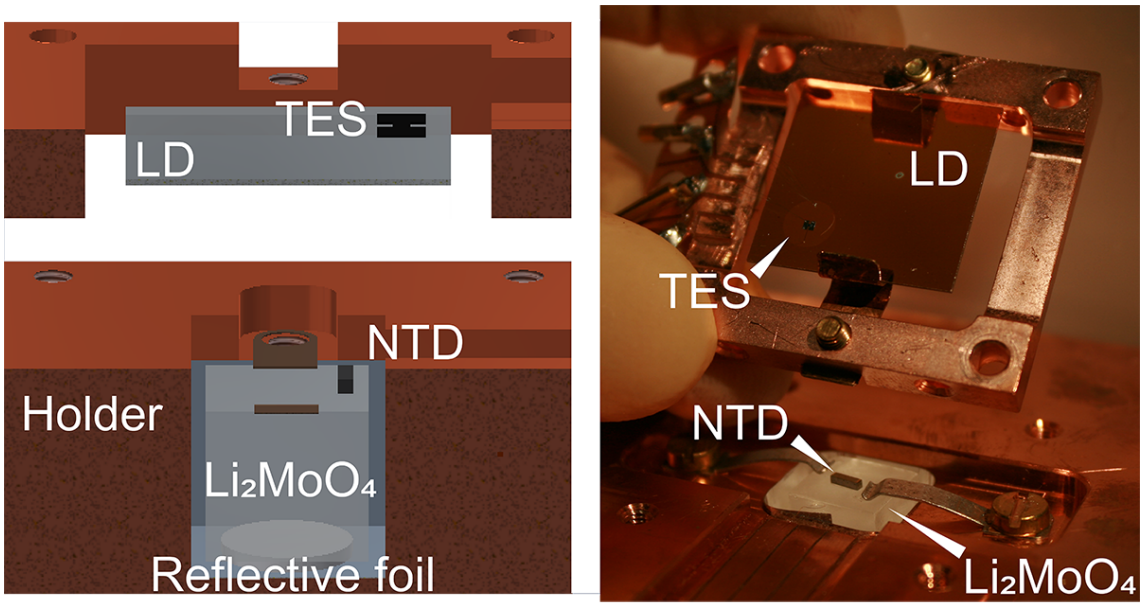

Figure 4.1: **Left**: section view of the detector module. **Right**: picture of the detector module. The Li_2MoO_4 crystal sits on a piece of PTFE inside a reflective cavity and is held in position with two bronze clamps. One NTD of $(1\times1\times3)\,mm^3$ is glued on the top surface of the crystal and is used as thermal sensor for signal read-out. A $(20\times20\times0.3)\,mm^3$ wafer of silicon-on-sapphire is used as light absorber, its frame is fixed on top of the target crystal. The thermal sensor is a TES directly deposited on the silicon coated side of the silicon-on-sapphire plate.

SQUID [4] system, combined with a CRESST-like detector control system [166]. An ^{55}Fe X-ray source with an activity of 0.055 Bq was placed about 0.5 cm away from the light detector to calibrate its energy response.
The two detectors were combined to constitute a detector module (Figure 4.1): this module was then mechanically and thermally connected to the coldest point of the dilution refrigerator, which retained a temperature of ∼10 mK during the whole data collection. This temperature is optimal for the NTD operation, but not for the LD. This particular TES, in fact, showed a critical temperature of $T_c = 22$ mK. Hence, the operating point of the LD had to be stabilized around T_c using a heater made of a thin gold film directly deposited in proximity to the TES.
Three measurement campaigns were performed: a gamma calibration, a neutron calibration, and a background measurement. First, a ^{57}Co γ-source was placed outside the cryogenic system for gamma calibration, which resulted in two visible lines in the spectrum at 122 keV and at 136 keV. Then, an AmBe source was placed in a similar position for neutron calibration. Finally, we removed the source to collect 14.77 hours of gross background data before the end of the measurement.
The two spectra computed in the 1–500 keV energy range for 3.3 hours each of stable phonon detector operations are shown in Figure 4.2. The phonon detector shows a consistent pulse shape up to MeV energy scale. The detector response is calibrated on the 122 keV and 136 keV peaks using a linear regression with the y-intercept constrained to 0 and the first order coefficient as a free parameter. We also observe a third peak due to an ^{241}Am contamination inside the set-up in all

[4] Applied Physics System model 581 DC SQUID

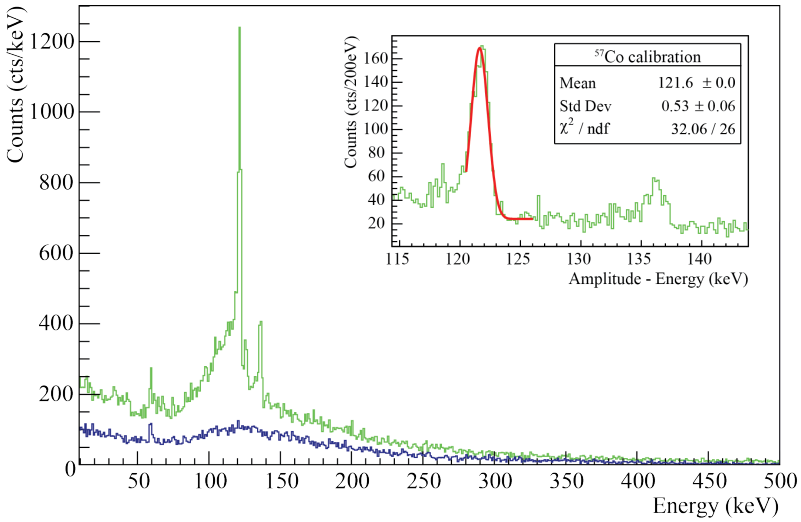

Figure 4.2: **Green**: measured spectrum using a ^{57}Co γ-calibration source in 3.3 hours. **Blue**: spectrum from 3.3 hours of background measurement. A bump peaks around 120 keV due to environmental radioactivity and a line appears at 59.5 keV due to an ^{241}Am contamination inside the setup. The two prominent peaks visible only in the green plot correspond to the 122 keV and the 136 keV γ rays of the ^{57}Co source: this region of the spectrum is also visible in the inlay in the top right corner, where the fit of the 122 keV peak is shown.

three measurement campaigns. Using the calibration factor obtained with the fit, the ^{241}Am γ-line appears at (59.5±0.2) keV, which matches the expected value of 59.54 keV [207]. For this reason and given the response function of an NTD [157], we can safely assume that the energy response is linear in the 0-136 keV range. After calibration, we quote the response of the NTD as (848±11) nV/keV. The energy resolution at zero energy, also denoted as baseline resolution, is $\sigma_{baseline}$ =(0.174±0.006) keV and the energy resolution at 122 keV is σ_γ =(0.53±0.06) keV. We also observe the 4.78 MeV thermal neutron capture peak of ^{6}Li which has a resolution of $\sigma_{n_{cap}}$ =(2.36±0.14) keV. The aforementioned energy resolutions are obtained via a Gaussian fit where standard deviation, center position, and amplitude are free parameters. The measured background rate is 2.37×10^4 counts/(keV·kg·day) in the 1–200 keV range. The LD is calibrated on the 5.89 keV peak of ^{55}Fe and has a baseline resolution $\sigma^{LD}_{baseline}$=(5.90±0.13) eV. The detector module shows a light yield (LY) for β and γ particles of (0.32±0.01) keV/MeV. The LY was computed as the ratio of the scintillation light detected in the LD converted in energy over the total energy deposited in the main absorber. The value we obtained is lower than previous cryogenic measurements with a similar crystal [194, 208]: we attribute this discrepancy to the different experimental setup (i.e. different LD and different geometry). The resulting quenching factors [209] are 0.205±0.007 for α particles and 0.124±0.012 for nuclear recoils induced by neutrons as seen during the neutron calibration, in agreement with the literature [194].

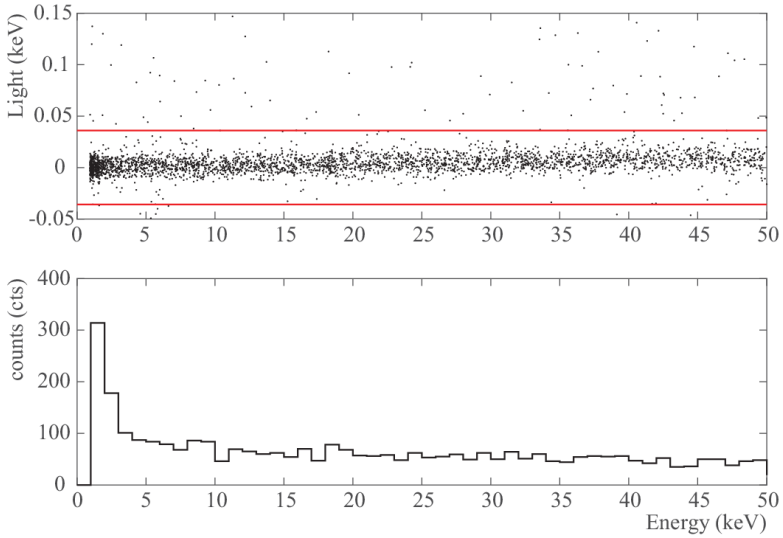

Figure 4.3: **Top**: the light measured in coincidence by the LD (y-axis) is displayed against the energy deposited in the Li_2MoO_4 crystal (x-axis) in the ROI (1-50 keV). The two lines in solid red correspond to the values chosen for the anti-coincidence cut: the events which fall inside the two lines are accepted for the dark matter analysis. The rejected events show an excessive light signal, which cannot be attributed to single particle hits in the main absorber. **Bottom**: measured energy spectrum of the selected events. Those events can mainly be attributed to low energy γ rays.

4.5 Dark Matter Results

The spin-dependent dark matter limits we present were calculated using the background measurement dataset. The results obtained should be seen as an evidence of the high potential of lithium-based crystals, rather than a conclusive outcome. For this very reason we decided to adopt a conservative approach for the data analysis and to collect only a few hours of background data. There would be no major benefit to aim for a longer data taking and for a more stringent data selection, since we are intrinsically limited in a non-shielded above-ground laboratory.

The energy region of interest we chose to compute our dark matter results is ranging from threshold to 50 keV. Due to the poor LY, in this energy range we cannot perform a particle identification analysis. Thus, the light signal is used only as a veto for muons and events originating from the materials surrounding the crystal. We expect dark matter particles to directly interact only with the Li_2MoO_4 crystal, but never with both the crystal and the light detector simultaneously. For this reason we define a region of interest (ROI) in the two dimensional space described by the energy deposited in the crystal on the x-axis and the energy deposited in the LD on the y-axis (see Figure 4.3, top). The ROI is defined on the x-axis by the energy region of interest. On the y-axis, instead, we set the maximum and the minimum values as C and -C respectively, where C is defined as

$$C = L_{max} + 2 \cdot \sigma_{\gamma}^{LD} = 39.2 \text{ eV} \tag{4.5}$$

This definition takes into account the maximum scintillation expected in the energy region of interest L_{max} and the energy resolution of the light detector σ_{γ}^{LD}.
L_{max} is simply obtained by the multiplication of the LY with the maximum value

in the energy region of interest:

$$L_{max} = LY \cdot 50\text{keV} = 12.8 \text{ eV} \tag{4.6}$$

Finally, the energy resolution σ_γ^{LD} =(10.0±1.6) eV is computed using the peak resulting from the scintillation generated by the absorption of 122 keV γ rays in the crystal during the ^{57}Co calibration. All the events falling inside the ROI are accepted for the dark matter analysis (see Figure 4.3, bottom) without further data selection.
The events falling outside the ROI are contributing to the dead time, hence the effective measurement time is reduced to 9.68 hours, which corresponds to a ^{7}Li exposure of 7.91×10^{-5} kg·day. The energy threshold of 0.932±0.012 keV has been determined according to the procedure described in [210]. Given the background induced by our setup, we set the threshold allowing a noise trigger rate (the rate of events caused by noise oscillation) of 1×10^4 counts/(keV·kg·day), which leads to a contribution in the first bin spectrum of approximately 10% of the total triggered events. The method we applied is valid in low-rate measurement conditions, a requirement we do not satisfy, therefore a higher trigger pedestal is expected mainly due to pileup.

We treat all events in the energy range between 0.932 keV and 50 keV as potential signal events, not performing any background subtraction and we conservatively calculate exclusion limits on spin-dependent interactions of dark matter particles with nuclei using Yellin's optimal interval method [211, 212] valid for *proton-only* interactions and for *neutron-only* interactions, as discussed in the theoretical framework presented before. For the calculation of the exclusion limits we adopt the standard dark matter halo model, which assumes a dark matter halo with a Maxwellian velocity distribution and a local dark matter density of $\rho_{\text{DM}} = 0.3\,\text{GeV}/(\text{c}^2 \cdot \text{cm}^3)$ [91]. We also assume $v_{\text{esc}} = 544\,\text{km/s}$ for the galactic escape velocity [89] and $v_\odot = 220\,\text{km/s}$ for the solar orbit velocity [213]. We tested the trigger efficiency generating a known flat energy spectrum of events. Each event is generated superimposing the ideal detector response, scaled to match the amplitude of simulated energy, on the recorded data. The simulated data is then processed with the same algorithm used for the real data. The fraction of survived events over the total simulated events at each energy represents the trigger efficiency, which was included in the calculation of the exclusion limits. Figure 4.4 shows the results obtained for *proton-only* and *neutron-only* interactions and the associated two-sigma statistical uncertainty. These results are extremely competitive with other spin-dependent direct dark matter searches for very light dark matter particles masses, especially in the sub-GeV/c^2 regime. For dark matter masses $\gtrsim 1.5\,\text{GeV}/\text{c}^2$ our results are not competitive with other direct search experiments, such as PICO-60 [200], CDMSlite [195], LUX [196], CDEX-10 [197], XENON1T [198], PandaX-II [199], due to the small exposure and the substantially higher background level, mainly caused by the above-ground operation in a non-shielded environment. Considering these sub-optimal conditions and reversing the argument, these results convincingly show the benefit of a comparable low threshold combined with a light target nucleus. The versatility to change the target material is a key feature of cryogenic detectors in general and CRESST-like readout in particular. This clearly yields the prospect of a quick advancement of sensitivities in the low-mass dark matter sector for spin-dependent interactions in the near future.

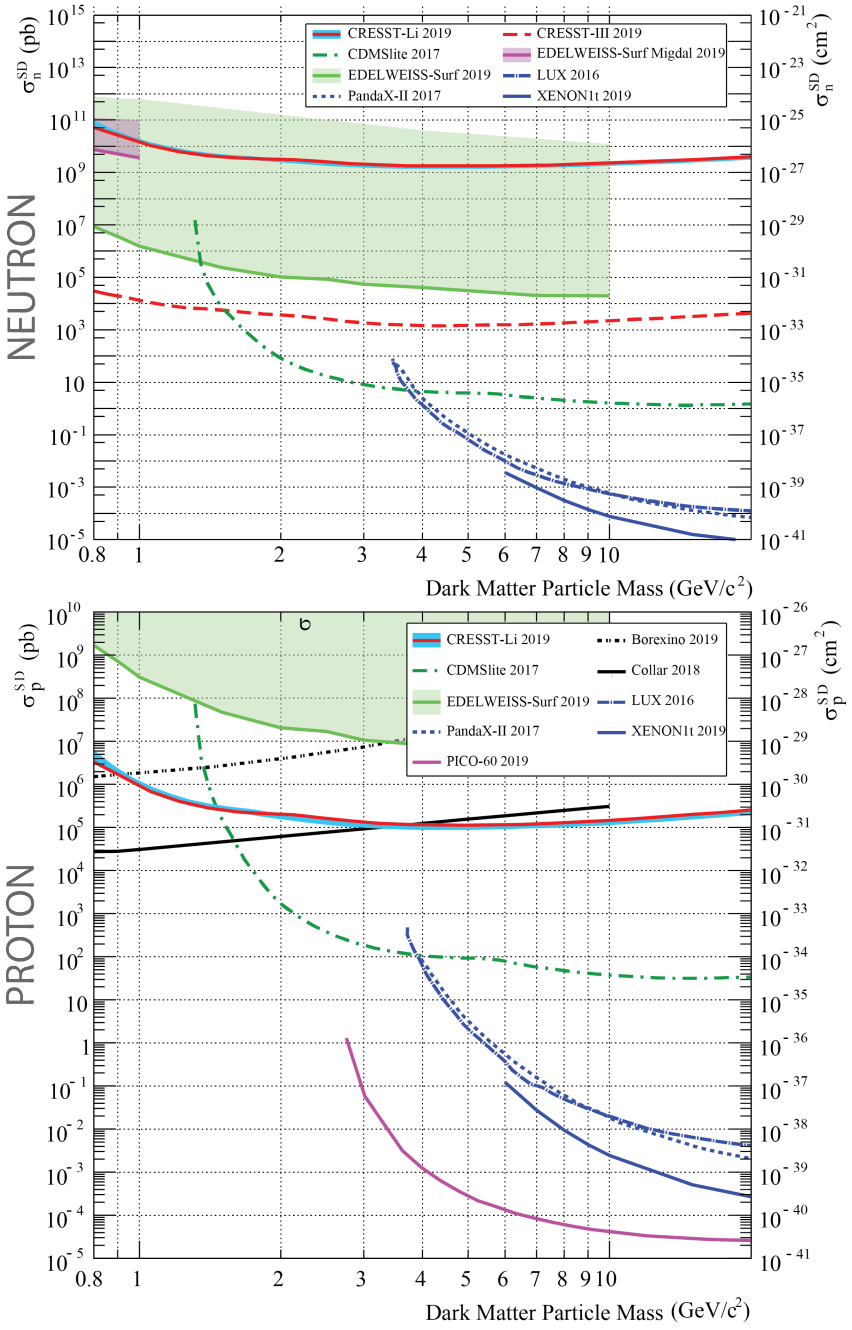

Figure 4.4: **Top:** Exclusion limit obtained for *neutron-only* spin-dependent interactions of dark matter particles with Standard Model particles. The cross section for this kind of interactions is shown on the y-axis (pb on the left, cm^2 on the right), while the dark matter particle mass is on the x-axis. The result of this work with ^{7}Li is drawn in solid red with the two-sigma band resulting from statistical uncertainty in solid blue: we reach $1.06{\cdot}10^{-26}$ cm^2 at 1 GeV/c^2. In dashed red we show the CRESST-III [122] limit using ^{17}O. For comparison, we show limits derived by other direct detection experiments: EDELWEISS [172] and CDMSlite [195] using ^{73}Ge; LUX [196], PandaX-II [199], and XENON1T [198] using ^{129}Xe+^{131}Xe (see legend). **Bottom:** Same, but for *proton-only* spin-dependent interactions. Our result with ^{7}Li is depicted in solid red with with the two-sigma band in solid blue, reaching $6.88{\cdot}10^{-31}$ cm^2 at 1 GeV/c^2. Additionally, we plot limits from other experiments: CDMSlite [195] and EDELWEISS [172] with ^{73}Ge; LUX [196], XENON1T [198], and PandaX-II [199] with ^{129}Xe+^{131}Xe; PICO-60 with ^{19}F [200]; Collar [193] with ^{1}H. Finally, we plot in dotted black a constraint from Borexino data derived in [214].

4.6 Conclusions

We have successfully operated a scintillating cryogenic detector based on 2.66 g of Li_2MoO_4 target crystal at the Max Planck Institute (MPI) for Physics in Munich, Germany. After testing the detector response in presence of a neutron source and a ^{57}Co γ rays source, we performed a background measurement lasting 9.68 hours of effective time, achieving an energy threshold of (0.932 ± 0.012) keV. This measurement sets the cornerstone for the use of lithium-based crystals in the low-mass spin-dependent dark matter sector and shows that it is possible to obtain extremely competitive results for masses below $1.5\,GeV/c^2$ even using a non-optimal phonon detector in a high background experimental setup.
We plan future measurements with lithium-based crystals, a CRESST-like phonon detector, and an underground experimental setup which could drastically boost the sensitivity with respect to this work.

Chapter 5

Cryogenic characterization of $LiAlO_2$ and new physics results

The content of this chapter was published as a collaborative effort in The European Physical Journal C (see [215]).
Part of the results were initially presented in [216], which I personally wrote.
I wrote the entirety of this paper, with the exception of Section 5.3, and prepared Figures 5.1, 5.2, 5.4, 5.5, 5.7, 5.8, 5.9 .
With the help of my day-by-day supervisor Dr. Michele Mancuso, I designed and prepared all the detectors employed in this work. This includes the cleanroom fabrication of the TES, gluing and bonding all the thermal sensors employed, assembling the detector modules.
Me and Dr. Michele Mancuso installed the detector modules in the dilution refrigerator at the Max Planck Institute for Physics, operated the dilution refrigerator, installed the neutron source, and acquired the data.
Together, we also installed the detector modules in the dilution refrigerator at LNGS and operated the dilution refrigerator. I personally installed and removed the neutron source at LNGS and set the operating point of the detectors. Me and Dr. Lucia Canonica acquired the data at LNGS.
I triggered and analyzed the data presented in Sections 5.5 and 5.6.

5.1 Abstract

In this work, a first cryogenic characterization of a scintillating $LiAlO_2$ single crystal is presented. The results achieved show that this material holds great potential as a target for direct dark matter search experiments. Three different detector modules obtained from one crystal grown at the Leibniz-Institut für Kristallzüchtung (IKZ) have been tested to study different properties at cryogenic temperatures. Firstly, two 2.8 g twin crystals were used to build different detector modules which were operated in an above-ground laboratory at the Max Planck Institute for Physics (MPP) in Munich, Germany. The first detector module was used to study the scintillation properties of $LiAlO_2$ at cryogenic temperatures. The second achieved an energy threshold of (213.02±1.48) eV which allows setting a competitive limit on the spin-dependent dark matter particle-proton scattering cross section for dark matter particle masses between 350 MeV/c^2 and 1.50 GeV/c^2. Secondly, a detector module with a 373 g $LiAlO_2$ crystal as the main absorber was tested in an underground

facility at the Laboratori Nazionali del Gran Sasso (LNGS): from this measurement it was possible to determine the radiopurity of the crystal and study the feasibility of using this material as a neutron flux monitor for low-background experiments.

5.2 Introduction

In the past few decades, great effort has been devoted to the investigation of dark matter [58]. One path which could lead to the identification of this elusive particle(s) is that of direct detection experiments. The goal of most experiments in this class is to detect interactions of a dark matter particle with nuclei of a target material [160]. The CRESST (Cryogenic Rare Event Search with Superconducting Thermometers) experiment, like most other direct searches, has primarily focused on probing spin-independent dark matter-nucleus interactions [217]. CRESST [122] is currently operating $CaWO_4$ and Al_2O_3 crystals at cryogenic temperatures in the LNGS underground laboratory located below the Gran Sasso massif in Italy. One advantage of this experiment is that the technology is not necessarily tied to the target employed; it is relatively easy to change the target crystal and thereby take advantage of the properties of different target nuclei.
In 2019, the CRESST Collaboration published the first results obtained with a lithium-based crystal operated in an above-ground laboratory [179], showing great potential for dark matter searches using lithium-containing crystals. Lithium is an attractive material because it is the lightest element that can be tested with the CRESST technology, which consists of a scintillating crystal equipped with a tungsten based Transition Edge Sensor (TES) operated at cryogenic temperatures. Since CRESST is heavily oriented towards the search for dark matter particles with sub-GeV mass, the adoption of crystals containing light elements can boost this exploration due to the favorable kinematics. Furthermore, lithium is one of the best elements to investigate spin-dependent interactions, being mainly constituted of ^{7}Li (92.41 % natural abundance [192]), which has $J_N = 3/2$ and $\langle S_p \rangle = 0.497$ [201]. We do not investigate spin-dependent interactions with ^{6}Li because of the current lack of $\langle S_{p/n} \rangle$ values in the available literature.
Another appealing property of these crystals is the possibility to detect the ^{6}Li(n,α)^{3}H reaction:

$$^6\mathrm{Li} + \mathrm{n} \rightarrow \alpha + {}^3\mathrm{H} + 4.78\ \mathrm{MeV}. \tag{5.1}$$

In fact, one of the most challenging sources of background for a direct dark matter search experiment are neutrons which, like dark matter particles, induce nuclear recoils. Through the detection of the above reaction, which shows a distinctive signature in a scintillating bolometer [188, 206], it is viable to precisely measure the neutron flux inside the experimental setup and, with the support of Monte Carlo simulations, it might be possible to reconstruct the energy spectrum of the neutrons. There are many crystals containing lithium that can be employed, such as Li_2MoO_4 [188, 189], $Li_2Mg_2(MoO_4)_3$ [190], Li_2WO_4 [218], and LiF [184, 191]. Amongst these, a crystal with promising properties is $LiAlO_2$. First, the CRESST technology for the direct deposition of a TES on the crystal surface can be applied. Second, $LiAlO_2$ is a scintillator at room temperature and shows a light emission with a 340 nm peak [219] at which the CRESST light detectors have a high absorption [167]. Finally, $LiAlO_2$ also contains ^{27}Al (100.0% natural abundance [192]), another interesting element

to study spin-dependent interactions, with $J_N = 5/2$ and $\langle S_p \rangle = 0.343$ [220]. The crystal used to build the detector modules operated in this work was produced at the Leibniz-Institut für Kristallzüchtung (IKZ) in Berlin and Section 5.3 is dedicated to a summary of the growth procedure. The following sections respectively detail the experimental setup, the data collected for the cryogenic characterization, the neutron and radiopurity measurements, and the dark matter results.

5.3 Crystal growth

All the detector modules used in this work are based on $LiAlO_2$ targets obtained from one single crystal grown at IKZ. The original crystal had a 5 cm diameter and was produced using the Czochralski technique [221]. The primary challenge for the growth of this kind of material stems from its high melting temperature of 1780°C, which entails a strong Li_2O evaporation. Li_2O evaporates not only from the melt, but also from the growing crystal: in unfavorable thermal conditions, this evaporation is so strong that an Li-free shell of α-Al_2O_3, a few millimeters thick, can form around the $LiAlO_2$ crystal. To avoid crystal decomposition which would arise from this effect, the axial thermal gradient in the setup must be kept as steep as possible. However, a steep temperature gradient implies an increased superheating of the melt associated with an intensified Li_2O evaporation from the melt itself: this shifts the melt composition from the desired one towards an Al_2O_3-rich melt. Because of non-identical melt and crystal compositions, the crystallization with Al_2O_3-rich melt involves solute segregation. To a certain extent, this results in the degradation of the grown crystals, in the form of a non-uniform macro distribution of the constituting elements and/or micro-inhomogeneities like second-phase inclusions, mainly $LiAl_5O_8$, due to reduced interface stability. There is no perfect set of growth conditions and parameters which can avoid all the effects of Li_2O evaporation: a practical solution will necessitate a compromise among crystal perfection, crystal size, and cost of the process.
The crystal used in this work was grown inside a cylindrical iridium crucible of 100 mm diameter in an argon protective atmosphere. The raw materials used for the crystal production are Li_2CO_3 and Al_2O_3 compounds with a 4N/5N purity. Special attention was paid to the preparation of the raw material in order to prevent Li_2O losses before the crystal growth: these materials were weighed and mixed in a stoichiometric ratio and calcinated at temperatures between 700°C and 750°C in platinum crucibles. The temperature and duration for this preparation was deduced from thermo-gravimetric measurements of the starting materials [222].

During the crystal growth, the axial temperature gradient was increased stepwise by changing the thermal insulation, until the opaque Al_2O_3 shell disappeared entirely and a shiny transparent crystal was obtained. This was achieved by applying a pulling rate of 1.5 mm/h when growing along the (100) direction, together with a crystal rotation between 10 and 25 rpm to improve the melt mixing. A more detailed description of the growth procedure, crystal defects, and tuning of the parameters can be found in [223].

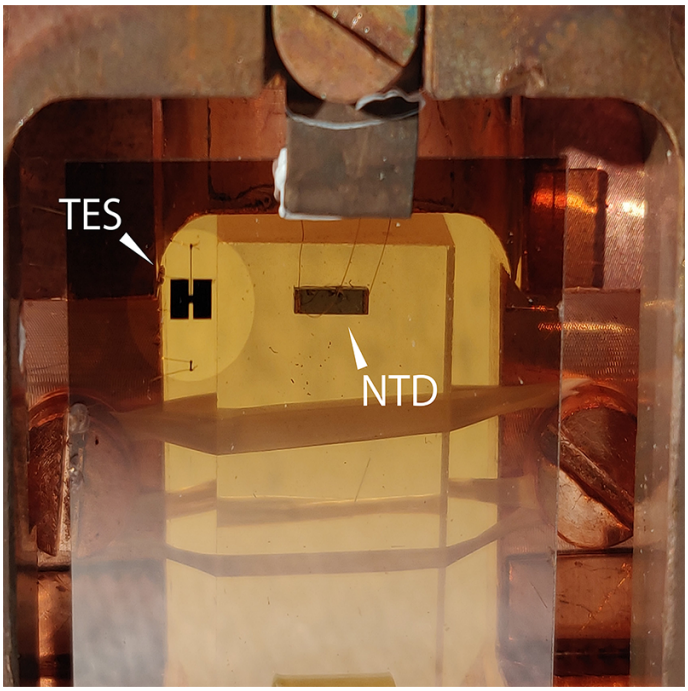

Figure 5.1: Close-up of *module A*. It is possible to see the 2.8 g $LiAlO_2$ crystal instrumented with the NTD sensor through the CRESST-III light detector.

5.4 Experimental setup at Max Planck Institute

Two (20x10x5) mm^3 crystals with a mass of 2.8 g each were cut from the $LiAlO_2$ single crystal produced at IKZ, and were used to assemble two different detector modules.

The first crystal was used to assemble *module A*, a detector module (see Figure 5.1) designed to characterize $LiAlO_2$ at cryogenic temperatures. In this case, the crystal was instrumented with a Neutron Transmutation Doped (NTD) germanium thermistor [157] glued [1] to one surface. The crystal was held in position inside a copper frame by two strings of PTFE tape. Electrical and thermal connections to the NTD were provided via 25 µm diameter gold bond wires. The temperature variation of the NTD was obtained by measuring the resistance of the thermistor. To do so, a constant bias current was sent through the NTD and the voltage drop of the sensor was measured with a commercial differential voltage amplifier [2]. A CRESST-III light detector (LD) [167] was facing the crystal, held in position by two CuNi clamps; this LD was made of a sapphire plate with a 1 µm silicon layer epitaxially grown on one face (Silicon-on-Sapphire) with a TES as thermal sensor deposited on the silicon side. The readout of the light detector is obtained with a commercial SQUID system [3], combined with a CRESST-like detector control system [166]. An ^{55}Fe X-ray source with an activity of $\sim$0.05 Bq was placed at a distance of $\sim$0.5 cm from the light detector to calibrate its energy response. The TES on the LD had a critical temperature $T_C{}^{LD}$=22 mK.
The second crystal constituted the main absorber of *module B* (Figure 5.2), a de-

[1] GP 12 Allzweck-Epoxidkleber, Gößl + Pfaff
[2] Stanford Research System - SR560 Low-noise voltage preamplifier
[3] Applied Physics System model 581 DC SQUID

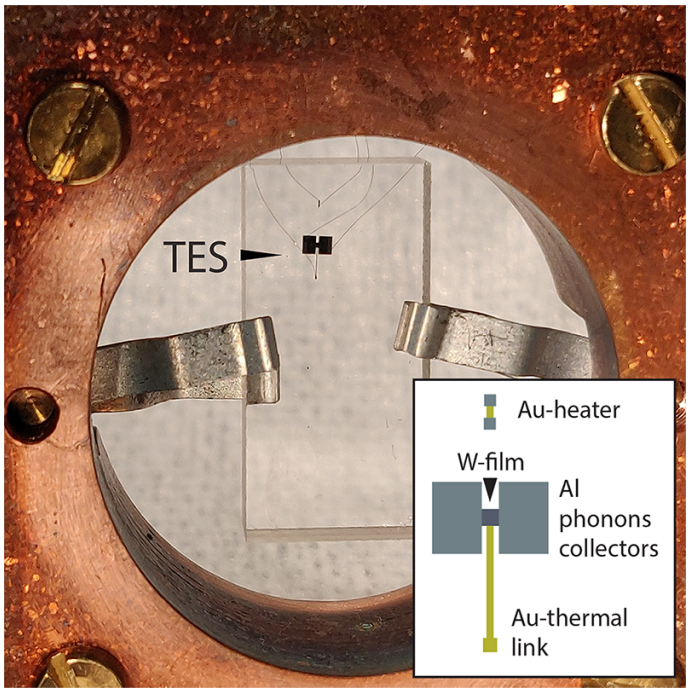

Figure 5.2: Close-up of *module B*, constituted by a 2.8 g $LiAlO_2$ crystal instrumented with a TES directly deposited on the surface. On the bottom right corner a scheme of the TES is shown (see text for details).

tector designed to reach a low energy threshold (<1 keV). The crystal was held in position inside a copper frame by two CuNi clamps. On one face of the crystal, a TES with a design similar to that of the light detector was deposited. The TES is constituted by a thin strip of tungsten with two large aluminum pads partially overlapping the tungsten layer. The aluminum pads serve two different purposes, as phonon collectors and as bond pads. The bond pads are connected via a pair of 25 µm aluminum bond wires through which the bias current is injected. The tungsten film is also connected by a long and thin strip of gold to a thicker gold bond pad on which a 25 μm gold wire is bonded. The gold strip serves as a weak thermal link between the sensor and the heat bath at ∼10 mK. On the same surface, but separated from the TES, there is an evaporated heater made of a thin strip of gold with two aluminum pads deposited on top. These pads are bonded with a pair of 25 μm aluminum bond wires through which a tunable current is injected to maintain the TES at the desired temperature. The heater is also used to inject heater pulses to monitor the detector response over time and for calibration purposes.
This TES had a critical temperature ${T_C}^B \simeq 42.5$ mK (Figure 5.3) when operated with a 4 µA bias current. ${T_C}^B$ is rather high compared to usual transition temperatures of CRESST TESs (∼15 mK); this can negatively affect the performance of the calorimeter, resulting in a higher energy threshold.

The two modules have been operated together inside a Leiden Cryogenics dilution refrigerator at the Max Planck Institute for Physics in Munich, Germany. The dilution refrigerator is located in an above-ground laboratory without shielding against environmental and cosmic radiation. The modules have been mechanically and thermally connected to the coldest point of the dilution refrigerator (∼10 mK).

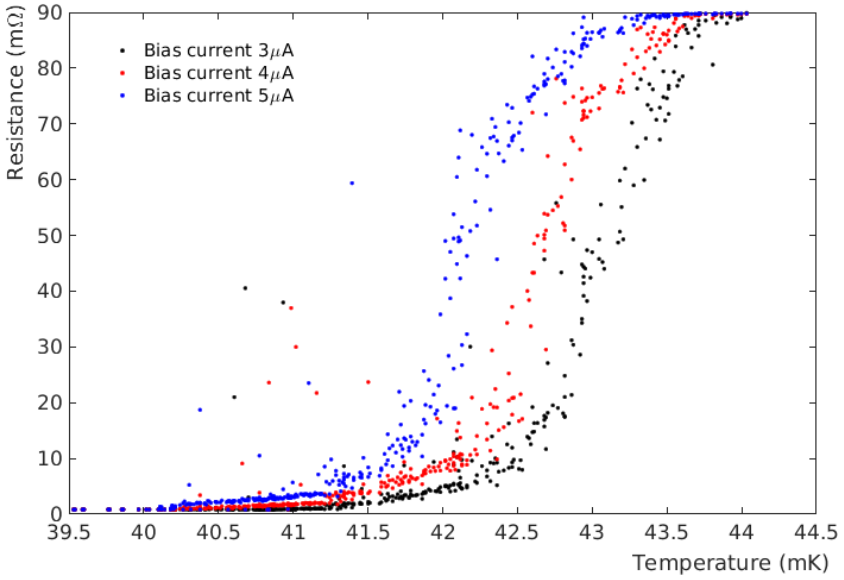

Figure 5.3: Measurement of resistance versus temperature with 3 different bias currents applied to the TES on *module B*. At ∼42.5 mK there is a transition between a superconducting response and a normal conducting response (Critical Temperature T_C) measured with a 4 μA bias current. The T_C has a slight dependence on the bias current applied to the TES caused by the electrothermal feedback.

5.5 First cryogenic characterization of $LiAlO_2$

Since there is no literature available on the cryogenic performance of $LiAlO_2$, the starting point was to study its basic properties. This was done using *module A*, which allowed an initial overview on scintillation, light yield (LY), and Quenching Factors (QFs) [4] [209, 224, 225] for different particle interactions inside the crystal.
The energy calibration of the light detector was performed using the peaks originating from the ^{55}Fe source (Figure 5.4). After calibration, the baseline resolution of the light detector is $\sigma^{LD}_{baseline} = (26.64 \pm 1.20)$ eV, while the resolution at 5.895 keV is σ_{Fe}=(123.9±4.1) eV.
During the operation of *module A*, an AmBe neutron source was installed at a distance of ∼50 cm from the center of the dilution refrigerator. For the energy calibration of the NTD the neutron capture peak appearing at 4780 keV (Equation 5.1) was used, where the energy resolution is
$\sigma_{capture}$=(19.96±0.72) keV.
In Figure 5.5, the energy measured in the light channel is plotted versus the energy measured in the phonon channel for each event registered by the detector during 9.44 hours of effective measuring time in the presence of the AmBe neutron source. Three main different families of events are easily distinguishable. Gamma and beta particles interacting in the $LiAlO_2$ form one band starting from zero energy and

[4] The Quenching Factor for the interaction of an arbitrary particle x is defined as: $QF_x = LY_x/LY_\gamma$

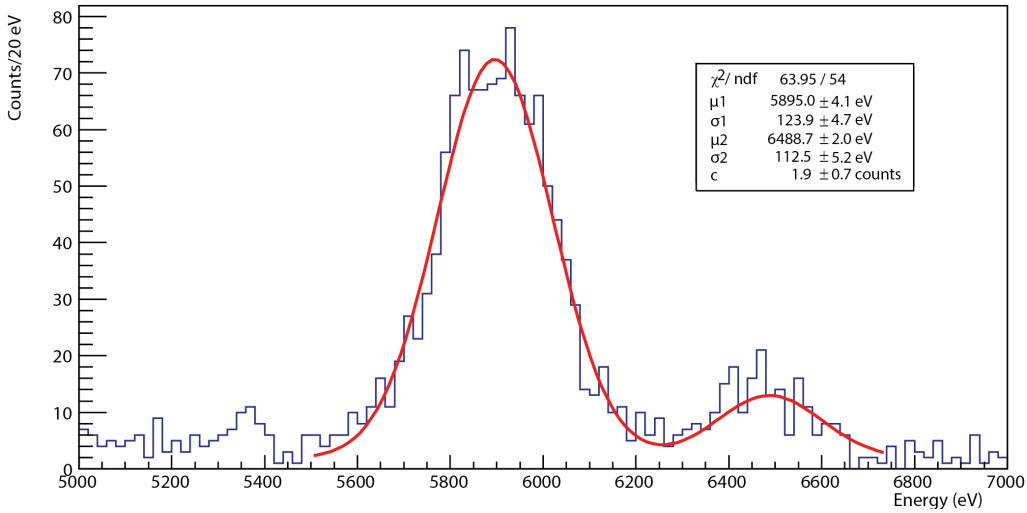

Figure 5.4: Energy spectrum of events registered by the CRESST-III light detector in the energy region of X-ray emission by the ^{55}Fe source. Two peaks are visible: one at 5.895 keV, resulting from the sum of $K_{\alpha 1}$ and $K_{\alpha 2}$ lines, and one at 6.490 keV, resulting from the sum of $K_{\beta 2}$ and $K_{\beta 3}$ lines. The fit function (red solid line) consists of the sum of two Gaussian functions (μ_1 and μ_2 are the expected values, σ_1 and σ_2 the standard deviations) plus a constant factor c to account for the flat background. In principle, σ_2 should not be lower than σ_1, but we attribute this anomaly to the presence of an energy loss in the left shoulder of the 5.895 keV peak. The 5.895 keV peak is used to obtain the energy calibration of the light detector.

with a light yield of (1.180±0.103) keV/MeV, where the LY is defined as:

$$\mathrm{LY} = \frac{\mathrm{Energy_{LD}}}{\mathrm{Energy_{NTD}}} \tag{5.2}$$

Neutrons scattering within the crystal exhibit a band starting from zero energy as well, but with a much reduced light yield (0.284±0.056) keV/MeV, resulting in a Quenching Factor for neutrons equal to 0.241. At high energies and with a light yield of ∼0.75 keV/MeV (or (3.438±0.227) keV at 4.78 MeV), in between the β/γ band and the neutron band, the neutron capture by ^{6}Li appears. Assuming a linear light emission up to this energy, the QF for the neutron capture is 0.599.
The separation between the β/γ band and the neutron band starts to become evident at ∼170 keV; thus, in the energy region of interest for dark matter search (∼0-10 keV) it will be unlikely to achieve an effective particle discrimination based on the light yield, even with a substantial improvement of the light collection in comparison to this measurement. In the vicinity of the neutron capture a small family of events appears, with a slightly higher energy. There is currently no clear interpretation and further investigations will be carried out to understand its origin, which might be tied to a resonance in the cross section for the ^{6}Li(n,α)^{3}H reaction. This family of events has not been observed in the LNGS measurement (see Section 5.8), but the neutron source employed in that case had an extremely reduced activity with respect to the above-ground measurement.

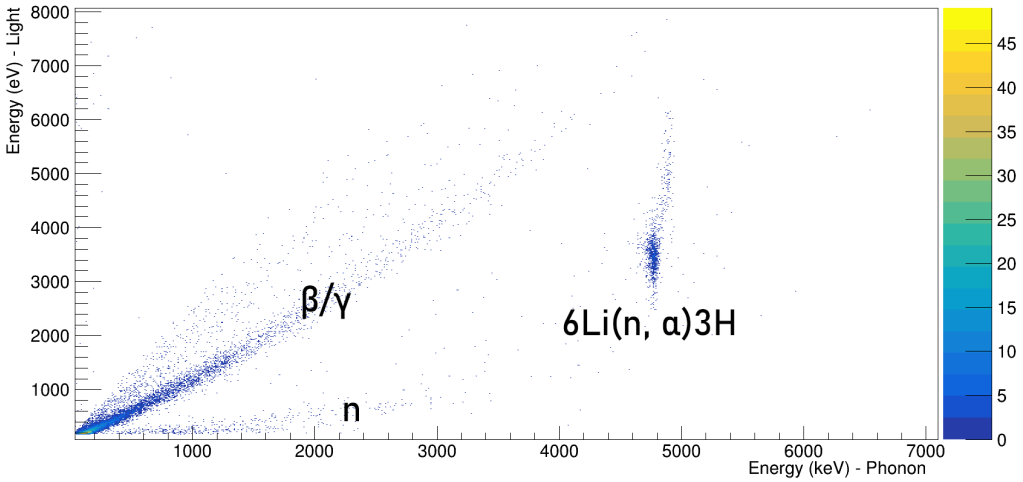

Figure 5.5: Energy measured by the CRESST-III light detector versus energy measured by the NTD for each event registered by *module A* in the presence of an AmBe neutron source during 9.44 hours of data collection. Two bands starting from zero appear: the one with the higher light emission is constituted by β/γ events interacting inside the $LiAlO_2$ crystal, while the one with lower light emission is caused by the scattering of neutrons within the crystal. At 4780 keV a different family of events appears, due to the neutron capture of ^{6}Li. In the vicinity of the neutron capture there is an additional family of events, with a slightly higher energy. This family currently is of unknown origin and the modeling of the anomalously high light yield is particularly challenging.

5.6 Dark matter results

As explained in Section 5.5, *module B* was designed to study spin-dependent interactions of low-mass dark matter particles with nuclei of a $LiAlO_2$ crystal in a cryogenic measurement. A low threshold is a key parameter to reach this goal, due to the steep increase of expected dark matter recoils at lower energies. For this reason the TES was directly evaporated onto the $LiAlO_2$ surface, applying, for the first time, the CRESST technology on a crystal containing lithium .
A total of 22.2 hours of data without any source ("background data") were collected for *module B* using a continuous DAQ with a sampling rate of 25 kHz. The events were triggered with a dedicated software based on the optimum filter [226].

The energy calibration is implemented using the 5.895 keV peak from the ^{55}Fe source, similar to the one used for the LD of *module A*. During the run, heater pulses of four different known amplitudes were injected to interpolate the energy calibration in the whole energy region of interest. The peaks corresponding to the heater pulses are identified in the dataset: each peak is fit with a Gaussian function which returns the mean and the error of the mean. Afterwards, the amplitude of heater pulses ($A_{injected}$) versus the amplitude measured by the TES (A_{phonon}) is plotted and the following function is fit to the data points:

$$A_{phonon} = p0 \cdot \frac{p1 \cdot A_{injected} \cdot I}{R_L + p1 \cdot A_{injected}} \tag{5.3}$$

where p0 is the gain of the SQUID, I is the bias current of the TES, R_L is the load resistor, and p1 is a coefficient which translates the temperature change of the TES,

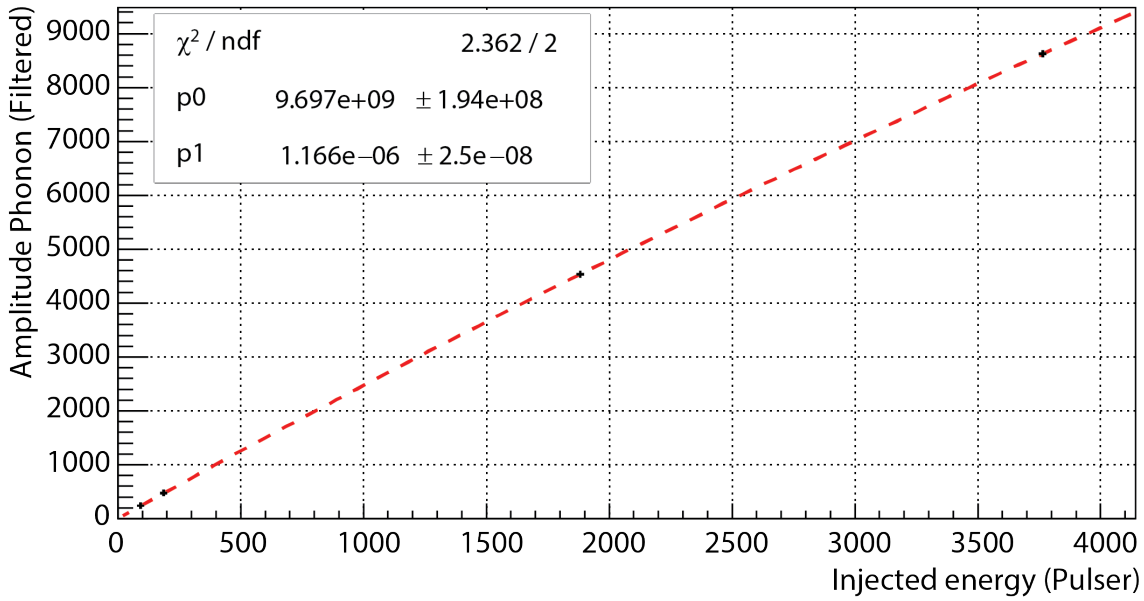

Figure 5.6: Injected amplitude of 4 different heater pulses versus amplitude registered by the TES (black crosses) expressed in arbitrary units. Each amplitude registered by the TES with relative error are obtained from the peaks appearing in the raw spectrum via a Gaussian fit. The four points are fit with Equation 5.3, which is used for the energy calibration of the detector.

induced by the heat pulse, into a variation of the TES resistance. Equation 5.3 is derived from the circuit scheme used to read out the TES [166]. For this measurement I=9 μA, while R_L=40 mΩ; p0 and p1 are the free parameters of the fit. Finally, the mean value registered by the TES A_{phonon}=(2379.2±0.7) a.u. corresponding to the 5.895 keV X-ray is used to convert A_{phonon} to energy via Equation 5.3. This description assumes that the TES resistivity changes linearly with the temperature in the energy interval considered (0-6 keV). With this method an accurate energy calibration (Figure 5.6) was obtained taking into account the intrinsic non-linearity of the read-out scheme. The baseline resolution is $\sigma^B_{baseline}$=(39.75±1.23) eV. The corresponding energy threshold for particle interactions with the target is E^B_T=(213.02±1.48) eV, calculated by using the same method as presented in [227]. In this case, however, the total rate of counts in the noise above threshold (noise trigger rate) is set to 10^3 counts/(keV·kg·day), two orders of magnitude lower than the observed event rate in the 1-5 keV range.

Figure 5.7 shows the calibrated energy spectrum of the 22.2 hours background measurement. The X-ray peaks from ^{55}Fe decay clearly emerge. A moderate rise of events below 300 eV is also evident. The energy resolution at 5.895 keV, calculated in the same way as for the LD of *Module A*, is σ_{K_α}=(184.0±1.6) eV, significantly worse than the resolution for heat pulse events which is equal to σ_{HP_2}=(41.6±1.0) eV at 1.159 keV and σ_{HP_3}=(57.0±1.6 eV) at 11.537 keV. This degradation in energy resolution for particle events is being investigated further. In the flat part of the spectrum, below the X-ray peaks, the background rate is of the order of $2{\cdot}10^5$ counts/(keV·kg·day), similar to the one observed in [205]. This high value is expected, since the detector is operated in an above-ground laboratory without any shielding or veto systems.

From the measured spectrum, dark matter exclusion limits for spin-dependent in-

teractions are calculated. The energy region of interest ranges from E_T^B to 4000 eV without applying any cut to the particle events registered by the detector. All the events with energies above 4000 eV contribute to the dead time, reducing the exposure from 22.2 hours to 17.2 hours, corresponding to a total exposure of $2.01{\cdot}10^{-3}$ kg·day, with an exposure for ^{7}Li of $1.95{\cdot}10^{-4}$ kg·day and an exposure for ^{27}Al of $8.22{\cdot}10^{-4}$ kg·day. The exclusion limits are calculated using Yellin's optimal interval method [211, 212] and are shown in Figure 5.8. The baseline resolution of the detector $\sigma^B_{baseline}$ and the energy threshold E_T^B are taken into account to evaluate the minimum value of dark matter mass for which it is possible to draw exclusion limits. These limits are valid for both *proton-only* interactions and for *neutron-only* interactions, as discussed in the theoretical framework presented in [179]. The calculation of the exclusion limits adopts the standard dark matter halo model, which assumes a Maxwellian velocity distribution and a local dark matter density of $\rho_{\mathrm{DM}} = 0.3\,(\mathrm{GeV/c^2})/\mathrm{cm^3}$ [91]. Furthermore, $v_{\mathrm{esc}} = 544\,\mathrm{km/s}$ is assumed for the galactic escape velocity [89] and $v_\odot = 220\,\mathrm{km/s}$ for the solar orbit velocity [213]. For the *proton-only* exclusion limits $\langle S_p\rangle = 0.4970$ for ^{7}Li and $\langle S_p\rangle = 0.3430$ for ^{27}Al are used, while for the *neutron-only* exclusion limits $\langle S_n\rangle = 0.0040$ for ^{7}Li and $\langle S_n\rangle = 0.0296$ for ^{27}Al [201, 220] are used. The data analysis efficiency is computed generating a known flat energy spectrum of events. These events are created by superimposing the ideal detector response on recorded data and then processed with the same analysis chain used for the real data. The fraction of surviving events over the total simulated events at each energy bin represents the data analysis efficiency. Since the determination of the amplitude and the triggering are done in one step by the optimum filter and no further data selection criteria applied, in this case the data analysis efficiency is equivalent to the trigger efficiency.

5.7 Experimental setup at LNGS

After the successful tests at MPP, the bulk of the original $LiAlO_2$ crystal sample was mechanically polished obtaining a 373 g crystal. Such crystal size is ideal to study the crystal radiopurity and to assess the feasibility of using $LiAlO_2$ crystal as a monitor for the neutron flux in a shielded experimental setup. For this reason, this crystal was used in a new detector module, *module C*, which was installed in the MPP Test-Cryostat facility located in the underground laboratory of Laboratori Nazionali del Gran Sasso (LNGS), under 3600 m water equivalent overburden to shield against cosmic radiation [229].
As visible in Figure 5.9, an NTD [157], a (5×5×1) mm^3 Si carrier with a thin gold stripe heater deposited on it, and a $CaWO_4$ carrier crystal on which a CRESST-II TES had been evaporated [170] are both glued [5] to the top surface of the $LiAlO_2$ crystal. The NTD and the CRESST-II TES are both being used as phonon sensors. This choice is motivated by the fact that the NTD has a higher dynamic range than the TES, while the TES can generally achieve a lower energy threshold than the NTD. Therefore, with this detector module it is possible to study both the low energy part of the spectrum (∼1 keV) and the high energy part (∼10 MeV). This allows the potential setting of competitive limits for spin-dependent dark matter search and the detailed study of the neutron capture by ^{6}Li during the same measurement.

[5] GP 12 Allzweck-Epoxidkleber

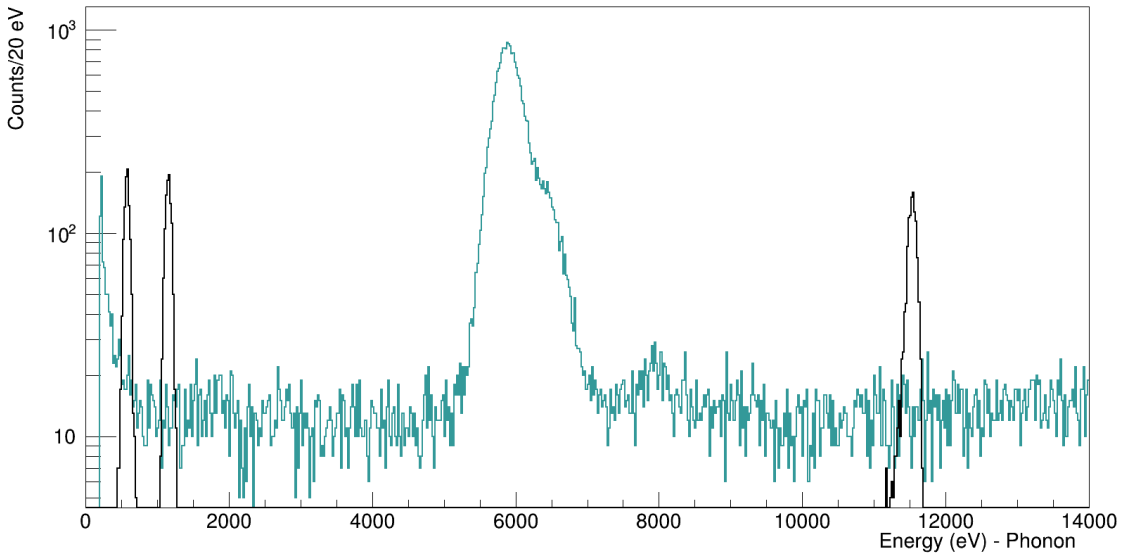

Figure 5.7: Energy spectrum collected during 22.2 hours of background measurement with *module B* without any cut applied to the data set. In black: events induced by injected heater pulses. In light blue: particle events only. At 5.895 keV the peak caused by the X-ray emission of ^{55}Fe decay appears; the energy resolution at 5.895 keV is equal to σ_{K_α}=(184.0±1.6) eV. The resolution for heat pulse events is equal to σ_{HP_2}=(41.6±1.0) eV at 1.159 keV and σ_{HP_3}=(57.0±1.6 eV) at 11.537 keV. Below 300 eV there is a rise in the spectrum.

The crystal was held in position inside a copper holder using three PTFE clamps on the bottom and three on the top. Reflective foil [6] was used to surround the crystal, in order to maximize light collection. A CRESST-II light detector [230] was facing the top surface of the $LiAlO_2$ crystal, completing the detector module.
The MPP Test-Cryostat facility is located in the corridor connecting Hall A and Hall B of LNGS. The model of dilution refrigerator installed in this facility is the same as the one used for the above-ground measurement at MPP. The detector module operated in this dilution refrigerator employs the same kind of wiring, NTD readout, and TES readout as in the previous above-ground measurement.

5.8 Neutron and radiopurity measurements at LNGS

The detector operation of *module C* at LNGS was divided into two parts: one focused on the efficacy of measuring neutrons, the other on measuring the radioactive impurities in the crystal. For these type of measurements, the data collected with the NTD (that does not saturate in the energy region of interest) and the CRESST-II light detector have been analyzed. The CRESST-II TES was also simultaneously operated as a phonon sensor to study the low-energy part of the spectrum (<1 MeV). At the beginning of the run an AmBe neutron source emitting ∼10 neutrons/s was installed at a distance of ∼60 cm from the center of the dilution refrigerator and 13.1 hours of data were collected. To ensure the stability of the NTD sensor, heater pulses with seven different amplitudes were injected, two of which were close to

[6] 3M's Vikuiti^{TM} Enhanced Specular Reflector

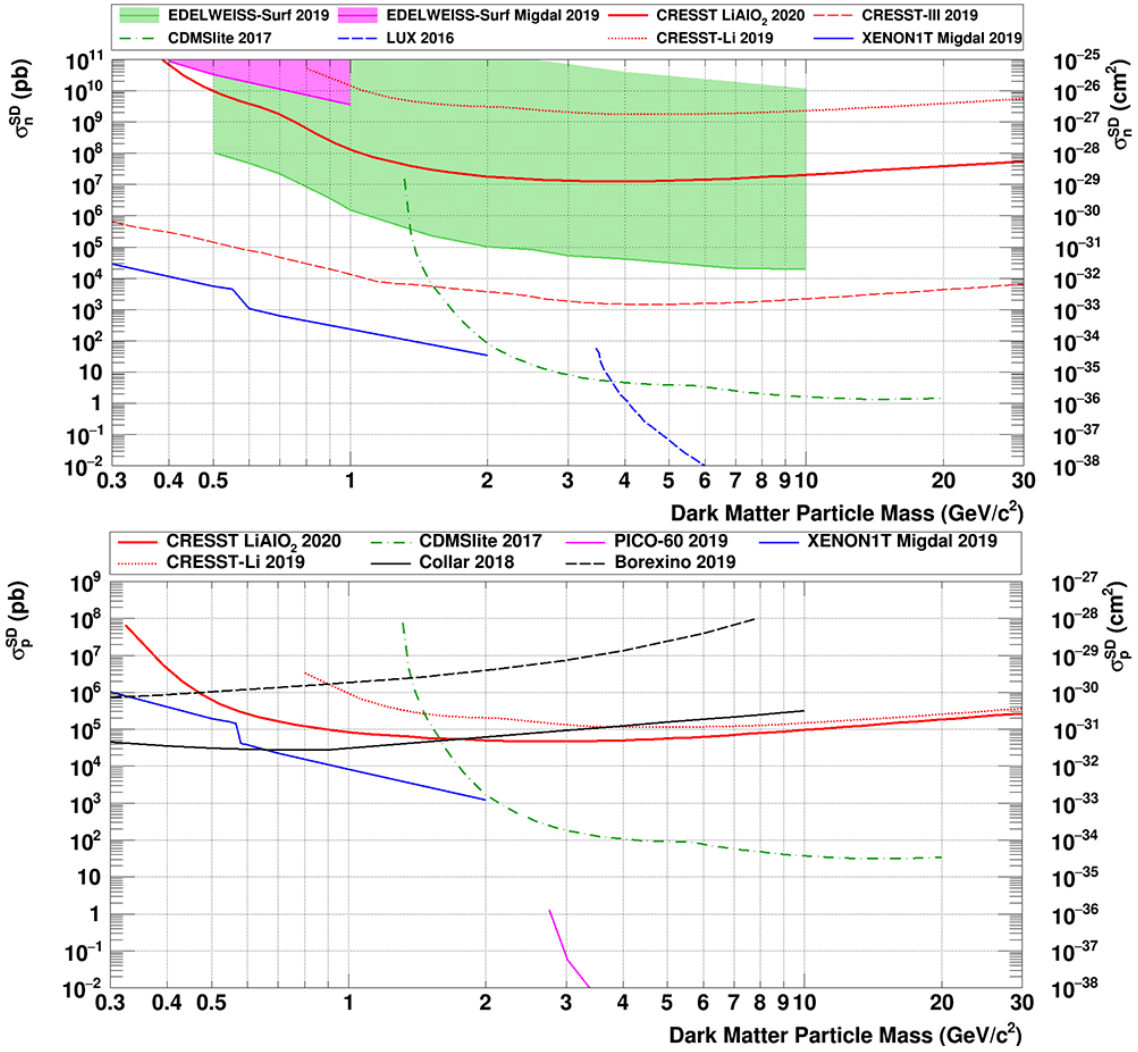

Figure 5.8: **Top:** Exclusion limits set by various direct detection experiments for spin-dependent interactions of dark matter particles with neutrons. The result obtained from *module B* data with ^{7}Li+^{27}Al is shown in solid red. The first result obtained by CRESST using ^{7}Li is plotted in dotted red [179], while the result obtained with ^{17}O in CRESST-III is shown in dashed red [122]. For comparison, limits from other experiments are also shown: EDELWEISS [172] and CDMSlite [195] using ^{73}Ge, LUX [196] and XENON1T (Migdal effect) [228] using ^{129}Xe+^{131}Xe. **Bottom:** The same, but for spin-dependent interactions of dark matter particles with protons. The result obtained from *module B* data with ^{7}Li+^{27}Al is shown in solid red. The first result obtained by CRESST using ^{7}Li is plotted in dotted red [179]. Additionally, limits from other experiments are also shown: CDMSlite with ^{73}Ge [195]; PICO with ^{19}F [116]; XENON1T (Migdal effect) with ^{129}Xe+^{131}Xe [228]; Collar with ^{1}H [193]. Finally, a constraint from Borexino data derived in [214] is shown in dotted black.

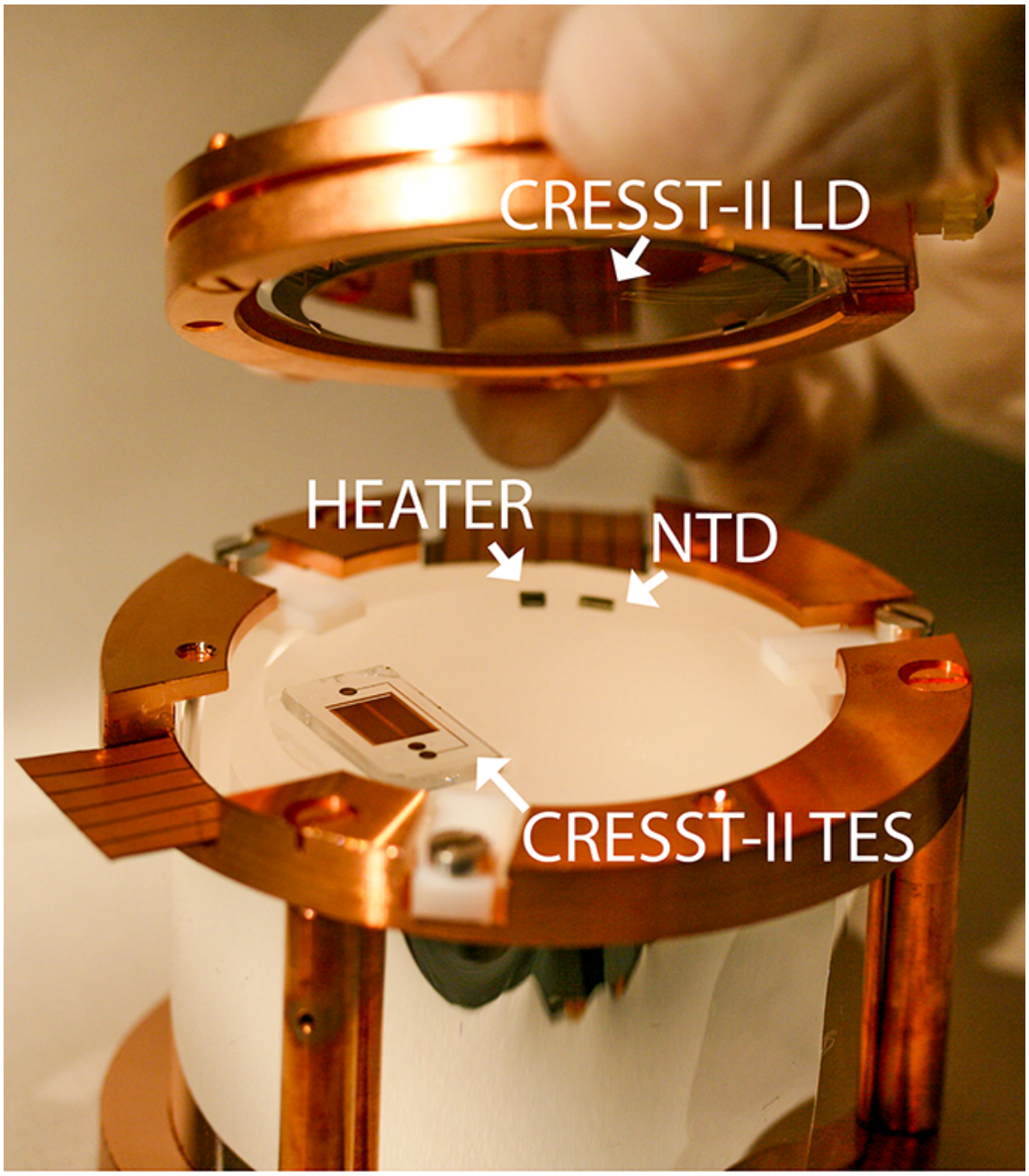

Figure 5.9: Detector *module C* was operated at LNGS. A 373 g crystal is instrumented with two phonon sensors glued on the top surface: an NTD and a CRESST-II TES. On the same surface there is a glued heater which ensures the stability of the detector operation. The crystal is surrounded by reflective foil and a CRESST-II light detector is facing the top surface of $LiAlO_2$.

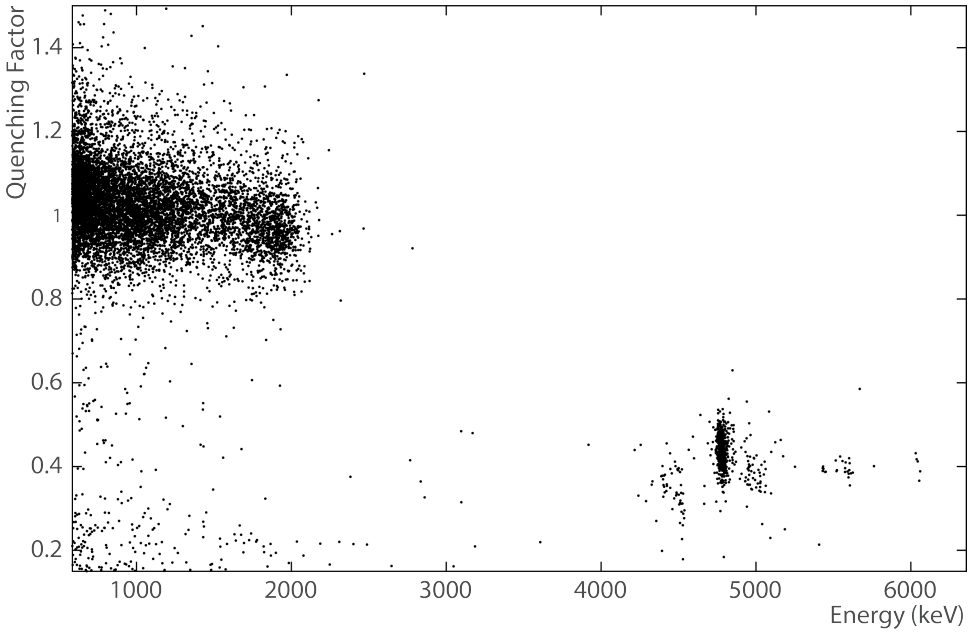

Figure 5.10: QF versus the energy registered by the NTD sensor for 13.1 hours of effective live time in the presence of a weak AmBe source. For energies $\lesssim$2.6 MeV it is possible to see the β/γ band which was used to normalize the QF. At energies $\gtrsim$3 MeV and for lower QF values, multiple families originated by α decays and one prominent line at 4.78 MeV corresponding to the neutron capture of ^{6}Li can be seen.

the energy region of interest for the neutron capture by ^{6}Li (Equation 5.1). The detector response was calibrated using these heater pulses and the 4.78 MeV peak corresponding to the neutron capture. After calibration, the energy resolution at 4780 keV is
$\sigma_{capture}$=(18.3±1.02) keV. In Figure 5.10, the scatter plot of QF versus the energy registered by the NTD for all the events recorded during the neutron measurement is presented. In this plot, the neutron capture peak shows a higher QF than the events originating from α decays. These two classes of events are used to build two histograms (Figure 5.11): neutron capture events are selected from an energy interval of $\pm 3\sigma_{capture}$ centered around 4780 keV, while all other events above 4 MeV are considered alpha events. It is possible to see that the two distributions are partially overlapping. However, even with a simple cut on the QF value one can exclude the vast majority of unwanted α decay events: if only events with a QF>0.44 (the mean value of the neutron capture distribution) are accepted, 93.3% of α events are cut while halving the detection efficiency for the neutron capture. The efficiency in discarding α events can then also be considerably increased defining a cut on the energy detected by the NTD phonon sensor: clearly, this cut is more effective the higher the energy resolution of the NTD.
In a low-background environment only a few neutron events are expected, while the number of alpha events depends on the radiopurity of the detector. This means that there would probably be not enough events to build two distributions based on the QF values. However, it is possible to perform a neutron calibration and then, based on the data, define a region where neutron events are expected during the background data campaign. From the total number of events inside this region, it is then feasible to quote a neutron flux value (or upper limit) with the respective

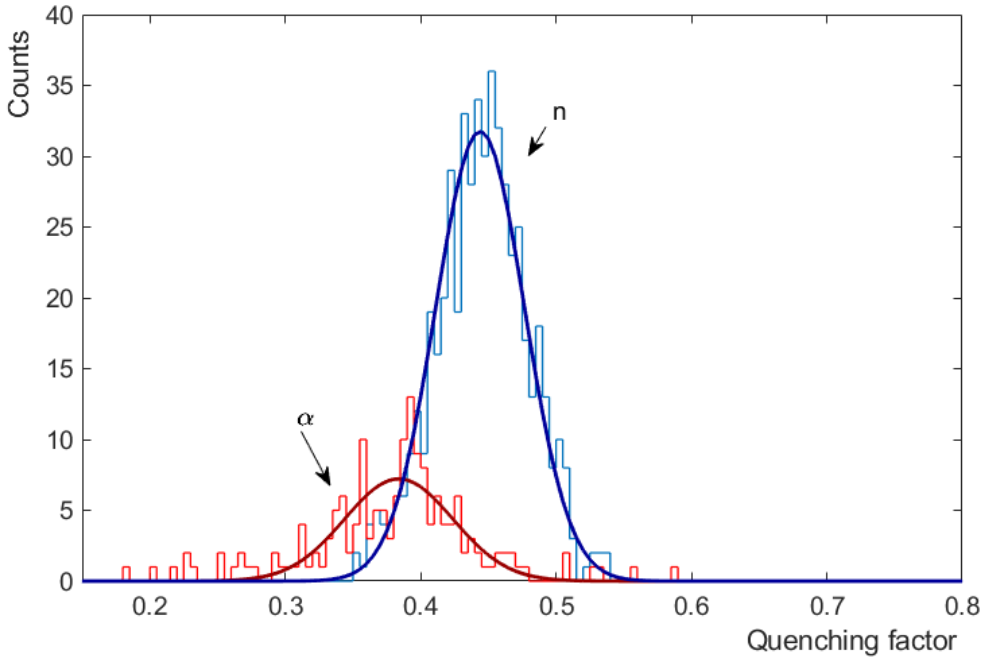

Figure 5.11: Distribution of QF values for events originated by α decays with a mean value of 0.38±0.04 (red) and distribution of QF for neutron capture events with a mean value of 0.44±0.03 (blue).

uncertainty.

The long term goal for CRESST is to directly detect neutrons inside the experimental setup using a specifically designed detector based on a lithium-containing crystal, thereby providing a relevant input to the background model of the experiment. From these data, using dedicated Monte Carlo simulations, the total neutron flux (or an upper limit) can be assessed while also possibly reconstructing the energy spectrum of the incoming neutrons. The measurement presented in this work is a first step in this direction.

After the neutron measurement, the AmBe source was removed to measure the radiopurity of the crystal. In this case, a 58.4 hours background measurement was carried out. After stability and data quality cuts, the effective measuring time is 35.6 hours. In this measurement it was not possible to use the neutron capture peak to calibrate the NTD response, but the heater pulses that were previously calibrated were used instead. In Figure 5.12, the energy spectrum measured by the NTD is shown without cuts. From this spectrum, at least 6 different peaks due to α decays in the 4-7 MeV region can be distinguished. After a careful evaluation, it can be assumed that three radioactive parents are inducing the peaks highlighted: ^{210}Po, ^{226}Ra, and natural uranium. The respective calculated activities are listed in Table 5.1. In principle, ^{226}Ra should be part of the ^{238}U decay chain, but it is not possible to correctly match the respective activities. One straightforward explanation is that ^{226}Ra and ^{238}U are not in secular equilibrium; as such the two contaminants are treated as separate parents of their respective decay chain. In fact, in the case of the secular equilibrium the peak centered around 4.86 MeV is expected to be ∼3 times more populated than the ^{238}U peak, due to the summing of ^{226}Ra, ^{230}Th, and ^{234}U activities. However, this peak is only 1.43 times more

Isotope	Activity (mBq/kg)
^{210}Po	0.314±0.080
^{226}Ra + ^{234}U	3.327±0.257
^{235}U	0.231±0.069
^{238}U	2.260±0.217

Table 5.1: Activities of the radioactive parents as observed during the background measurement at LNGS.

populated than the ^{238}U peak and equal, well within 1 sigma, to the sum of ^{222}Rn (0.962±0.142 mBq) and ^{238}U activities. One explanation which can fit well the data is that ^{226}Ra and its daughters are in secular equilibrium and have the same activities, while we do not observe the daughters of ^{238}U and ^{235}U decay chains. The activities ratio of the uranium isotopes are roughly as expected for the presence of natural uranium, only the activity of ^{235}U is slightly higher than expected, but within 2 sigma. It has to be noted that the ^{235}U peak is the least populated and so the most affected by statistical uncertainties. The uranium peaks appear to be broader than the peaks caused by the ^{226}Ra daughters. This could signal that the uranium might be present both internally and on the surfaces of the crystal, while ^{226}Ra might prevalently be an internal contamination. This observation, combined with the break of the secular equilibrium between ^{238}U and ^{226}Ra, could point at two contaminations at different stages of the crystal production and handling, one related to ^{226}Ra and one due to natural uranium.
In addition to the ^{214}Bi-^{214}Po decays, two peaks can be attributed to the daughters of ^{226}Ra: ^{218}Po and ^{222}Rn. Finally, a modest contamination of ^{210}Po is also observed.

The total number of events above 3 MeV is 483: this means an upper bound on the total alpha activity of (10.1±0.5) mBq/kg for this particular $LiAlO_2$ crystal. Considering this value, the radiopurity of this crystal is ∼3 times worse than the most radiopure $CaWO_4$ crystal produced within the
CRESST Collaboration (TUM40) [231], but in line with standard commercial $CaWO_4$ crystals. The goal for the future is to drastically improve the radiopurity of $LiAlO_2$, starting from a careful selection of the raw materials used for the crystal growth, and the material used for cutting and polishing. Additionally, a 20.8 hours calibration using a ^{241}Am gamma source installed close to the outer shield of the dilution refrigerator was carried out to test the performance of the CRESST-II TES[216]. During the calibration and the background measurement, heater pulses with nine different amplitudes were injected. The 59.54 keV gamma peak from the ^{241}Am source used for the energy calibration has a resolution of σ_{Am}=(3.044±0.074) keV. Similarly for the TES calibrations presented before, this peak and the peaks corresponding to the injected heater pulses are used to accurately calibrate the detector response at different energies. The sensor has an energy threshold of (2.601±0.126) keV, considerably higher than that achieved in the measurement performed above-ground with a smaller $LiAlO_2$ crystal: this is expected due to the large increase in mass as showed by the scaling law described in [232].

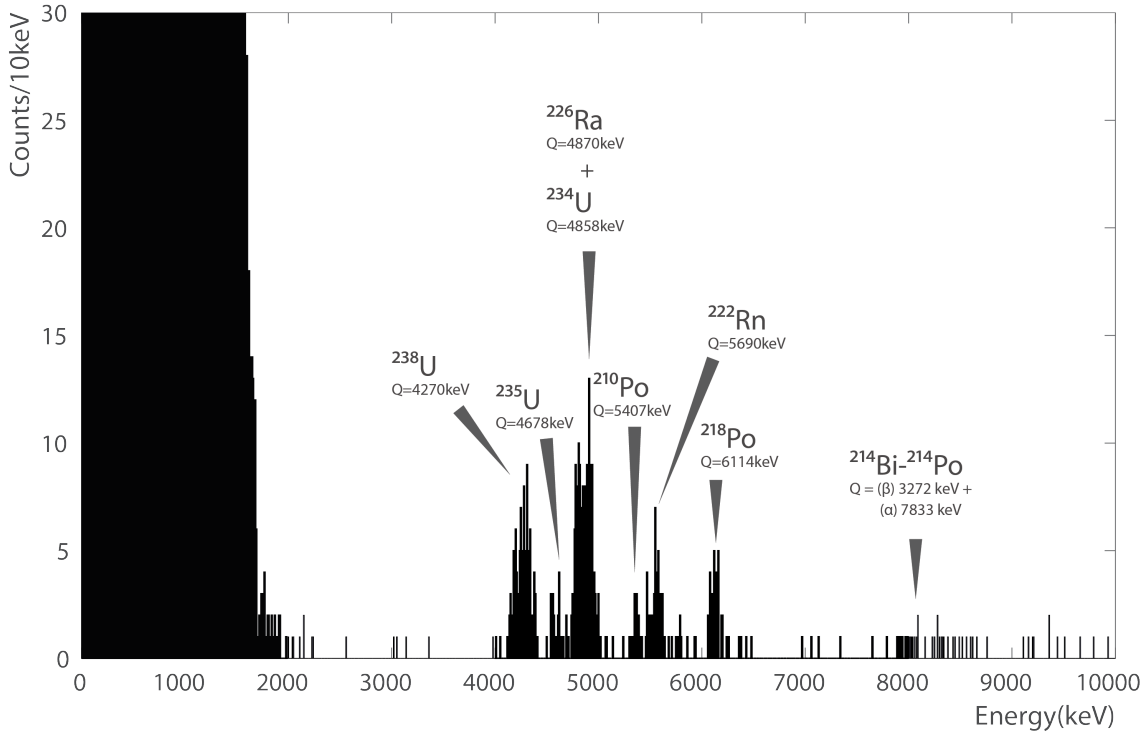

Figure 5.12: Energy spectrum registered by the NTD during a background measurement of 35.6 hours effective time. From this spectrum at least 7 different sources of α decays in the 4-7 MeV region can be distinguished and above 7 MeV additional events, likely due to ^{214}Bi-^{214}Po decays, appear.

5.9 Conclusions

This work details the results of three different detectors, all of which employ a $LiAlO_2$ target crystal, a material that has never been employed in cryogenic experiments thus far. The cryogenic properties of the material were tested in an above-ground laboratory with a 2.8 g crystal and new limits on spin-dependent dark matter interactions are set with a crystal instrumented with a TES deposited on $LiAlO_2$. A large-size detector with a mass of 373 g was operated in an underground cryogenic facility at LNGS in the presence of a weak neutron source, in order to assess the feasibility to monitor the neutron flux directly inside cryogenic setups. The results presented in this work demonstrate the high potential of $LiAlO_2$ crystals as cryogenic detectors in the field of low-background applications and contribute to the ongoing search for dark matter.

Chapter 6

Testing the bolometric properties of $Tm_3Al_5O_{12}$

The content of this chapter was published as a collaborative effort in Nuclear Instruments and Methods in Physics Research Section A (see [233]).
My original contribution is, under the supervision of my day-by-day supervisor Dr. Michele Mancuso, the preparation of the bolometer, the installation of the detector in the dilution refrigerator, the operation of the dilution refrigerator, and the collection of the data at the Max Planck Institute for Physics in Munich.

6.1 Abstract

The ^{169}Tm nuclide has first nuclear level at 8.41 keV with magnetic type transition to the ground state and, therefore, can be used as a target nucleus for the search of resonant absorption of solar axions. We plan to use a Tm-containing crystal of a garnet family $Tm_3Al_5O_{12}$ as a bolometric detector in order to search for the excitation of the first nuclear level of ^{169}Tm via the resonant absorption of solar axions. With this perspective in mind, a sample of the $Tm_3Al_5O_{12}$ crystal was grown and tested for its bolometric and optical properties. Measurements of chemical and/or radioactive contaminations were performed as well. In this paper we present the test results and estimate the requirements for a future low-background experimental setup.

6.2 Introduction

With the ongoing search for the dark matter, a hypothetical axion particle remains a valid candidate with robust theoretical motivation. Having been introduced back in 1978, the hypothetical axion was initially supposed to solve the long-standing strong CP-problem in quantum chromodynamics (QCD). The new pseudoscalar particle had to emerge after the newly introduced chiral symmetry had been spontaneously broken at some energy scale f_A, thus compensating the CP-violating term of QCD Lagrangian [24, 26, 25]. The axion interactions with ordinary matter are described in terms of effective coupling constants g_{AN} (nucleons), $g_{A\gamma}$ (photons) and g_{Ae} (leptons). The values of these constants and axion mass m_A appear to be inversely proportional to the symmetry breaking scale f_A in all theoretical models.

The initial model of "standard" axion assumed the chiral symmetry breaking

scale to be comparable to that of the electro-weak interactions ($f_A \approx 250$ GeV), thus making specific predictions regarding axion mass and coupling constants. A series of experiments employing reactors, particle accelerators and artificial radioactive sources were carried out and eventually invalidated the existence of "standard" axion. Nevertheless, there is no principal restrictions on the symmetry breaking scale f_A, which can be made arbitrary large, consequently reducing the expected axion mass and suppressing its interactions with ordinary matter.

Soon, after exclusion of the "standard" axion, new modified models were developed. The axions described in these models were nicknamed "invisible", due to their weak coupling with ordinary matter [234, 235, 236, 237]. Moreover, it turned out that such a particle fits the criteria for a potential dark matter constituent. Thus, the search for axions and axion-like particles is considered an extremely important task.

With the intensely ongoing experimental searches for the dark matter particles there is a constant demand for advancement in low-background techniques as the experiments keep excluding new regions of the parameter space. This paper reports the results of various measurements aimed to study the properties of $Tm_3Al_5O_{12}$, a thulium containing crystal of the garnet family, which can be used to detect the resonant absorption of solar axions [238, 144, 239].

6.3 Thulium as a target material

The majority of the axion experiments can be addressed to one of two major groups: solar axion searches and relic axion searches. Several processes could be responsible for axion production inside the solar core; at present, the main efforts are focused on searching the conversion of solar axions to photons in a macroscopic laboratory magnetic field (CAST [240], IAXO [241]). The spectrum of solar axions, similarly to the spectrum of solar neutrinos, contains a continuous part with average energy about 4 keV, produced by Primakoff effect, Compton-like processes and bremsstrahlung, and several monochromatic lines, associated with the emission of axions in nuclear transitions of magnetic type.

Among the possible axion interactions with ordinary matter, theoretical models describe the resonant absorption of an axion by atomic nuclei via the axion-nucleon (g_{AN}) interaction [129, 242]. The relatively high cross-section of this process allows achieving competitive sensitivity levels on a small scale setup. The search for resonant absorption of monochromatic axions emitted by ^{57}Fe, ^{7}Li and ^{83}Kr nuclei at the Sun was proposed to be carried out in [243, 130, 131], respectively.

The use of ^{169}Tm low-lying nuclear level to search for axions with a continuous spectrum was proposed in [238]. Searches for Primakoff, Compton and bremsstrahlung axions using ^{169}Tm were performed in [144, 239] via the "target-detector" scheme. A significant advantage of experiment with ^{169}Tm target is that the probability of axion emission/absorption in 8.41 keV M1 transition depends weakly on the actual values of two poorly constrained QCD parameters (S and z) as opposed to ^{57}Fe and ^{83}Kr nuclei, for which the probability can vanish in some cases [144]. The sensitivity of the experiments is limited by low detection efficiency, which can be significantly increased by introducing the ^{169}Tm target inside the sensitive volume of the detector.

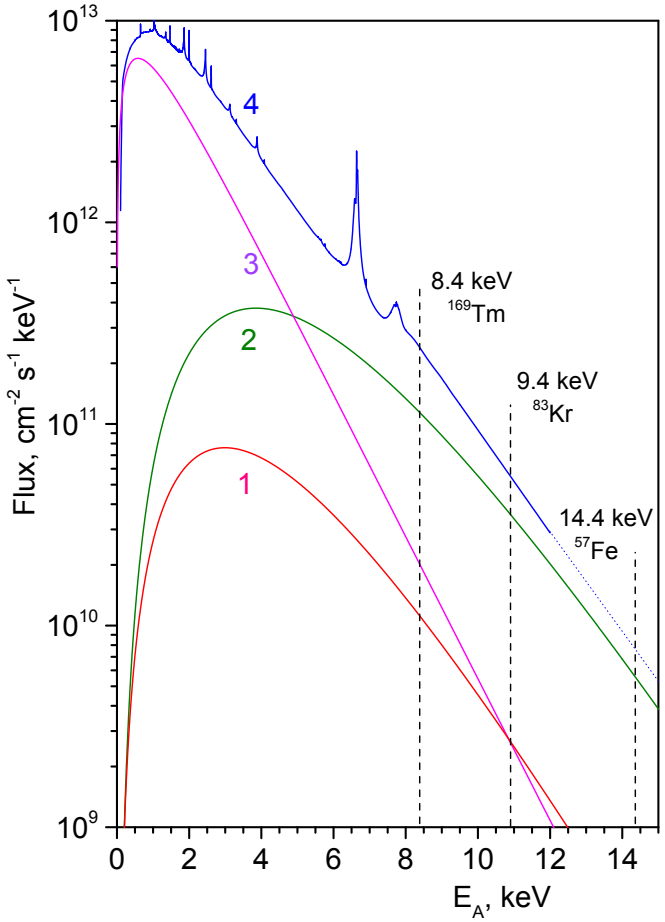

Figure 6.1: Solar axion spectra for Primakoff (1), Compton-like processes (2) and bremsstrahlung (3), calculated for $g_{A\gamma} = 10^{-10}$ GeV^{-1} and $g_{Ae} = 10^{-11}$, correspondingly. The total axion spectrum from the axion-electron coupling is represented by line (4) [128].

A low-background setup equipped with a cryogenic detector constituted by a target containing ^{169}Tm allows one to test the resonant absorption of axions with a detection efficiency close to 100% and a strong suppression of the possible background induced by photons coming from the excited atomic levels. The latter consideration is critical for ^{169}Tm, since it has several energies of characteristic X-rays very close to 8.41 keV γ-line [144]. The first attempts to employ Tm-containing crystals $NaTm(WO_4)_2$ and $NaTm(MoO_4)_2$ as a bolometer detector were undertaken in [244].

In this work we present the first experimental results obtained using a small crystal of $Tm_3Al_5O_{12}$ with size of ($\sim 10 \times 10 \times 10$) mm^3 and weight of 8.18 g. The obtained results prove the feasibility of using the given material in a cryogenic calorimeter detector module and can be used to estimate the specifications for a future full-scale installation.

6.4 Crystal growth characterization

6.4.1 Crystal growth and sample preparation

The $Tm_3Al_5O_{12}$ crystal was fabricated at Kurchatov Institute in Moscow, Russia. The crystal boule was grown from iridium crucible (diameter 40 mm, height 40 mm) by conventional Czochralski technique with RF-heating.

The original raw oxides Y_2O_3(4N), Tm_2O_3(5N) and Al_2O_3(4N) were annealed at 900° C in order to remove moisture. Afterwards, the ingredients were thoroughly mixed in stoichiometric proportion, pressed into tablets, sintered and placed into the crucible for crystal growth. High purity zirconium oxide (4N) was used as thermal insulation to maintain the required temperature conditions inside the system.

The process was carried out in the nitrogen atmosphere with 0.1 % admixture of O_2. The YAG crystal oriented along $\langle 100 \rangle$ axis was used as crystallization seed. The crystal was grown setting a pulling rate of 2 mm/hour and rotation speed of 20 rpm. Such growth conditions provide the formation of the optimal convex shape of the solid-liquid interface.

As a result of the growth process we obtained a 16 mm diameter and 40 mm height boule. This boule was then used to fabricate two crystal samples. Sample #1 was cut from the boule tail, therefore the bottom surface has an irregular shape. Overall, this sample measures ($8 \times 10 \times 10$) mm^3 and weighs 5.5 g. The bottom surface of this sample appeared to be covered in small amount of iridium from crucible, while the rest of the surfaces were clear. This sample was used to perform radiopurity and optical measurements.

Sample #2 was produced from the top part of the boule and has cubic shape with plain cuts on all surfaces. Its dimensions are $10 \times 10 \times 10$ mm^3 with an 8.18 g mass. This sample was used in a cryogenic measurement to test the bolometric properties of the ^{169}Tm-containing garnet.

6.4.2 Optical properties

The absorption and transparency spectra of sample #1 were obtained in LNGS (Italy) using the UV-VIS spectrophotometer within $200 - 700$ nm wavelength range. The normalized absorption spectrum is presented in Fig. 6.2. The spectrum contains two distinct absorption bands, approximately at $350 - 367$ nm and $457 - 477$ nm.

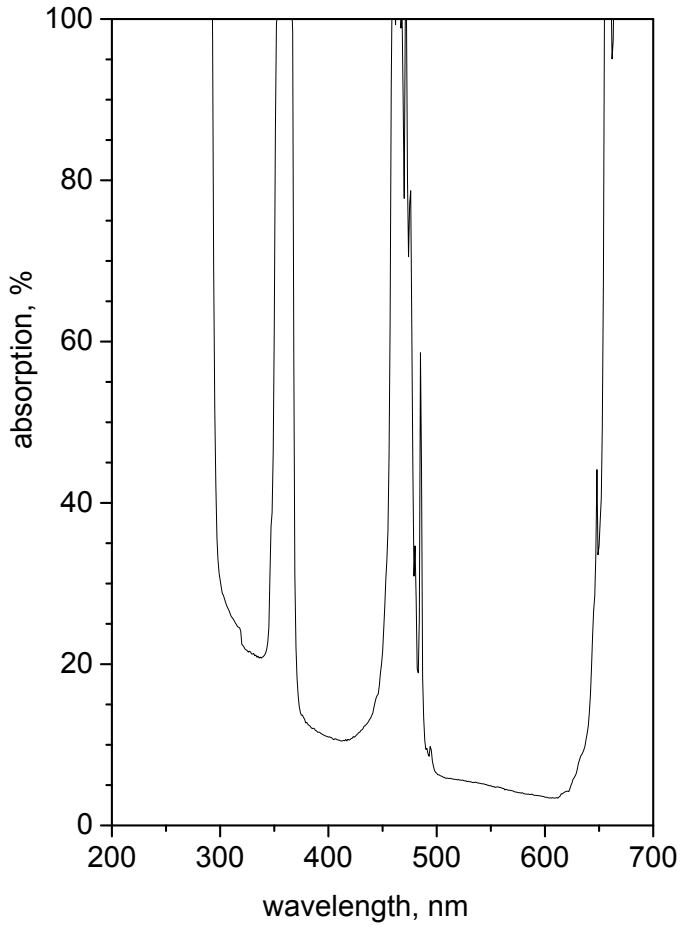

Figure 6.2: Absorption spectrum of the crystal sample #1 for the optical band.

Absorption bands approximately correspond to those associated with ^{169}Tm ions at 460 nm and 681 nm, reported in earlier research of ^{169}Tm-doped YAG [245, 246]. Due to the presence of wide absorption bands within the visible range the use of the crystal as a scintillator would seem ineffective and for now no further investigation of scintillating properties was performed.

6.4.3 Low-background spectrometry

The level of internal radioactive contamination of sample #1 the $Tm_3Al_5O_{12}$ crystal with respect to uranium and thorium natural decay chains, and, in particular, to their daughter nuclides, was investigated by means of γ-ray spectroscopy with an ultra-low background high purity germanium (ULB-HPGe) detector. The measurements were carried out in the STELLA (SubTerranean Low Level Assay) facility in the Gran Sasso National laboratories of the INFN in Assergi, Italy, which provides an average shielding of about 3600 m.w.e. Details about this facility can be found in [247, 248, 249]. The $Tm_3Al_5O_{12}$ crystal sample #1 was placed on a well-type

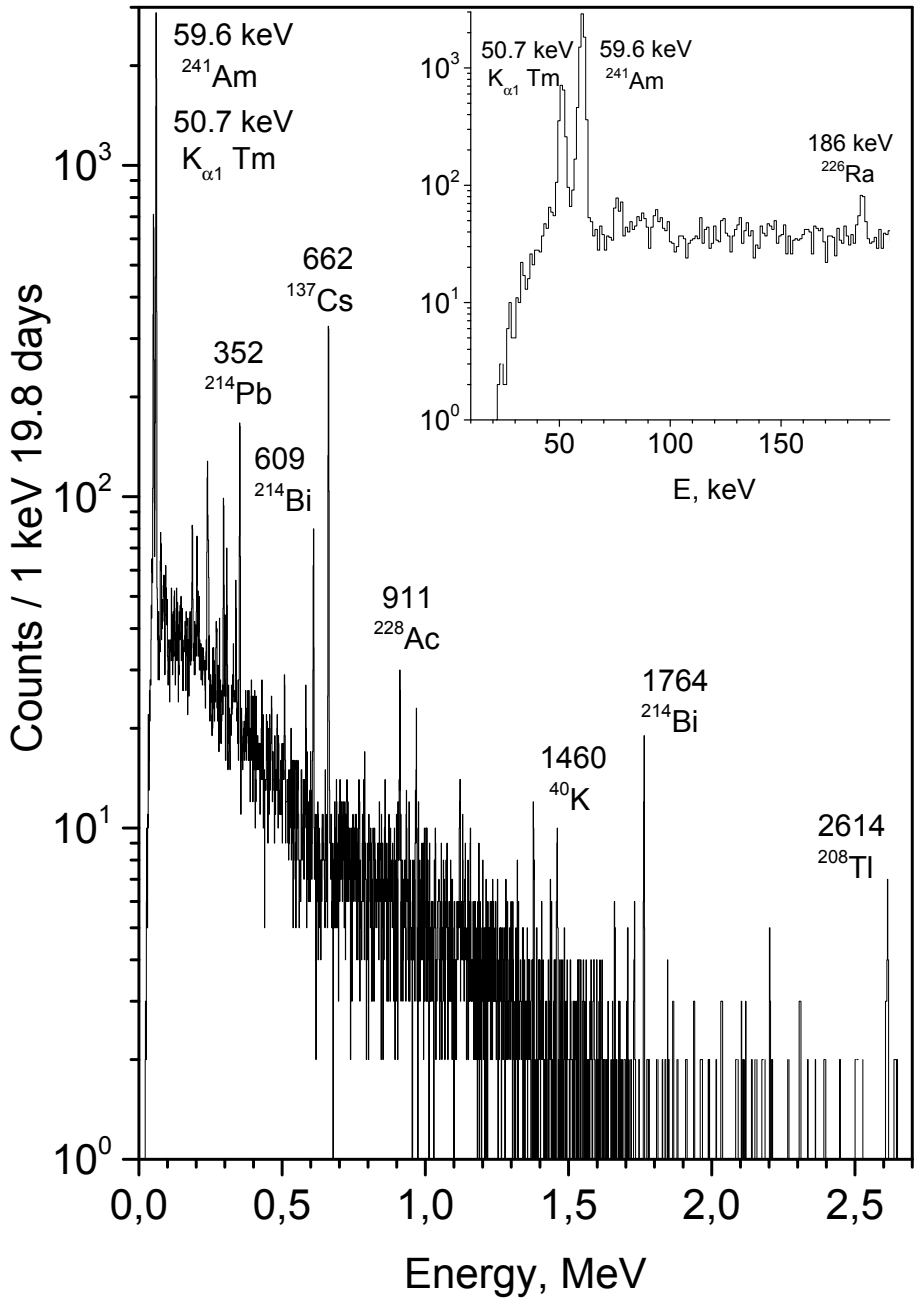

Figure 6.3: Energy spectrum of the crystal sample #1 obtained with Ge detector. The inset shows low-energy part of the spectrum.

ULB-HPGe detector with an active volume of about 160 cm^3. This detector has a rather thin aluminum window of 0.75 mm thickness and has an optimized design for high counting efficiency of small samples in a wide energy range. The germanium detector is surrounded by low-radioactivity lead ($\approx$ 15 cm), copper ($\approx$ 5 cm) and special lead with low content in ^{210}Pb ($\approx$ 5 cm). Finally, the shielding and the detector are housed in a polymethyl metacrylate box that is continuously flushed with pure nitrogen in order to suppress the amount of radon in the vicinity of the detector.

The energy resolution can be approximated in the energy region of 239−2615 keV by the function:

$$\mathrm{FWHM} = (1.41(4) + 0.00197(4) \times E)^{1/2}, \tag{6.1}$$

where E is the energy of detected *gamma*-ray in keV. For instance, the FWHM at 1332.5 keV gamma line of ^{60}Co is 2.0 keV.

The data with the $Tm_3Al_5O_{12}$ crystal sample #1 were taken over 476.63 hours (19.86 days), while the background spectrum was taken over 674.26 hours (28.09 days). The energy spectra of the $Tm_3Al_5O_{12}$ crystal sample normalized to the time of measurement is presented in Fig. 6.3.

The specific activities of the isotopes were calculated using the formula:

$$A = (S_s/t_s - S_b/t_b)/(y \cdot \eta \cdot m), \tag{6.2}$$

where $S_s(S_b)$ is the area of a peak in the sample (background) spectrum, $t_s(t_b)$ is the time of the sample (background) measurement, y is the yield of the corresponding γ-line, η is the efficiency of the full peak detection and m is the mass of the sample. The efficiencies for the full-energy absorption peaks used for the quantitative analysis were obtained through a Monte-Carlo simulation (code MaGe), based on the GEANT4 software package [250]. The values of the limits were obtained using the procedure presented [251]. The nuclides and their activities found in the $Tm_3Al_5O_{12}$ crystal samples are shown in Table 6.1.

The measurements have shown a significant contamination of the crystal sample #1 with ^{241}Am and ^{137}Cs isotopes. The intensity of the 59.6 keV ^{241}Am peak was 370 events/day, which corresponds to the ^{241}Am α-activity of $\sim$ 900 decays/day. ^{241}Am presence within the sample has no clear explanation at the moment. One can speculate that iridium crucible used for the crystal growth had been previously exposed to ^{241}Am-containing material. Sample #1 is also contaminated by La and Lu nuclides, which can be explained by chemical affinity of Tm and Lu/La. Thulium does not occur in the nature in a free state, while it is commercially produced from minerals containing rare earth elements of the lutetium subgroup (from Gd to Lu). Finally, sample #1 contains nuclides from U/Th decay chains. The ratio of ^{235}U/^{238}U is in agreement with natural abundance of uranium isotopes. Secular equilibrium appears to be broken, although this is a typical occurrence in inorganic crystals [252, 253, 254].

It has been demonstrated before for various compounds, that the majority of impurities accumulate at the end of the crystal boule due to the segregation effect [255]. Thus, one could naturally expect that sample #1 from the bottom of the boule should be less radiopure with respect to the sample #2 from the top of the boule.

Chain	Nuclide	Activity [Bq/kg]
^{232}Th	^{228}Ra	0.27 ± 0.04
	^{228}Th	0.22 ± 0.03
^{238}U	^{226}Ra	0.45 ± 0.03
	^{234}Th	2.5 ± 0.9
	^{234m}Pa	≤ 2.3
	^{210}Pb	4 ± 1
^{235}U	^{235}U	0.11 ± 0.02
—	^{40}K	≤ 0.36
	^{60}Co	≤ 0.020
	^{241}Am	94 ± 9
	^{137}Cs	0.85 ± 0.09
	^{176}Lu	0.09 ± 0.01
	^{138}La	0.03 ± 0.01

Table 6.1: The concentration of radionuclides (in Bq/kg) in the $Tm_3Al_5O_{12}$ crystal sample #1, obtained by ULB-HPGe measurements. The upper limits are given with 90% C.L., and the expanded standard uncertainties with $k = 1$.

6.4.4 Mass-spectrometry

A general contamination screening for the wide range of elements was performed via the high-resolution inductively coupled plasma mass-spectrometry (HR-ICP-MS). The measurement was performed by the "Thermo Fisher Scientific ELEMENT2" spectrometer located at the Gran Sasso National laboratories. The material for measurements was obtained from the crystal sample #2 in form of crystal particulates, which were then dissolved in an acid solution and diluted for the measurement. A semi-quantitative analysis was performed, i. e. the instrument was calibrated via a single reference standard solution of thorium and uranium.

While the chemical purity was analyzed with respect to a wide range of elements, we would like to stress the attention on some of them, which have critical importance for crystal quality, or as elements that affects crystal radiopurity. For the most of the elements only the upper limits on concentration were obtained. The obtained concentrations for various elements are presented in Table 6.2.

One could see that transition elements of Fe group that have a huge impact of optical properties of any crystal are practically absent. This confirms the fact that the green tint of $Tm_3Al_5O_{12}$ crystal is caused by Tm ion properties rather than by the presence of such impurities.

The evidence of Ir on the level of 7 ppm is caused by the high rate of material evaporation from the iridium crucible caused by exposure to high temperatures during the crystal growth process. The use of inert atmosphere with a small admixture of oxygen during the crystal production may reduce such evaporation, though it cannot be eliminated completely. One should notice that such concentration of Ir is observed inside the inner crystal volume, while the macroscopic iridium particulates cover one of the surfaces of the crystal sample #2. Other elements of Pt-group are excluded at the concentration levels of less than 0.5 ppm.

Apparently, the whole range of rare earth elements proved to be present in the

Elem.	C [ppm]	Elem.	C [ppm]	Elem.	C [ppm]
K	≤ 21.4	Y	1357.1	Dy	1.6
Ca	15.7	Zr	70.7	Er	6.7
Cr	≤ 3.0	Mo	24.3	Yb	4.8
Mn	≤ 0.7	I	71.4	Lu	3.4
Fe	≤ 21.4	La	2.5	Hf	7.1
Co	≤ 0.4	Ce	3.0	Ir	6.9
Ni	≤ 3.6	Nd	4.4	Tl	2.6
Cu	≤ 0.7	Sm	1.2	Pb	78.6
Zn	0.7	Eu	0.4	Bi	0.4
Ga	1.9	Gd	11.4	Th	≤ 0.1
Br	7.9	Tb	0.3	U	0.1

Table 6.2: The element concentrations (C) in parts per million (ppm) units reported by the ICP MS study of the crystal sample #2.

final crystal material with concentrations of up to tens of ppm. The elements of the Gb sub-group are present in larger amount with respect to the Ce sub-group, due to the the chemical affinity of thulium with the given elements. The presence of Sm and Gd that have α-decaying isotopes with relatively short half-lives may become the source of irreducible background. If the particle interactions are being registered solely via the heat channel such background events would be indistinguishable from the pulses we look for. Thus, for the high sensitivity experiment the concentration of rare earth elements inside the Tm-containing crystal should be thoroughly minimized. The significant yttrium concentration of more than 1300 ppm demonstrate that the declared purity grade (5N) of the Tm oxide powder should be double checked by independent measurements, and a reliable producer of thulium oxide should be selected accordingly.

Presence of the elements like Zn, Ga, Zr, Br, Mo, I, Hf, Tl, Pb, Bi could be possibly explained by instrumental contamination, caused by evaporation from the walls of the crucible, in case those elements were involved in previous crystal growths. Therefore, in order to achieve the high purity Tm-containing crystal one should use a freshly produced iridium crucible and thermal shield.

With respect to the radioactive elements, the measurements showed high concentration of uranium (0.1 ppm) due to chemical affinity with rare earth elements, and the limit was set on the presence of thorium (≤ 0.1 ppm). The limit on potassium concentration was found to be ≤ 22 ppm. The exposure of crystal material to high temperatures during the growth helps to eliminate potassium impurities from the compound due to its high volatility.

6.5 Experimental set-up

The 8.8 g $Tm_3Al_5O_{12}$ crystal (sample #2) is used as main absorber of a cryogenic detector. The absorber is held in position inside a copper holder by two pairs of bronze clamps. One surface of the crystal is coupled to a Neutron Transmutation

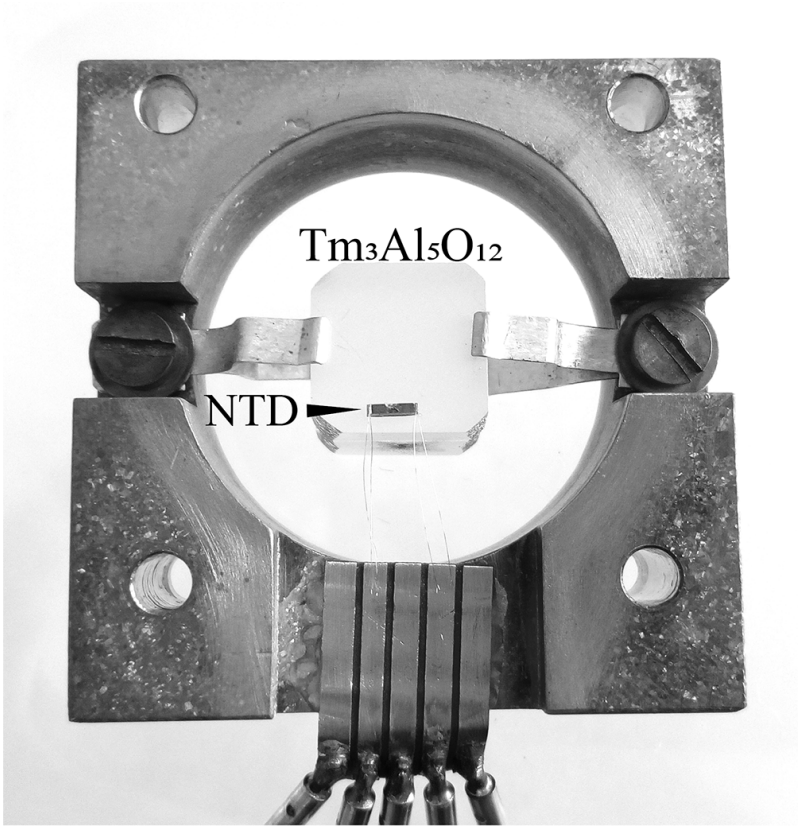

Figure 6.4: $Tm_3Al_5O_{12}$ crystal sample #2 instrumented with a NTD inside the copper holder. Gold bond wires provide thermal and electrical connections to the bond pads glued on the copper holder.

Doped (NTD) sensor [157] through a thin layer of epoxy [1]; electrical and thermal connections are provided to the NTD through a pair of gold bond wires with a 25 μm diameter. This detector (see Fig. 6.4) was operated at the Max-Planck-Institute for Physics (MPI) in Munich, Germany, inside a dilution refrigerator [2] in an above-ground laboratory without any shielding against the environmental and cosmogenic radiation. The detector was mechanically and thermally connected to the coldest point of the dilution refrigerator: $\sim$10 mK was the lowest temperature reached during the measurement. The temperature readout of the NTD is obtained measuring the voltage drop variations of the sensor with a differential voltage amplifier while applying a constant bias current through the NTD. At cryogenic temperatures, a particle interacting inside the target crystal produces a thermal pulse that follows a well-tested model described in [169]. The pulse amplitude is proportional to the energy deposited in the absorber, so,with the help of calibrations sources, it is possible to accurately measure the energy spectrum of the particle interactions above a certain energy threshold E_r.

From [169] we expect a measured particle pulse to be a superposition of two exponential pulses. In our case, however, we had to introduce a third exponential pulse in order to properly describe the pulse shape of a particle interaction taking place inside the $Tm_3Al_5O_{12}$ crystal, as shown in figure 6.5. We attribute this third

[1] GP 12 Allzweck-Epoxidkleber
[2] Kelvinox400HA

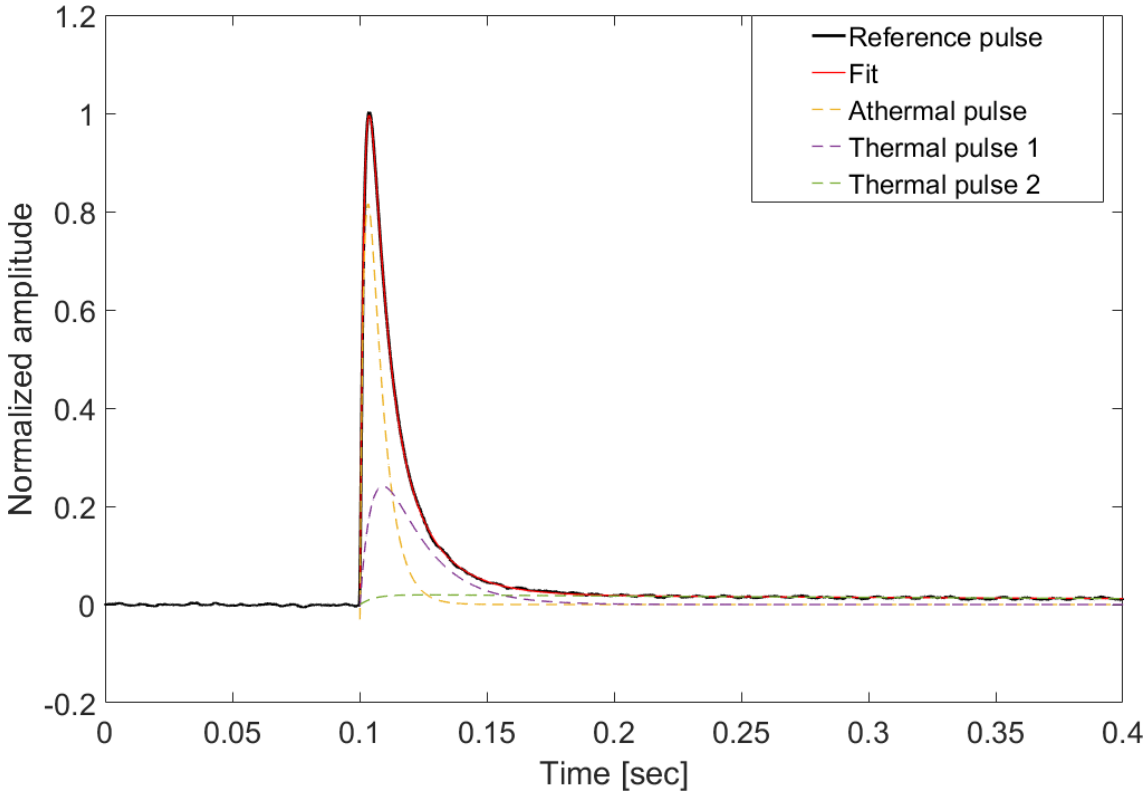

Figure 6.5: In solid black a typical particle interaction inside the $Tm_3Al_5O_{12}$ crystal measured by the NTD. In solid red the parametric fit. In dashed yellow, dashed purple, dashed green the three exponential components: athermal, first thermal component, and second thermal component respectively. The second thermal component is not included in the physical model usually adopted and has a much longer lifetime than the other two exponential components.

exponential pulse to a second thermal component, since a similar effect has already been seen in previous works with cryogenic detectors [256]. The interpretation of this second thermal component is not straightforward and is under investigation. The fit of a typical particle pulse measured by our detector can give useful information about the exponential components such as the life time of non-thermal phonons (τ_n), the intrinsic thermal relaxation time constant of the thermometer (τ_{in}), and the thermal relaxation time constants of the absorber (τ_{t1}, τ_{t2}). The result of the fit in this case leads to τ_n=5.5 ms, τ_{in}=1.9 ms, τ_{t1}=15 ms, and τ_{t2}=560 ms. It is worth noticing that the additional thermal component we introduced (τ_{t2}) appears to live in a long time scale: a thermal component with a long lifetime might affect the accuracy of the energy reconstruction of particle interactions, especially in the presence of a high rate. Thus, it might be even more beneficial than usual to operate this detector in a low background environment.

6.6 Results

This measurement convincingly shows that it is feasible to operate a bolometric detector which employs $Tm_3Al_5O_{12}$ as the absorber. This is, of course, the necessary condition for a cryogenic detector with a new target material. This, of course, is

Isotope	A [Bq/kg]	Isotope	A [Bq/kg]
^{238}U	≤ 0.28	^{232}Th	≤ 0.16
^{235}U	≤ 0.24	^{230}Th	≤ 0.20
^{234}U	≤ 0.14	^{210}Po	≤ 0.33
^{226}Ru	≤ 0.12	^{241}Am	1.4 ± 0.1
^{220}Ru	≤ 0.10	—	—

Table 6.3: Upper limits and values of activities (A) in Bq/kg of U and Th chain contaminants, determined by the bolometric measurement of crystal sample #2 (90% C.L.)

the first goal to achieve before planning a cryogenic experiment based on a given target material. $Tm_3Al_5O_{12}$ is particularly attractive for solar axions search, on the condition that it is possible to obtain an energy threshold $\leq$ 8 keV. Thus, this measurement was also useful to understand how close we are to this design goal with the technology employed. In this first test, we have recorded 3.8 hours of data in a continuous single run. For the analysis we have considered the whole dataset without the application of any cut, in order to preserve the 1.3 g·day exposure. Due to the high content of long living radioactive elements it is possible to immediately identify characteristic features in the energy spectrum, despite the low exposure. A broad peak evidently appears in the spectrum shown in figure 6.6: this peak can be ascribed to the alpha decay of ^{241}Am (5.637 MeV Q-value [257]), the highest contaminant present in the sample.
Consequently, it is possible to use this peak to calibrate the detector response. The results of the peak fitting via the gaussian are given in Fig. 6.6. The peak position corresponds to $Q_\alpha = 5.637$ MeV and was used for energy scale calibration. The peak width was determined to be $\sigma = 110$ keV, although this evaluation might be affected by the complex structure of the peak, which is formed by the escape probabilities of 59.6 keV and 43.4 keV γ-quanta and characteristic X-rays. The number of events within the peak amounts to 155 ± 10 events and corresponds to ^{241}Am activity of 1.4 Bq/kg. The rest of the spectrum does not contain any prominent α-peaks. In order to estimate the activity of various nuclides belonging to U and Th decay chains we used the events within $3\sigma = \pm 330$ keV interval from the Q_α value. The spectrum was fit by gaussian with fixed parameters of $x_0 = Q_\alpha$ and $\sigma = 110$ keV, while the peak area and the background constant remained free. The obtained upper limits for activity of some isotopes are given in Tab. 6.3. Mixed $\alpha - \beta$ decays from ^{214}Bi-^{214}Po and ^{212}Bi-^{212}Po decay chains appear in the spectrum as single events: unfortunately, time-coincidence techniques cannot be employed due to the relatively slow pulses of the bolometric detectors.
The measured activities are considerably smaller than the ones measured in Gran Sasso, pointing towards a strong segregation of the contaminants during the crystal growth. To estimate the background introduced by these contaminants at the energy of interest ($\sim$8 keV) a further investigation on the internal contamination of this crystal is needed.

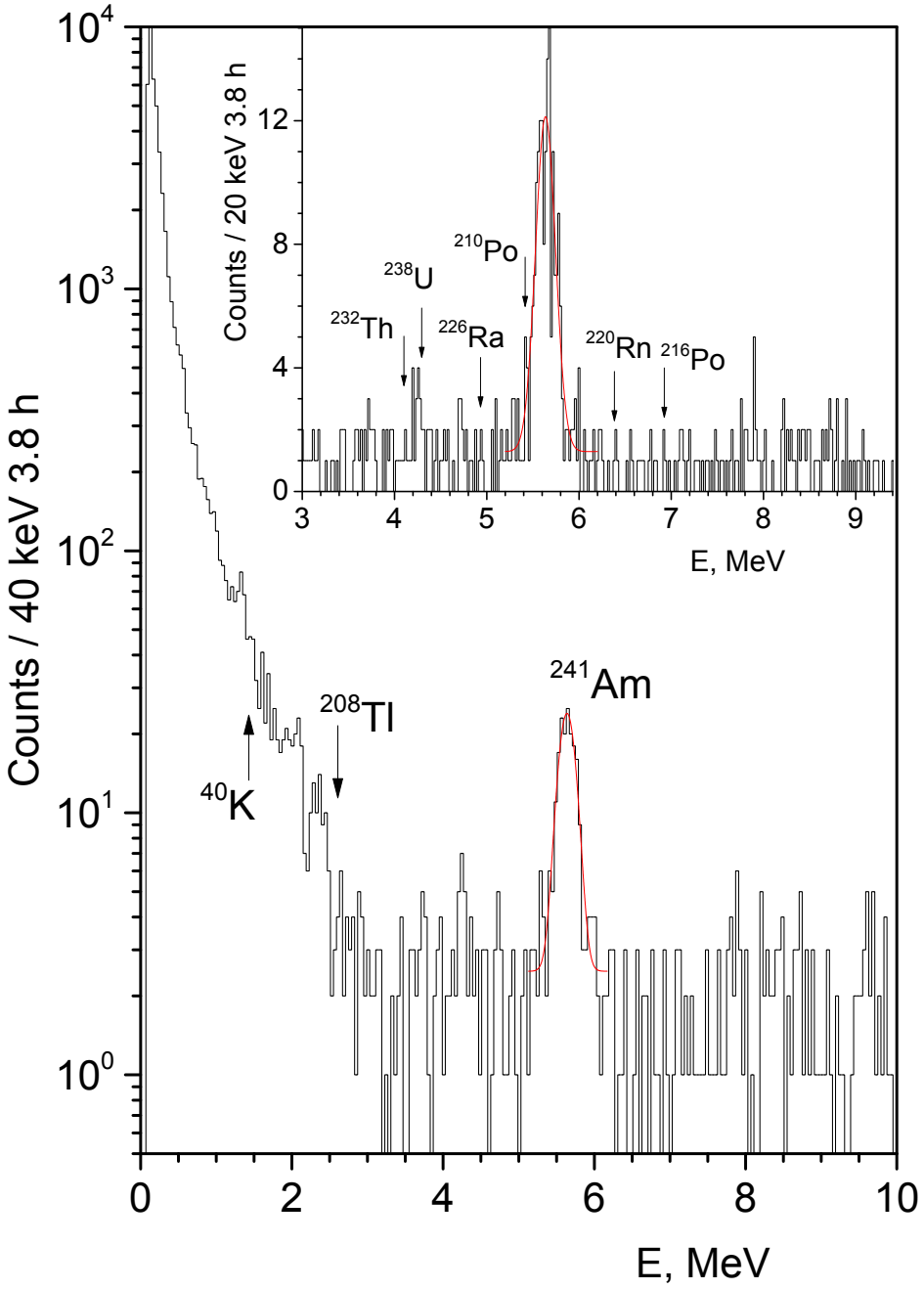

Figure 6.6: Energy spectrum measured by the NTD for a 1.3 g·day exposure. Ths inset shows the energy interval where α-peaks of ^{238}U and ^{232}Th chains should be manifested. The energy calibration was obtained using the mean value of a broad peak that we attribute to the 5.637 MeV alpha decay of ^{241}Am, the main contaminant present in the crystal.

6.7 Conclusions

The performed measurements have proven for the first time the feasibility of operating a thulium-containing crystal as a cryogenic bolometer. The obtained baseline resolution amounted to 22.75 ± 0.65 keV, which translates to energy threshold E_{th} of about 170 keV. The phonon events pulse shape was well-fitted via the four time constraints fit, where the longest component (560 ms).

While the principle possibility of operating a thulium-based material in a cryogenic set-up has been confirmed, it is clear that further optimization is needed in order to achieve the required sensitivity for the solar axion search. In order to obtain physical results we need an improvement of more than one order of magnitude for the energy threshold, which might be in reach using a CRESST-like detector with a TES as thermal sensor: CRESST has already demonstrated the ability to obtain outstanding energy thresholds employing small crystals (30.1 eV with a 24 g $CaWO_4$ crystal [122] and 19.7 eV with a 0.5 g Al_2O_3 crystal [171]).

The screening of Tm-based compound revealed significant contamination by U/Th decay chains at the level of few Bq/kg. The crystal also contains isotope ^{137}Cs with activity of about 1 Bq/kg, as well as radioactive nuclides ^{176}Lu and ^{138}La that accompany rare earth metals in raw materials (Tm_2O_3(5N) and Y_2O_3(4N) powders). The presence of ^{241}Am at the level of 100 Bq/kg together with ^{137}Cs in the bulk of the crystal remains poorly understood, not excluding the possible contamination from growth equipment or raw materials.

In order to produce the low-background Tm-containing crystal that will meet the requirements for chemical and radioactive purity one should exercise additional precautions during the crystal production and handling, including pre-growth purification of Tm_2O_3(5N) and Y_2O_3(4N) powders against U/Th chain nuclides and thorough screening of the growth equipment to be used. Further investigations of the application of the Tm-containing crystal as a cryogenic bolometer are ongoing.

Chapter 7

New limits on the resonant absorption of solar axions by ^{169}Tm

The content of this chapter was published as a collaborative effort in The European Physical Journal C (see [258]).
Under the supervision of my day-by-day supervisor Dr. Michele Mancuso, I prepared the prototype used in this work. This includes the cleanroom fabrication of the TES, bonding the sensor, and installing the calibration source.
Together, we installed the detector in the dilution refrigerator, operated the dilution refrigerator, and acquired the data leading to the publication.
I also triggered the data and performed an independent analysis of the data to check the validity of the energy calibration used in the analysis showed in this work.
I wrote Section 7.4, Section 7.6, and large parts of Section 7.5. I prepared figure 7.2.

7.1 Abstract

A search for resonant absorption of solar axions by ^{169}Tm nuclei was carried out. A newly developed approach involving low-background cryogenic bolometer based on $Tm_3Al_5O_{12}$ crystal was used that allowed for significant improvement of sensitivity in comparison with previous ^{169}Tm based experiments. The measurements performed with 8.18 g crystal during 6.6 days exposure yielded the following limits on axion couplings: $|g_{A\gamma}(g^0_{AN}+g^3_{AN}) \leq 1.44\times10^{-14}\,\mathrm{GeV}^{-1}$ and $|g_{Ae}(g^0_{AN}+g^3_{AN}) \leq 2.81\times10^{-16}$.

7.2 Introduction

Originally, axions were introduced as hypothetical bosons produced by a spontaneous breaking of newly introduced chiral symmetry at some energy scale f_A [24, 26, 25]. The initial model of "standard" axion assumed the symmetry-breaking scale f_A to be similar to the electro-weak interactions scale, but subsequently it was excluded by a series of experiments (the extensive list can be found in corresponding section of [36]). Afterwards, the initial axion model has been expanded into two classes of "invisible" axion models: hadronic (KSVZ) axion [234, 235] and GUT (DFSZ) axion [237, 236]. These models allow f_A to be arbitrary large, therefore reducing the expected axion mass and suppressing the axion interactions with ordinary matter, effectively rendering it "invisible".

The limit on the axion mass m_A is obtained as a consequence of the experimental limits on the effective coupling constants of axion with photons ($g_{A\gamma}$), electrons (g_{Ae}) and nucleons (g_{AN}). Axion coupling constants appear to be significantly model-dependent, so in principle it is possible to consider more general class of axion-like particles (ALPs) with their masses and coupling constants being independent parameters. Axions and ALPs remain suitable dark matter candidates, motivating the experimental effort to search for these particles.

The axion mass m_A can be expressed through the properties of π^0-meson [259]:

$$m_A = \frac{m_\pi f_\pi}{f_A}\left(\frac{z}{(1+z)(1+z+w)}\right)^{1/2}, \tag{7.1}$$

where m_π and f_π are respectively the pion mass and decay constant, while $z = m_u/m_d$ and $w = m_u/m_s$ are the quark mass ratios.

In a laboratory environment axions could be potentially observed via various processes with different axion couplings. The Primakoff effect allows the conversion of axion into a detectable photon inside strong magnetic fields ($g_{A\gamma}$) or the axion decay into 2 γ-quanta. Axion interaction with electrons of atomic shells (g_{Ae}) can cause axio-electric effect (similarly to the photo-ionization) or Compton-like processes. Finally, since the axion is a pseudoscalar boson it can undergo resonant absorption or emission in nuclear transitions of magnetic type (g_{AN}).

The resonant absorption can be used for detection of solar axions in experimental setup with a target containing a nuclide with magnetic type transition to the ground state. The general idea behind this approach is that, due to the presence of g_{AN} coupling, the axions could be resonantly absorbed by the target nucleus N possessing the relevant excited state. After the absorption, the excited nucleus N^* will consequently discharge, emitting the γ-quantum: $A + N \to N^* \to N + \gamma$. The proposals for experiments aimed for registration of monochromatic solar axions produced by ^{57}Fe, ^{7}Li, ^{83}Kr and ^{169}Tm nuclei were originally made in [243, 130, 131, 144], correspondingly.

The main benefit of g_{AN}-based detection technique comes from the resonant nature of the absorption process, which provides high reaction cross-section and, therefore, a possibility of achieving competitive sensitivity even with a relatively small-scale experimental setup. A "solid target + semiconductor detector" layout has been successfully employed for previous axion searches with various targets (^{7}Li [140], ^{169}Tm [178], ^{57}Fe [141]). On the other hand, ^{57}Fe and ^{169}Tm nuclei have low-energy excited states with significant conversion ratios ($\eta \sim 10^{-3}$), so the most transitions would actually produce conversion or Auger electrons and characteristic X-rays, instead of nuclear γ-quanta. Intensive self absorption of these particles inside the target material effectively limits the usable target mass by several grams, thus constraining the potentially achievable sensitivity of this approach.

A natural solution for this problem would be the introduction of the target material inside the active volume of the detector. This approach was implemented in experiments with gaseous ^{83}Kr target and proportional counter located at the underground facility of Baksan Neutrino Observatory [260, 143].

In this paper we aim to detect solar axions via the resonant absorption by ^{169}Tm target, similarly to a series of previous axion searches with ^{169}Tm targets performed at Petersburg Nuclear Physics Institute [144, 178, 239]. The measurement presented here uses the recently developed approach with cryogenic bolometer based on Tm-

containing crystal of a garnet family ($Tm_3Al_5O_{12}$) [233]. We show a significant improvement of the experimental sensitivity thanks to the inclusion of ^{169}Tm inside the active volume of the detector and demonstrate the potential feasibility of this approach for a kg-scale installation.

7.3 Axion rate estimation

The most intense source of axions for an experiment based on Earth is constituted by the Sun. There are several expected mechanisms of axion production that can take place inside stars. Axions can be produced as a result of Primakoff effect due to the axion-photon coupling ($g_{A\gamma}$). The axion-electron coupling (g_{Ae}) allows for several axion-yielding reactions: atomic de-excitation and recombination, electron-nucleus and electron-electron bremsstrahlung and Compton-like scattering. Finally, stellar cores possess high enough temperatures for the thermal excitation of low-energy nuclear levels of magnetic type (~ 1 keV scale), which could emit axions during the de-excitation (g_{AN} coupling).

7.3.1 Solar axion flux

The axion-photon coupling is determined by the following expression [261, 262]:

$$g_{A\gamma} = \frac{\alpha}{2\pi f_A}\left(\frac{E}{N} - \frac{2(4+z)}{3(1+z)}\right) = \frac{\alpha}{2\pi f_A} C_{A\gamma} \tag{7.2}$$

where $\alpha \approx 1/137$ is the fine structure constant and E/N is the ratio between electromagnetic and color anomalies. The value of E/N depends on the particular axion model: in case of DFSZ-axion $E/N = 8/3$ while in the original KSVZ model $E/N = 0$ [261].

The differential energy spectrum of Primakoff axions is calculated [263, 264, 265] based on the radial distributions of temperature and electron density provided by the Standard Solar Model (SSM). The shape of Primakoff axion spectrum calculated for nominal value $g_{A\gamma} = 10^{-10}\,\mathrm{GeV}^{-1}$ is presented in Figure 7.1. The continuous flux has a maximum at ~ 4 keV and becomes negligible at energies beyond 20 keV. In case of ^{169}Tm as a target, the axion flux at 8.41 keV would remain relatively significant at about $\sim 10\,\%$ of its maximum value.

The axion-electron coupling depends significantly on the type of axion model. In case of DFSZ axion the direct coupling to leptons is allowed and the constant g_{Ae} depends on electron mass m_e as:

$$g_{Ae} = \frac{1}{3}\cos^2\beta \cdot \frac{m_e}{f_A} \tag{7.3}$$

where β is an arbitrary angle.

In KSVZ model axions can not interact with leptons directly, but the coupling via the radiative loops remains possible [262]:

$$g_{Ae} = \frac{3\alpha^2 n m_e}{2\pi f_A}\left(\frac{E}{N}\ln\frac{f_A}{m_e} - \frac{2}{3}\cdot\frac{4+z+w}{1+z+w}\ln\frac{\Lambda}{m_e}\right) \tag{7.4}$$

where the QCD cutoff scale $\Lambda \approx 1$ GeV. Consequently, in this case the axion-electron coupling is suppressed by a factor α^2.

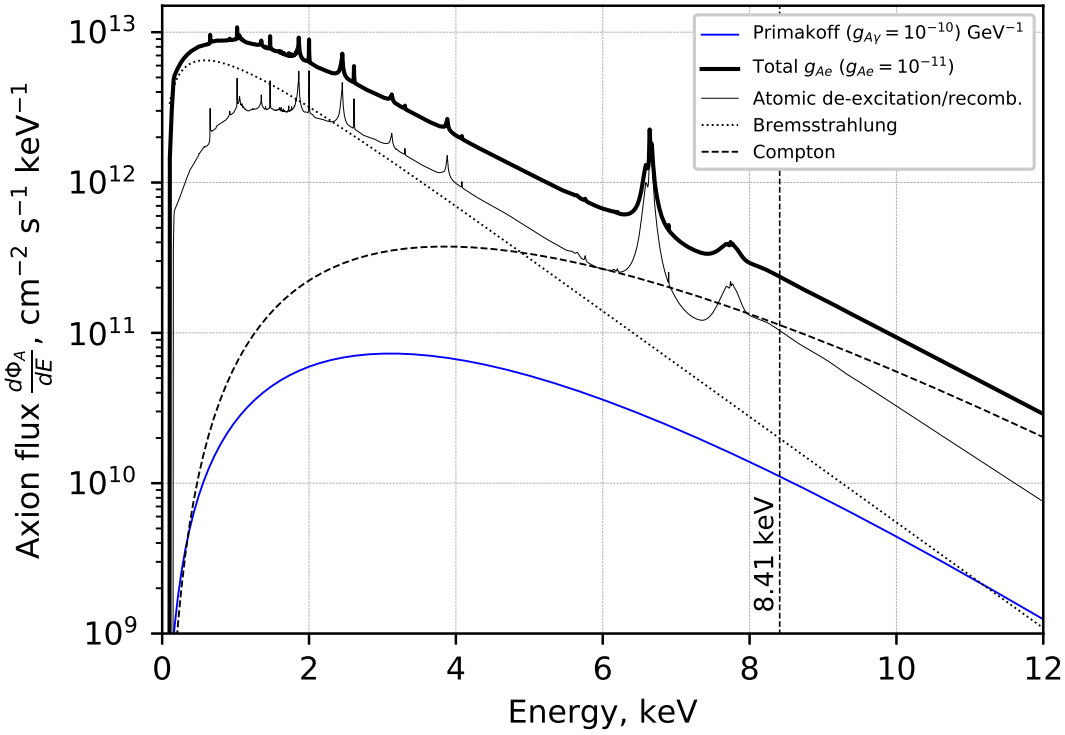

Figure 7.1: The calculated energy spectra of solar axions produced due to the axion-photon [265] and axion-electron couplings [128]. The spectra are calculated in assumption of massless axion ($m_A = 0$) for nominal $g_{A\gamma}$ and g_{Ae} values relevant to the range of experimental sensitivity.

The expected flux of axions produced in the Sun via the axion-electron coupling (g_{Ae}) is calculated using cross-sections for Compton processes [266, 267] and bremsstrahlung [236], SSM data on the electron gas density, temperature distribution and concentrations of various elements [239, 268]. A recent work [128] also includes the axion production via the processes of atomic recombination and de-excitation, which adds additional linear structure on top of the continuous Compton/bremsstrahlung spectra.

The shape of total g_{Ae}-related axion spectrum (together with Compton and bremsstrahlung components) calculated for the nominal value of $g_{Ae} = 10^{-11}$ is given in Figure 7.1. At lower energies below ~ 5 keV bremsstrahlung axions constitute the most part of g_{Ae} axion flux, while above ~ 5 keV Compton axions become dominant.

It is important to note that for both axion couplings the value of solar flux Φ_A at a given axion energy E_A appears to be proportional to the square of the relevant coupling constant:

$$\Phi_{Ax}(E_A) \propto C_{Ax} \cdot g_{Ax}^2 \tag{7.5}$$

where C_{Ax} is a constant determined for a given axion coupling g_{Ax}.

7.3.2 Resonant absorption of axions by atomic nuclei

The cross-section for the resonant absorption of incident solar axions with energy E_A is expressed in a similar fashion as the conventional γ-ray absorption, corrected by emission probability ω_A/ω_γ. The axion absorption rate for ^{169}Tm can be presented as [144]:

$$R_A = \pi\sigma_{0\gamma}\Gamma\frac{d\Phi_A}{dE_A}(E_A = 8.41\text{ keV})\left(\frac{\omega_A}{\omega_\gamma}\right) \tag{7.6}$$

where $\sigma_{0\gamma}$ is the maximum cross-section of γ-ray absorption, Γ is the width of energy level, ω_A and ω_γ are respectively the probabilities of axion or photon emission.

The probability ratio ω_A/ω_γ was calculated in [269, 242] using the long wave approximation:

$$\frac{\omega_A}{\omega_\gamma} = \frac{1}{2\pi\alpha}\frac{1}{1+\delta^2}\left[\frac{g^0_{AN}\beta + g^3_{AN}}{(\mu_0 - 0.5)\beta + \mu_3 - \eta}\right]^2\left(\frac{p_A}{p_\gamma}\right)^3 \tag{7.7}$$

where p_γ and p_A are respectively the photon and axion momenta; $\mu_0 = \mu_p + \mu_n \approx 0.88$ and $\mu_3 = \mu_p - \mu_n \approx 4.71$ are the isoscalar and isovector nuclear magnetic momenta, β and η are parameters derived from the nuclear matrix elements of a particular target isotope. In case of ^{169}Tm, using the one-particle approximation, these parameters can be approximated as $\beta \approx 1.0$ and $\eta \approx 0.5$, yielding the expression for ω_A/ω_γ as [144]:

$$\frac{\omega_A}{\omega_\gamma} = 1.03(g^0_{AN} + g^3_{AN})^2(p_A/p_\gamma)^3 \tag{7.8}$$

In the framework of KSVZ axion model, the axion-nucleon coupling g_{AN} consisting of the isoscalar g^0_{AN} and isovector g^3_{AN} terms can be expressed through the f_A value [261, 262]:

$$g^0_{AN} = -\frac{m_N}{6f_A}\left[2S + (3F - D)\frac{1+z+2w}{1+z+w}\right] \tag{7.9}$$

and

$$g^3_{AN} = -\frac{m_N}{2f_A}\left[(F + D)\frac{1-z}{1+z+w}\right] \tag{7.10}$$

where $m_N \approx 939\,\text{MeV}$ is the nucleon mass, z and w are quark mass ratios, and F, D, S are axial and singlet coupling parameters. The values of F and D are experimentally obtained from the observations of hyperon semi-leptonic decays [270]: $F = 0.462 \pm 0.011$ and $D = 0.808 \pm 0.006$, for various solar axion fluxes.

The singlet coupling parameter S represents the contribution of quarks to the polarization of the nucleon. The experimental restrictions on the value of S, obtained in [271, 272], are $(0.27 \leq S \leq 0.41)$. Nevertheless, in further calculations we assume $S = 0.5$ for convenience of result comparison, since this value is commonly used in previous works and in other experiments.

The model independent expression for the rate of axion absorption by ^{169}Tm nucleus (7.6) then can be derived from flux expression (7.5) and ω_A/ω_γ ratio (7.8):

$$R_A = C_{Ax} \cdot g^2_{Ax} \cdot (g^0_{AN} + g^3_{AN})^2 \cdot (p_A/p_\gamma)^3 \tag{7.11}$$

where counting rate R_A is expressed here in $\text{atom}^{-1}\cdot\text{s}^{-1}$ units. The constant C_{Ax} has a cumulative value defined by axion model parameters, properties of target nucleus, etc. — in case of ^{169}Tm target $C_{A\gamma} = 104$ and $C_{Ae} = 2.76 \times 10^5$ [144, 128].

Then, using the relations between axion mass m_A and axion-nuclei coupling g_{AN} (7.9, 7.10) it becomes possible to express the absorption rate as a function of axion coupling g_{Ax} and m_A (in eV units):

$$R_A = C'_{Ax} \cdot g^2_{Ax} \cdot m^2_A \cdot (p_A/p_\gamma)^3 \tag{7.12}$$

$$(C'_{A\gamma} = 4.08 \times 10^{-13},\ C'_{Ae} = 1.03 \times 10^{-9})$$

Finally, by employing expressions for m_A (7.1), $g_{A\gamma}$ (7.2) and g_{Ae} (7.3, 7.4) we obtain the dependence of axion absorption rate R_A directly on the axion mass m_A (in eV units):

$$R_A = C''_{Ax} \cdot m^4_A \cdot (p_A/p_\gamma)^3 \tag{7.13}$$

$$(C''_{A\gamma} = 6.64 \times 10^{-32},\ C''_{Ae} = 8.08 \times 10^{-31})$$

The total number of expected "axion" events is determined by the target mass (i.e. number of ^{169}Tm nuclei), detector efficiency and total live time of the measurement. The detection probability of the resulting "axion" peak depends on the background level and on the energy resolution of the experiment.

7.4 Cryogenic bolometer and experimental setup

In a recent work [233], we demonstrated the possibility to operate a cryogenic bolometer based on the thulium-containing crystal $Tm_3Al_5O_{12}$. This first prototype showed promising results, but the energy threshold achieved was rather far from meeting the minimum benchmark to be sensitive to the resonant absorption of solar axions in ^{169}Tm.

In order to improve the energy threshold and the energy resolution of a cryogenic bolometer based on a $Tm_3Al_5O_{12}$ crystal the type of phonon sensor has been changed, replacing the Neutron Transmutation Doped (NTD) sensor with a Transition Edge Sensor (TES). First, the same $Tm_3Al_5O_{12}$ crystal used in [233] has been processed with dichloromethane (CH_2Cl_2) in order to remove the glue and the NTD sensor. After that, a CRESST-like TES [167] has been evaporated on the crystal surface.

The TES is constituted by a thin strip of tungsten with two large aluminum pads partially overlapping the tungsten layer. These aluminum pads have two different features: they serve as phonon collectors and bond pads. These pads are connected via a pair of 25 μm aluminum bond wires through which the bias current is injected. The tungsten film is also connected by a long and thin strip of gold to a thicker gold bond pad on which a 25 μm gold wire is bonded. This bond serves as thermal link between the sensor and the heat bath at ~ 10 mK.

On the same surface, but separated from the TES, we also evaporate a heater. The heater is made of a thin strip of gold with two aluminum pads deposited on top. These pads are also bonded with a pair of 25 μm aluminum bond wires through which a tunable current can be injected to maintain the TES at the desired temperature. The heater is also used to inject artificial pulses in order to monitor the detector response over time and to refine the energy calibration during the data analysis.

We would like to highlight that this is the first time a TES is directly evaporated on a crystal containing ^{169}Tm. In Figure 7.2 we show the crystal after the TES deposition along with a sketch of the TES design.

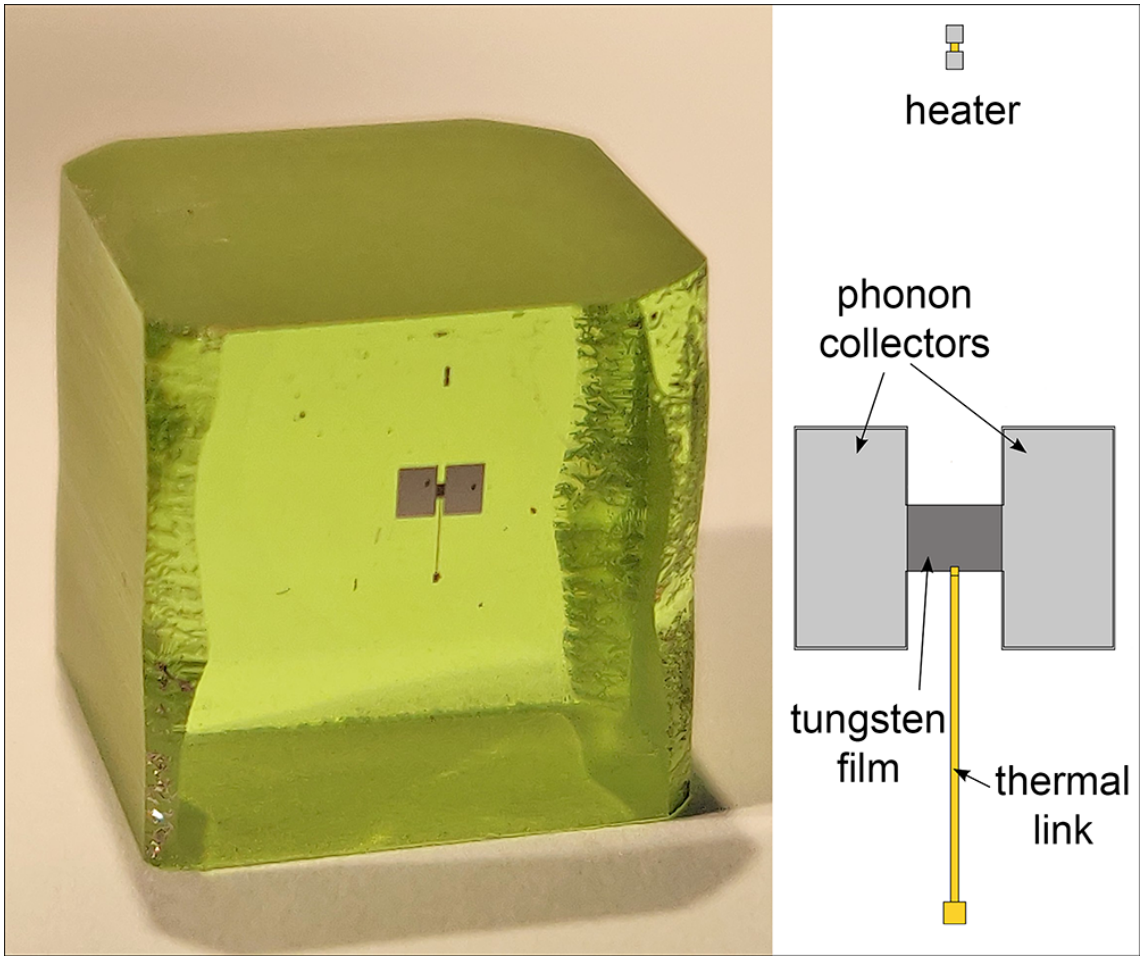

Figure 7.2: **Left**: $Tm_3Al_5O_{12}$ crystal after the TES deposition. It is possible to see two large aluminum phonon collectors (light gray) evaporated on top of a darker strip of tungsten. Closer to the upper edge of the crystal surface there is the heater made of a thin strip of gold with two aluminum pads deposited on top. **Right**: A sketch of a similar TES design [273].

After the TES deposition, the crystal was placed inside a copper holder where it was held in position by a pair of CuBe clamps. Inside the holder, we place a ^{55}Fe X-ray source with activity of $\sim 0.4\,$Bq at a distance of $\sim 1\,$mm from one of the crystal surfaces. This X-ray source is used for the energy calibration of the detector. Finally, the holder is mechanically coupled to the coldest stage of a Leiden Cryogenics dilution refrigerator located in an above-ground laboratory at the Max Planck Institute for Physics (MPP) in Munich, Germany. It has to be noted that in this laboratory there is no shielding against environmental and cosmic radiation.

A temperature of $\sim 10\,$mK has been maintained over the course of the whole run at the coldest stage of the dilution refrigerator. The TES has a critical temperature $T_C = 23\,$mK, thus the operating point is stabilized around this value injecting an appropriate current through the heater. The readout of the TES is obtained with a commercial SQUID system[1], combined with a CRESST-like detector control system [166]. The start of the run has been reserved for a first energy calibration with a ^{57}Co source placed outside of the dilution refrigerator. After this initial calibration, we have collected background data for solar axion search.

7.5 Data analysis and results

The background data acquisition has lasted for 6.60 days of total measurement time. To precisely evaluate the effective measurement time in the region of interest we created a copy of the data where we blindly inject simulated pulses of 8.41 keV with a rate of $1.6\,\text{mBq}\cdot\text{s}^{-1}$, ~ 1000 times smaller than the total rate observed from environmental radioactivity. The data with the simulated pulses were triggered and analyzed in the same way as the background data collected, hence the fraction of survived simulated pulses corresponds to the survival probability of a hypothetical signal.After the trigger, the effective measurement time in the energy region of interest is 3.89 days, with a significant reduction to the respect of the total measurement time. This is due to the trigger dead time, which is naturally high in an above-ground experimental setup.

One stability cut and two quality cuts are applied to the data, with the effective measurement time further reduced to 3.86 days. The stability cut rejects the periods of time when the detector is not in the desired working point, while the quality cuts reject pile-up events and artifacts in the data. The quality cuts are based on two different pulse shape parameters. The overall exposure is equal to $31.6\,\text{g}\cdot\text{day}$ with a ^{169}Tm exposure of $19.2\,\text{g}\cdot\text{day}$.

The acquired spectrum of events in $3 - 20\,$keV energy interval is presented in Figure 7.3. The energy calibration has been performed using a combination of the injected heater pulses and the characteristic peak induced by the presence of the ^{55}Fe source. The injected heater pulses have three different amplitudes and are continually sent throughout the data acquisition. Using this information we can monitor the stability of the detector and correct for any unwanted drift of the operating point. The energy resolution of the detector is not sufficient to resolve $K_{\alpha 1}$, $K_{\alpha 2}$ and $K_{\beta 1+3}$ characteristic X-ray lines of Mn induced by the ^{55}Fe source, thus in the spectrum only a single peak centered around 5.895 keV is visible.

There is no significant excess of events in the vicinity of 8.41 keV. Hence, in

[1] Applied Physics System model 581 DC SQUID

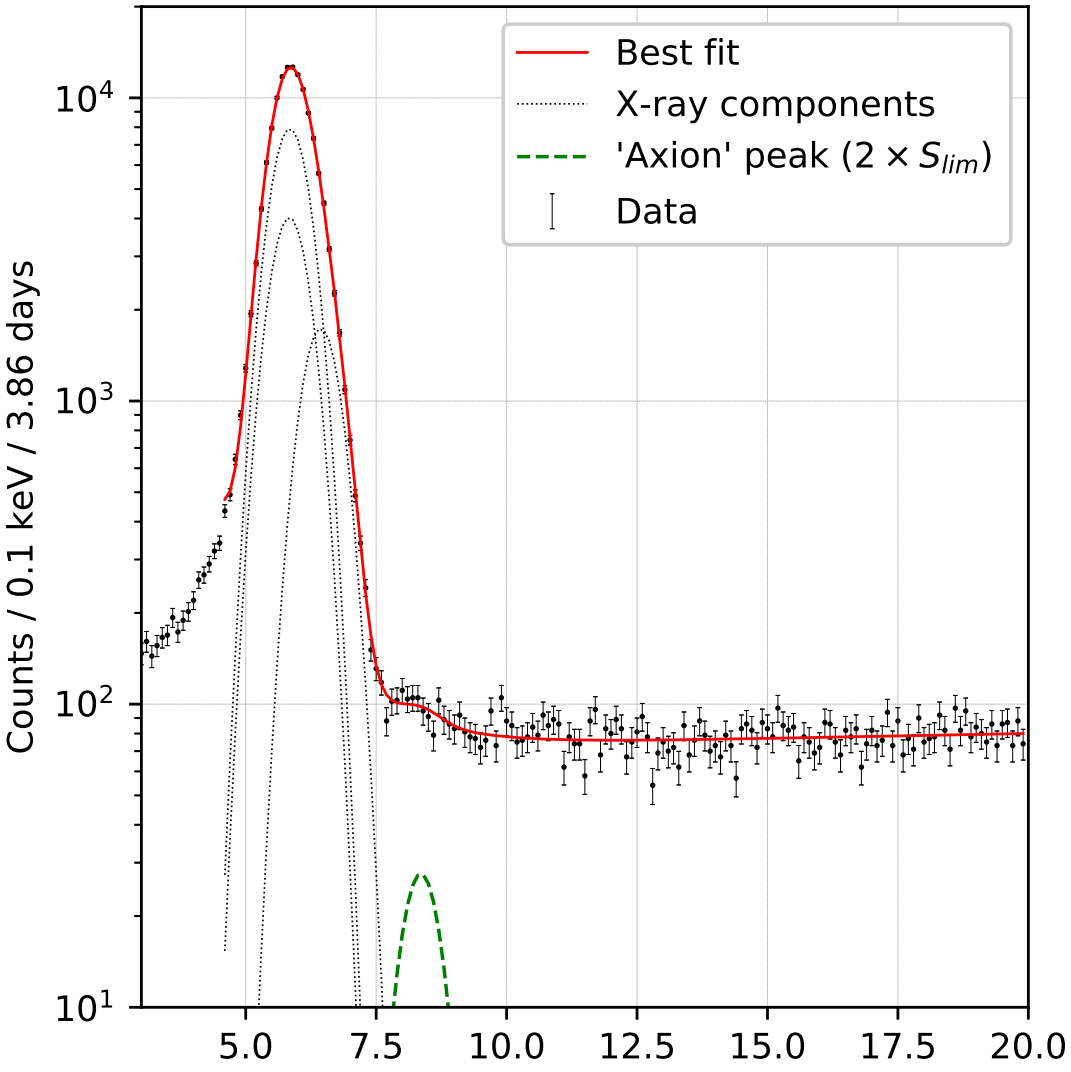

Figure 7.3: Spectrum of events obtained during the live time of 3.9 days by $Tm_3Al_5O_{12}$ bolometer in $3-20$ keV energy interval with 0.1 keV binning. The result of fitting by model (7.14) is presented by solid line. The presumed "axion" peak with area $S = 2 \times S_{lim}$ is shown by the dashed line (the area is increased to improve visibility).

order to determine the upper limit on the number of events in the "axion peak" a maximum likelihood method has been employed. The fit function is chosen as a sum of exponential background, three Gaussians describing $K_{\alpha 1}$, $K_{\alpha 2}$, K_β X-rays of Mn and the expected "axion" peak, all with the same energy resolution σ:

$$N(E) = a + b \cdot E + c \cdot e^{-\frac{(E-4)}{d}} + \sum_{i=1}^{4} S_i e^{-\frac{(E_i - E)^2}{2\sigma^2}} \tag{7.14}$$

The shape of the unresolved Mn X-ray peak is described by sum of three Gaussians, representing $K_{\alpha 1}$, $K_{\alpha 2}$ and K_β lines. All Gaussian positions, including the axion peak, are set relative to the position of the brightest $K_{\alpha 1}$ line ($E_{\alpha 1}$). The intensities of $K_{\alpha 1}$, K_β and axion peak are free, while the intensity of the $K_{\alpha 2}$ is set relatively to $S_{\alpha 1}$. In total, there are 9 free fit parameters: 4 background coefficients (a, b, c, d) and 5 peak parameters (σ, $E_{\alpha 1}$, $S_{\alpha 1}$, S_β, S_A). The exponential model of the background fails below 5 keV, so in order to avoid the introduction of additional parameters we chose to raise the lower border of fit interval to 4.6 keV, since this non-linear background should not make any significant contribution at 8.31 keV. The best fit with reduced chi-squared criterion $\chi^2/N_{DoF} = 171.1/(154-9) = 1.18$ is presented in Fig. 7.3 by a solid line. The determined energy resolution amounted to $\sigma = 0.370$ keV.

In order to determine the upper limit on the 8.41 keV peak intensity a standard approach of χ^2-profiling was employed. The value of χ^2 is determined for different fixed values of S_A while the other parameters remain unconstrained. The obtained probability function $P(\chi^2)$ is normalized to unity for $S_A \geq 0$. The upper limit estimated in this manner is $S_{lim} = 128$ at 90 % confidence level.

The upper limit on the amount of measured "axion" events S_{lim} depends on the detection efficiency ϵ, the number of ^{169}Tm nuclei N_{Tm}, the measurement time T, and axion resonant absorption rate R_A calculated in Section 7.3.2:

$$\epsilon \cdot N_{Tm} \cdot T \cdot R_A \leq S_{lim} \tag{7.15}$$

In case of $Tm_3Al_5O_{12}$ crystal the detection efficiency is $\epsilon \approx 1$ since the target material is located inside the active volume of the detector. The number of target ^{169}Tm nuclei in 8.18 g $Tm_3Al_5O_{12}$ crystal is $N_{Tm} = 1.77 \times 10^{22}$. The exposure time left after the application of data selection cuts is equal to $T = 3.86$ days and R_A is the axion resonant absorption rate for ^{169}Tm defined earlier by expressions (7.11, 7.12, 7.13). In accordance with these equations and in assumption that $(p_A/p_\gamma)^3 \approx 1$, which holds for axion masses below ~ 2 keV, our measurement yields the following limits on axion-photon coupling:

$$\begin{aligned} \left| g_{A\gamma} \cdot (g^0_{AN} + g^3_{AN}) \right| &\leq 1.44 \times 10^{-14}\,\mathrm{GeV}^{-1} \\ |g_{A\gamma} m_A| &\leq 2.31 \times 10^{-7} \end{aligned} \tag{7.16}$$

and axion-electron coupling:

$$\begin{aligned} \left| g_{Ae} \cdot (g^0_{AN} + g^3_{AN}) \right| &\leq 2.81 \times 10^{-16} \\ |g_{Ae} m_A| &\leq 4.59 \times 10^{-9}\,\mathrm{eV} \end{aligned} \tag{7.17}$$

The axion mass m_A here is expressed in eV units and $g_{A\gamma}$ is expressed in GeV^{-1} units, while g_{Ae} and g_{AN} are dimensionless.

The exclusion plots for the axion parameter space are given in Figures 7.4 and 7.5 along with comparison with other experiments and astrophysical bounds. The limit obtained in this work significantly exceeds the best previous result achieved with ^{169}Tm target [178]. The $g_{A\gamma}$ limit obtained with ^{83}Kr [143] still remains unsurpassed, although the current limits achieved with only 8.18 g crystal and 3.86 days of live time are competitive, and show potential due to the scalability of the experiment.

It should also be noted that the particular values of ^{169}Tm nuclear matrix elements make it a favorable axion target, since the probability ratio ω_A/ω_γ never vanishes for any combination of model parameters, unlike the case of ^{57}Fe and ^{83}Kr nuclei [141].

7.6 Conclusions

In this work we present the first successful investigation of the resonant absorption of solar axions in ^{169}Tm employing a cryogenic bolometer. The cryogenic bolometer is constituted by a 8.18 g $Tm_3Al_5O_{12}$ crystal with a TES directly evaporated on the crystal surface. We have collected data for 3.86 days of effective measurement time with a ^{169}Tm exposure equal to 19.2 g·day. From the data acquired, we set competitive limits on the axion coupling constants to electrons and photons.

The technology presented in this paper allows for a straightforward scaling of the experiment which would enable a drastic increase of the collected exposure. Furthermore, the reduction of the background rate in the region of interest would translate into a considerable improvement on the sensitivity to solar axion absorption. Since the background rate reduction can be effectively achieved with a dedicated underground experiment, we are confident in an improvement of the presented results in the near future.

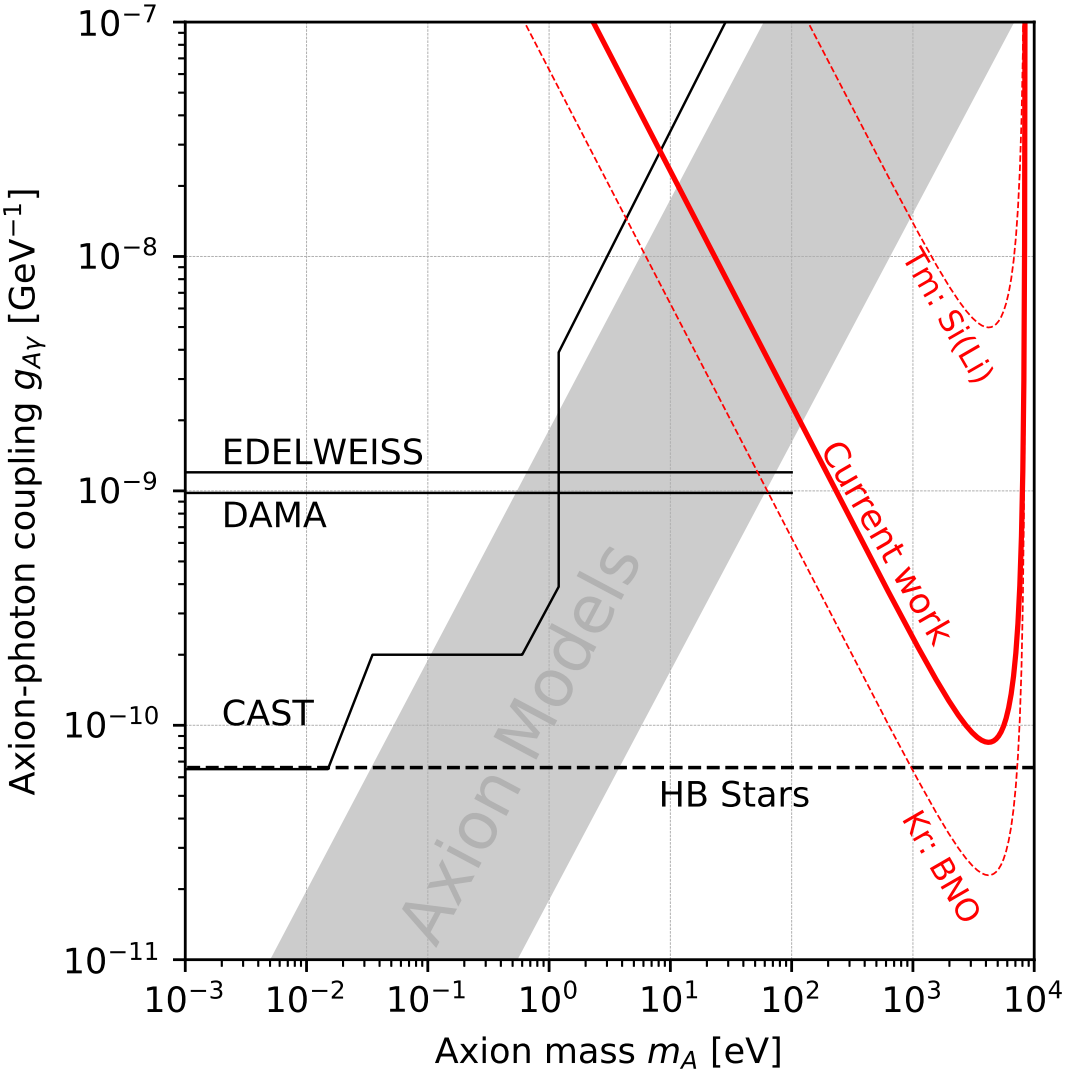

Figure 7.4: Axion-photon coupling $g_{A\gamma}$ limits obtained in current work in comparison with other experiments (DAMA [134], EDELWEISS [136], CAST [132], ^{169}Tm-Si(Li) [178], ^{83}Kr-gas counter [143]) and astrophysical bounds (horizontal branch stars lifetime [274]).

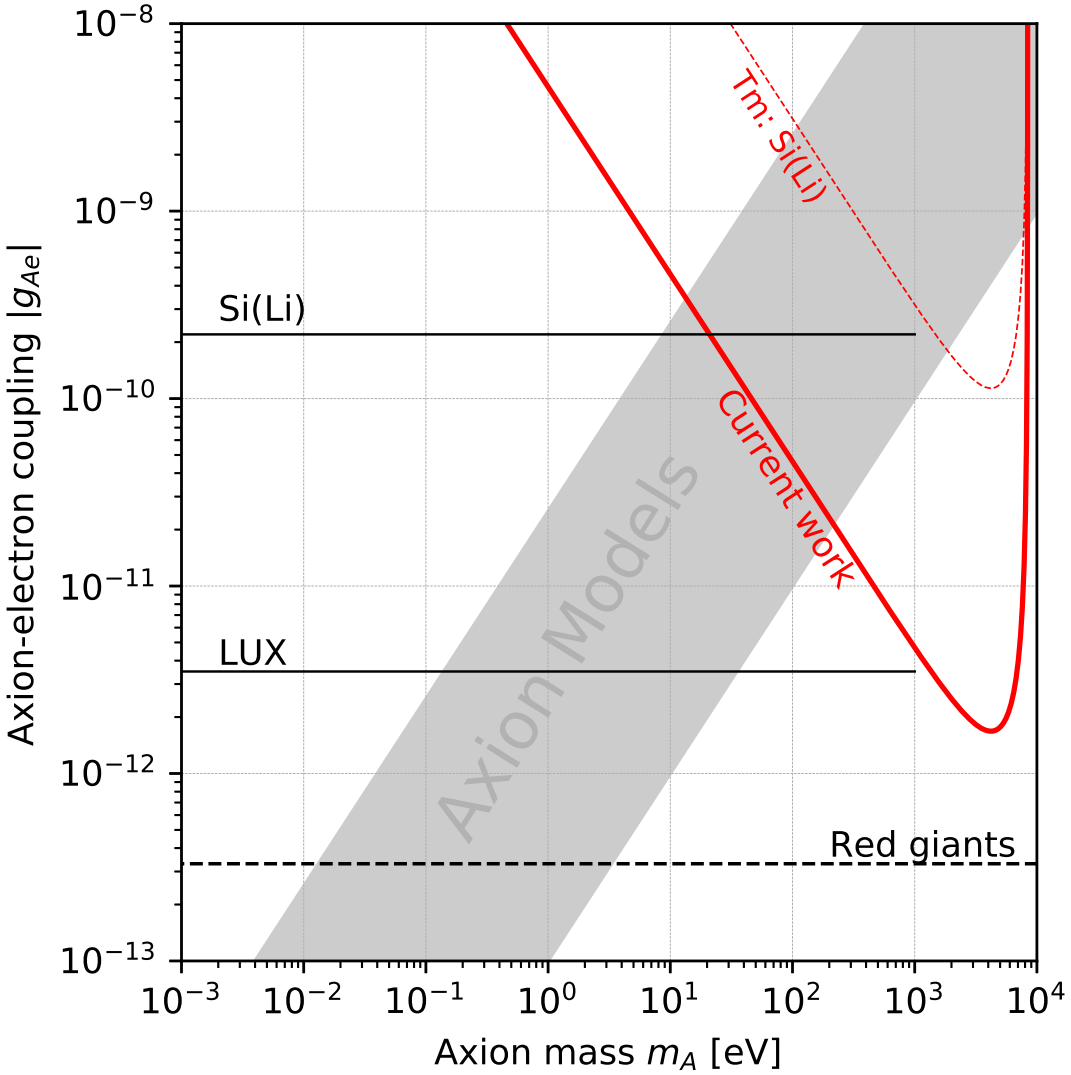

Figure 7.5: Axion-electron coupling g_{Ae} limits obtained in current work in comparison with other experiments (axio-electric effect on Si [137], LUX [275]) and astrophysical bounds (red giant cooling rate [276]).

Chapter 8

Conclusions and future perspectives

The work presented in this thesis shows that the cutting-edge technology developed over the years by the CRESST experiment can be used beyond what has been the main focus of the experiment in the past. In fact, CRESST-III is currently leading the exploration of spin-independent interactions between sub-GeV dark matter particles and ordinary matter among cryogenic experiments, but the physics reach can be further extended. For this reason, in this thesis two new distinct lines of research for the experiment were pursued by developing and testing novel prototypes at the Max Planck Institute for Physics in Munich, Germany.

The first goal was to expand the sub-GeV dark matter investigation to spin-dependent interactions with ordinary matter. As such, new types of absorbers were employed, focusing primarily on adopting the most sensitive isotope to explore this parameter space: ^{7}Li. ^{7}Li has all the attractive properties required: high sensitivity, high natural abundance (92.4%), light mass, and available in crystals suited for cryogenic experiments. Furthermore, lithium-containing crystals can also be employed to measure small neutron fluxes directly inside the experimental setup. Since neutrons are a dangerous background source for a dark matter experiment, this is an added bonus which might significantly improve the modeling of the experimental background.
The first prototype developed for this scope was based on a Li_2MoO_4 crystal and achieved a relatively low energy threshold (932 eV) even though the thermal sensor employed was not optimal and far from the usual performances of CRESST-like TESs. Nevertheless, the energy threshold achieved allowed to set competitive limits on spin-dependent dark matter interactions in the sub-GeV mass range despite the extremely low exposure (7.91×10^5 kg·days for ^{7}Li) and the operation in a non-shielded above-ground laboratory. The second stage of the detector development was aimed at building a detector with a lithium-containing crystal instrumented with a CRESST-like TES. To do so, it was required to change the target crystal, since the large higroscopicity of Li_2MoO_4 was an insurmountable obstacle to this implementation. The choice fell to $LiAlO_2$, a novel absorber for cryogenic experiments. As such, there was the need of a cryogenic characterization which was done with a 2.8g crystal instrumented with a NTD and coupled with a CRESST-III light detector. A twin crystal, the first of this kind instrumented with a TES, was simultaneously run and achieved a low energy threshold of (213.02±1.48) eV. The improvement in the energy threshold compared to the Li_2MoO_4 run allowed to significantly lower the limits on spin-dependent interactions, probing dark matter

masses as low as 0.35 GeV. The limit set on *proton-only* spin-dependent interactions is currently the leading one for cryogenic experiments in the sub-GeV mass range. Again, this was achieved despite the low exposure and a cryogenic operation in a non-shielded above-ground laboratory. Clearly, this indicates that significant improvements (∼4 orders of magnitude) of the previously-set dark matter limits can be achieved by simply acquiring data in an underground run. For this reason, CRESST-III is currently acquiring data with two detector modules based on $LiAlO_2$ and built in the same fashion as regular $CaWO_4$ modules at the Laboratori Nazionali del Gran Sasso (LNGS).Finally, a 373 g $LiAlO_2$ crystal was instrumented with both a TES and a NTD and operated in an underground facility at LNGS. The module was operated in the presence of a weak neutron source to test the possibility to tag neutron capture events by ^{6}Li, an isotope of lithium with a 7.6% natural abundance. This test gave positive indications towards the implementation of this technique for measuring the neutron background directly inside the CRESST cryostat.

The second line of research involved the adoption of CRESST-like TESs to investigate the resonant absorption of solar axions by ^{169}Tm. Solar axions have an energy spectrum of $\lesssim$15 keV. If one of these particles flows through a thulium-containing material it can be absorbed inducing the excitation of the nuclear state of ^{169}Tm. When the nucleus relaxes back from the first excited state to its ground state, a 8.41 keV photon is emitted. As such, there is an effective conversion to a non-detectable particle, the axion, to a detectable signature, a photon with a fixed energy. If the experiment is built with enough sensitivity and solar axions exist, a peak centered at 8.41 keV would appear in the energy spectrum. Some small scale experiments already tried to pursue this detection principle, but they were severely limited by their detection efficiency and their small exposure. This is mostly due to the fact that ^{169}Tm was not embedded in the detector. This problem can be efficiently solved by employing an array of cryogenic detectors with a ^{169}Tm-containing the absorber. For this reason, two prototypes based on a $Tm_3Al_5O_{12}$ crystal were developed and tested at Max Planck Institute for Physics.
The first prototype was instrumented with a NTD thermistor to study its cryogenic properties and in this run it was possible to acquire the first calibrated energy spectrum with a cryogenic detector containing ^{169}Tm. However, the energy threshold achieved (∼170 keV) was far from the experimental design, which requires E_T ≤8.41 keV After this, there was a development aimed at reaching the experimental design required to investigate solar axions. Since a drastic improvement of the energy threshold was needed, the second prototype was instrumented with an evaporated CRESST-like TES. This time the detector matched the required specifications and it was possible to acquire data for 3.86 days of effective measurement. This converts to an exposure of 19.2 g·days for ^{169}Tm. No excess of events was found in the vicinity of 8.41 keV, so the following limits on axion couplings were derived: $|g_{A\gamma}(g^0_{AN} + g^3_{AN})| \leq 1.44 \times 10^{-14}\,\mathrm{GeV}^{-1}$ and $|g_{Ae}(g^0_{AN} + g^3_{AN})| \leq 2.81 \times 10^{-16}$. The limit on $|g_{A\gamma}|$ is the strongest obtained for an experiment based on a ^{169}Tm-containing target, while the limit on $|g_{Ae}|$ is the most stringent among all the experiments for axion masses larger than 1 keV.
In this case too, the biggest limit is the operation of the detector in a non-shielded above-ground experiments. A similar underground experiment has the potential to surpass all the experimental limits on both couplings for axion masses larger than 1 keV and even challenge the astronomical bound even at lower masses.

Bibliography

[1] F. Zwicky. "Die Rotverschiebung von extragalaktischen Nebeln". In: *Helv. Phys. Acta* 6 (1933), pp. 110–127. DOI: 10.1007/s10714-008-0707-4.

[2] Gianfranco Bertone and Dan Hooper. "History of dark matter". In: *Rev. Mod. Phys.* 90.4 (2018), p. 045002. DOI: 10.1103/RevModPhys.90.045002. arXiv: 1605.04909 [astro-ph.CO].

[3] F. Zwicky. "On the Masses of Nebulae and of Clusters of Nebulae". In: *Astrophys. J.* 86 (1937), pp. 217–246. DOI: 10.1086/143864.

[4] Sinclair Smith. "The Mass of the Virgo Cluster". In: *Astrophys. J.* 83 (1936), pp. 23–30. DOI: 10.1086/143697.

[5] Vera C. Rubin and W. Kent Ford Jr. "Rotation of the Andromeda Nebula from a Spectroscopic Survey of Emission Regions". In: *Astrophys. J.* 159 (1970), pp. 379–403. DOI: 10.1086/150317.

[6] V. C. Rubin, N. Thonnard, and W. K. Ford Jr. "Rotational properties of 21 SC galaxies with a large range of luminosities and radii, from NGC 4605 /R = 4kpc/ to UGC 2885 /R = 122 kpc/". In: *Astrophys. J.* 238 (1980), p. 471. DOI: 10.1086/158003.

[7] S. M. Faber and J. S. Gallagher. "Masses and mass-to-light ratios of galaxies". In: *Annual Review of Astron and Astrophys* 17 (1979), pp. 135–187. DOI: 10.1146/annurev.aa.17.090179.001031.

[8] A. S. Szalay and G. Marx. "Neutrino rest mass from cosmology". In: *Astronomy and Astrophysics* 49 (June 1976), pp. 437–441.

[9] J. E. Gunn et al. "Some Astrophysical Consequences of the Existence of a Heavy Stable Neutral Lepton". In: *Astrophys. J.* 223 (1978). [,190(1978)], pp. 1015–1031. DOI: 10.1086/156335.

[10] S. S. Gershtein and Ya. B. Zeldovich. "Rest Mass of Muonic Neutrino and Cosmology". In: *JETP Lett.* 4 (1966). [,58(1966)], pp. 120–122.

[11] R. Cowsik and J. McClelland. "An Upper Limit on the Neutrino Rest Mass". In: *Phys. Rev. Lett.* 29 (1972), pp. 669–670. DOI: 10.1103/PhysRevLett.29.669.

[12] M. I. Vysotsky, A. D. Dolgov, and Ya. B. Zeldovich. "Cosmological Restriction on Neutral Lepton Masses". In: *JETP Lett.* 26 (1977). [,187(1977)], pp. 188–190.

[13] Katsuhiko Sato and Makoto Kobayashi. "Cosmological Constraints on the Mass and the Number of Heavy Lepton Neutrinos". In: *Progress of Theoretical Physics* 58.6 (Dec. 1977), pp. 1775–1789. ISSN: 0033-068X. DOI: 10.1143/PTP.58.1775. eprint: http://oup.prod.sis.lan/ptp/article-pdf/58/6/1775/5295104/58-6-1775.pdf. URL: https://dx.doi.org/10.1143/PTP.58.1775.

[14] Benjamin W. Lee and Steven Weinberg. "Cosmological Lower Bound on Heavy Neutrino Masses". In: *Phys. Rev. Lett.* 39 (1977). [,183(1977)], pp. 165–168. DOI: 10.1103/PhysRevLett.39.165.

[15] P. Hut. "Limits on Masses and Number of Neutral Weakly Interacting Particles". In: *Phys. Lett.* B69 (1977). [,179(1977)], p. 85. DOI: 10.1016/0370-2693(77)90139-3.

[16] Duane A. Dicus, Edward W. Kolb, and Vigdor L. Teplitz. "Cosmological Upper Bound on Heavy Neutrino Lifetimes". In: *Phys. Rev. Lett.* 39 (1977). [Erratum: Phys. Rev. Lett.39,973(1977)], p. 168. DOI: 10.1103/PhysRevLett.39.973.2,10.1103/PhysRevLett.39.168.

[17] A. G. Doroshkevich et al. "Astrophysical implications of the neutrino rest mass. III. Nonlinear growth of perturbations and the missing mass". In: *Sov. Astron. Lett.* 6 (1980). [Pisma Astron. Zh.6,465(1980)], pp. 257–259.

[18] V. A. Lyubimov et al. "An Estimate of the electron-Neutrino Mass from the beta Spectrum of Tritium in the Valine Molecule". In: *Phys. Lett.* 94B (1980), pp. 266–268. DOI: 10.1016/0370-2693(80)90873-4.

[19] Simon D. M. White, C. S. Frenk, and M. Davis. "Clustering in a Neutrino Dominated Universe". In: *Astrophys. J.* 274 (1983). [,80(1984)], pp. L1–L5. DOI: 10.1086/161425.

[20] Heinz Pagels and Joel R. Primack. "Supersymmetry, Cosmology and New TeV Physics". In: *Phys. Rev. Lett.* 48 (1982), p. 223. DOI: 10.1103/PhysRevLett.48.223.

[21] Scott Dodelson and Lawrence M. Widrow. "Sterile-neutrinos as dark matter". In: *Phys. Rev. Lett.* 72 (1994), pp. 17–20. DOI: 10.1103/PhysRevLett.72.17. arXiv: hep-ph/9303287 [hep-ph].

[22] Savas Dimopoulos and Howard Georgi. "Softly Broken Supersymmetry and SU(5)". In: *Nucl. Phys.* B193 (1981), pp. 150–162. DOI: 10.1016/0550-3213(81)90522-8.

[23] R. D. Peccei and Helen R. Quinn. "CP Conservation in the Presence of Instantons". In: *Phys. Rev. Lett.* 38 (1977), pp. 1440–1443. DOI: 10.1103/PhysRevLett.38.1440.

[24] R. D. Peccei and Helen R. Quinn. "Constraints Imposed by CP Conservation in the Presence of Instantons". In: *Phys. Rev.* D16 (1977), pp. 1791–1797. DOI: 10.1103/PhysRevD.16.1791.

[25] Frank Wilczek. "Problem of Strong P and T Invariance in the Presence of Instantons". In: *Phys. Rev. Lett.* 40 (1978), pp. 279–282. DOI: 10.1103/PhysRevLett.40.279.

[26] Steven Weinberg. "A New Light Boson?" In: *Phys. Rev. Lett.* 40 (1978), pp. 223–226. DOI: 10.1103/PhysRevLett.40.223.

[27] Bernard Carr, Florian Kuhnel, and Marit Sandstad. "Primordial Black Holes as Dark Matter". In: *Phys. Rev.* D94.8 (2016), p. 083504. DOI: 10.1103/PhysRevD.94.083504. arXiv: 1607.06077 [astro-ph.CO].

[28] Anne M. Green and Bradley J. Kavanagh. "Primordial Black Holes as a dark matter candidate". In: (2020). arXiv: 2007.10722 [astro-ph.CO].

[29] M. Milgrom. "A Modification of the Newtonian dynamics as a possible alternative to the hidden mass hypothesis". In: *Astrophys. J.* 270 (1983), pp. 365–370. DOI: 10.1086/161130.

[30] Georges Lemaitre. "A Homogeneous Universe of Constant Mass and Growing Radius Accounting for the Radial Velocity of Extragalactic Nebulae". In: *Annales Soc. Sci. Bruxelles A* 47 (1927). [Gen. Rel. Grav.45,no.8,1635(2013)], pp. 49–59. DOI: 10.1007/s10714-013-1548-3.

[31] G. Lemaitre. "The expanding universe". In: *Gen. Rel. Grav.* 29 (1997). [Annales Soc. Sci. Bruxelles A53,51(1933)], pp. 641–680. DOI: 10.1023/A:1018855621348.

[32] G. Gamow. "The Evolution of the Universe". In: *Nature* 162.4122 (1948), pp. 680–682. DOI: 10.1038/162680a0.

[33] R. A. Alpher, H. Bethe, and G. Gamow. "The origin of chemical elements". In: *Phys. Rev.* 73 (1948), pp. 803–804. DOI: 10.1103/PhysRev.73.803.

[34] Alan H. Guth. "The Inflationary Universe: A Possible Solution to the Horizon and Flatness Problems". In: *Phys. Rev.* D23 (1981). [Adv. Ser. Astrophys. Cosmol.3,139(1987)], pp. 347–356. DOI: 10.1103/PhysRevD.23.347.

[35] N. Aghanim et al. "Planck 2018 results. VI. Cosmological parameters". In: (2018). arXiv: 1807.06209 [astro-ph.CO].

[36] M. Tanabashi et al. "Review of Particle Physics". In: *Phys. Rev. D* 98 (3 Aug. 2018), p. 030001. DOI: 10.1103/PhysRevD.98.030001. URL: https://link.aps.org/doi/10.1103/PhysRevD.98.030001.

[37] Tongyan Lin. "Dark matter models and direct detection". In: *PoS* 333 (2019), p. 009. DOI: 10.22323/1.333.0009. arXiv: 1904.07915 [hep-ph].

[38] M. Markevitch et al. "A Textbook example of a bow shock in the merging galaxy cluster 1E0657-56". In: *Astrophys. J. Lett.* 567 (2002), p. L27. DOI: 10.1086/339619. arXiv: astro-ph/0110468 [astro-ph].

[39] Maxim Markevitch et al. "Direct constraints on the dark matter self-interaction cross-section from the merging galaxy cluster 1E0657-56". In: *Astrophys. J.* 606 (2004), pp. 819–824. DOI: 10.1086/383178. arXiv: astro-ph/0309303 [astro-ph].

[40] M. Viel, J. S. Bolton, and M. G. Haehnelt. "Cosmological and astrophysical constraints from the Lyman-alpha forest flux probability distribution function". In: *Mon. Not. Roy. Astron. Soc.* 399 (2009), pp. L39–L43. DOI: 10.1111/j.1745-3933.2009.00720.x. arXiv: 0907.2927 [astro-ph.CO].

[41] Douglas Clowe et al. "A direct empirical proof of the existence of dark matter". In: *Astrophys. J. Lett.* 648 (2006), pp. L109–L113. DOI: 10.1086/508162. arXiv: astro-ph/0608407 [astro-ph].

[42] Priyamvada Natarajan et al. "Mapping substructure in the HST Frontier Fields cluster lenses and in cosmological simulations". In: *Mon. Not. Roy. Astron. Soc.* 468.2 (2017), pp. 1962–1980. DOI: 10.1093/mnras/stw3385. arXiv: 1702.04348 [astro-ph.GA].

[43] Arno A. Penzias and Robert Woodrow Wilson. "A Measurement of excess antenna temperature at 4080-Mc/s". In: *Astrophys. J.* 142 (1965), pp. 419–421. DOI: 10.1086/148307.

[44] Daniel Baumann. "Primordial Cosmology". In: *PoS* TASI2017 (2018), p. 009. DOI: 10.22323/1.305.0009. arXiv: 1807.03098 [hep-th].

[45] C. L. Bennett et al. "Four year COBE DMR cosmic microwave background observations: Maps and basic results". In: *Astrophys. J. Lett.* 464 (1996), pp. L1–L4. DOI: 10.1086/310075. arXiv: astro-ph/9601067 [astro-ph].

[46] C. L. Bennett et al. "Nine-Year Wilkinson Microwave Anisotropy Probe (WMAP) Observations: Final Maps and Results". In: *Astrophys. J. Suppl.* 208 (2013), p. 20. DOI: 10.1088/0067-0049/208/2/20. arXiv: 1212.5225 [astro-ph.CO].

[47] D. J. Fixsen. "The Temperature of the Cosmic Microwave Background". In: *Astrophys. J.* 707 (2009), pp. 916–920. DOI: 10.1088/0004-637X/707/2/916. arXiv: 0911.1955 [astro-ph.CO].

[48] Y. Akrami et al. "Planck 2018 results. I. Overview and the cosmological legacy of Planck". In: (2018). arXiv: 1807.06205 [astro-ph.CO].

[49] Daniel J. Eisenstein et al. "Detection of the Baryon Acoustic Peak in the Large-Scale Correlation Function of SDSS Luminous Red Galaxies". In: *Astrophys. J.* 633 (2005), pp. 560–574. DOI: 10.1086/466512. arXiv: astro-ph/0501171 [astro-ph].

[50] Lauren Anderson et al. "The clustering of galaxies in the SDSS-III Baryon Oscillation Spectroscopic Survey: baryon acoustic oscillations in the Data Releases 10 and 11 Galaxy samples". In: *Mon. Not. Roy. Astron. Soc.* 441.1 (2014), pp. 24–62. DOI: 10.1093/mnras/stu523. arXiv: 1312.4877 [astro-ph.CO].

[51] Risa H. Wechsler and Jeremy L. Tinker. "The Connection between Galaxies and their Dark Matter Halos". In: *Ann. Rev. Astron. Astrophys.* 56 (2018), pp. 435–487. DOI: 10.1146/annurev-astro-081817-051756. arXiv: 1804.03097 [astro-ph.GA].

[52] Mark Vogelsberger et al. "Cosmological Simulations of Galaxy Formation". In: *Nature Rev. Phys.* 2.1 (2020), pp. 42–66. DOI: 10.1038/s42254-019-0127-2. arXiv: 1909.07976 [astro-ph.GA].

[53] Richard H. Cyburt, Brian D. Fields, and Keith A. Olive. "An Update on the big bang nucleosynthesis prediction for Li-7: The problem worsens". In: *JCAP* 11 (2008), p. 012. DOI: 10.1088/1475-7516/2008/11/012. arXiv: 0808.2818 [astro-ph].

[54] Massimo Persic, Paolo Salucci, and Fulvio Stel. "The Universal rotation curve of spiral galaxies: 1. The Dark matter connection". In: *Mon. Not. Roy. Astron. Soc.* 281 (1996), p. 27. DOI: 10.1093/mnras/281.1.27,10.1093/mnras/278.1.27. arXiv: astro-ph/9506004 [astro-ph].

[55] Jonathan L. Feng. "Dark Matter Candidates from Particle Physics and Methods of Detection". In: *Ann. Rev. Astron. Astrophys.* 48 (2010), pp. 495–545. DOI: 10.1146/annurev-astro-082708-101659. arXiv: 1003.0904 [astro-ph.CO].

[56] Gianfranco Bertone and M. P. Tait Tim. "A new era in the search for dark matter". In: *Nature* 562.7725 (2018), pp. 51–56. DOI: 10.1038/s41586-018-0542-z. arXiv: 1810.01668 [astro-ph.CO].

[57] Jonathan L. Feng and Jason Kumar. "The WIMPless Miracle: Dark-Matter Particles without Weak-Scale Masses or Weak Interactions". In: *Phys. Rev. Lett.* 101 (2008), p. 231301. DOI: 10.1103/PhysRevLett.101.231301. arXiv: 0803.4196 [hep-ph].

[58] Giorgio Arcadi et al. "The waning of the WIMP? A review of models, searches, and constraints". In: *Eur. Phys. J.* C78.3 (2018), p. 203. DOI: 10.1140/epjc/s10052-018-5662-y. arXiv: 1703.07364 [hep-ph].

[59] Simon Knapen, Tongyan Lin, and Kathryn M. Zurek. "Light Dark Matter: Models and Constraints". In: *Phys. Rev.* D96.11 (2017), p. 115021. DOI: 10.1103/PhysRevD.96.115021. arXiv: 1709.07882 [hep-ph].

[60] Yonit Hochberg et al. "Mechanism for Thermal Relic Dark Matter of Strongly Interacting Massive Particles". In: *Phys. Rev. Lett.* 113 (2014), p. 171301. DOI: 10.1103/PhysRevLett.113.171301. arXiv: 1402.5143 [hep-ph].

[61] David E. Kaplan, Markus A. Luty, and Kathryn M. Zurek. "Asymmetric Dark Matter". In: *Physical Review D* 79 (2009), p. 115016. DOI: 10.1103/PhysRevD.79.115016. arXiv: 0901.4117.

[62] Kathryn M. Zurek. "Asymmetric Dark Matter: Theories, Signatures, and Constraints". In: *Phys. Rept.* 537 (2014), pp. 91–121. DOI: 10.1016/j.physrep.2013.12.001. arXiv: 1308.0338 [hep-ph].

[63] Kalliopi Petraki and Raymond R. Volkas. "Review of asymmetric dark matter". In: *Int. J. Mod. Phys.* A28 (2013), p. 1330028. DOI: 10.1142/S0217751X13300287. arXiv: 1305.4939 [hep-ph].

[64] John Preskill, Mark B. Wise, and Frank Wilczek. "Cosmology of the Invisible Axion". In: *Phys. Lett.* 120B (1983), pp. 127–132. DOI: 10.1016/0370-2693(83)90637-8.

[65] David J. E. Marsh. "Axion Cosmology". In: *Phys. Rept.* 643 (2016), pp. 1–79. DOI: 10.1016/j.physrep.2016.06.005. arXiv: 1510.07633 [astro-ph.CO].

[66] Jihn E. Kim and Gianpaolo Carosi. "Axions and the Strong CP Problem". In: *Rev. Mod. Phys.* 82 (2010). [Erratum: Rev. Mod. Phys.91,no.4,049902(2019)], pp. 557–602. DOI: 10.1103/RevModPhys.91.049902,10.1103/RevModPhys.82.557. arXiv: 0807.3125 [hep-ph].

[67] R. D. Peccei. "The Strong CP problem and axions". In: *Lect. Notes Phys.* 741 (2008), pp. 3–17. DOI: 10.1007/978-3-540-73518-2_1. arXiv: hep-ph/0607268 [hep-ph].

[68] Joerg Jaeckel and Andreas Ringwald. "The Low-Energy Frontier of Particle Physics". In: *Ann. Rev. Nucl. Part. Sci.* 60 (2010), pp. 405–437. DOI: 10.1146/annurev.nucl.012809.104433. arXiv: 1002.0329 [hep-ph].

[69] Howard Baer et al. "Dark matter production in the early Universe: beyond the thermal WIMP paradigm". In: *Phys. Rept.* 555 (2015), pp. 1–60. DOI: 10.1016/j.physrep.2014.10.002. arXiv: 1407.0017 [hep-ph].

[70] P. A. Zyla et al. "Review of Particle Physics". In: *PTEP* 2020.8 (2020), p. 083C01. DOI: 10.1093/ptep/ptaa104.

[71] Alexander Kusenko. "Sterile neutrinos: The Dark side of the light fermions". In: *Phys. Rept.* 481 (2009), pp. 1–28. DOI: 10.1016/j.physrep.2009.07.004. arXiv: 0906.2968 [hep-ph].

[72] Yohei Ema, Kazunori Nakayama, and Yong Tang. "Production of Purely Gravitational Dark Matter". In: *JHEP* 09 (2018), p. 135. DOI: 10.1007/JHEP09(2018)135. arXiv: 1804.07471 [hep-ph].

[73] Jonathan L. Feng, Arvind Rajaraman, and Fumihiro Takayama. "Probing gravitational interactions of elementary particles". In: *Int. J. Mod. Phys.* D13 (2004). [Gen. Rel. Grav.36,2575(2004)], pp. 2355–2359. DOI: 10.1142/S0218271804006474,10.1023/B:GERG.0000048977.62657.41. arXiv: hep-th/0405248 [hep-th].

[74] Lars Bergstrom. "Dark Matter Evidence, Particle Physics Candidates and Detection Methods". In: *Annalen Phys.* 524 (2012), pp. 479–496. DOI: 10.1002/andp.201200116. arXiv: 1205.4882 [astro-ph.HE].

[75] Gianfranco Bertone, Dan Hooper, and Joseph Silk. "Particle dark matter: Evidence, candidates and constraints". In: *Phys. Rept.* 405 (2005), pp. 279–390. DOI: 10.1016/j.physrep.2004.08.031. arXiv: hep-ph/0404175 [hep-ph].

[76] Michael Klasen, Martin Pohl, and Günter Sigl. "Indirect and direct search for dark matter". In: *Prog. Part. Nucl. Phys.* 85 (2015), pp. 1–32. DOI: 10.1016/j.ppnp.2015.07.001. arXiv: 1507.03800 [hep-ph].

[77] M. Ackermann et al. "Searching for Dark Matter Annihilation from Milky Way Dwarf Spheroidal Galaxies with Six Years of Fermi Large Area Telescope Data". In: *Phys. Rev. Lett.* 115.23 (2015), p. 231301. DOI: 10.1103/PhysRevLett.115.231301. arXiv: 1503.02641 [astro-ph.HE].

[78] W. B. Atwood et al. "The Large Area Telescope on the Fermi Gamma-ray Space Telescope Mission". In: *Astrophys. J.* 697 (2009), pp. 1071–1102. DOI: 10.1088/0004-637X/697/2/1071. arXiv: 0902.1089 [astro-ph.IM].

[79] J. A. Hinton. "The Status of the H.E.S.S. project". In: *New Astron. Rev.* 48 (2004), pp. 331–337. DOI: 10.1016/j.newar.2003.12.004. arXiv: astro-ph/0403052 [astro-ph].

[80] T. C. Weekes et al. "VERITAS: The Very energetic radiation imaging telescope array system". In: *Astropart. Phys.* 17 (2002), pp. 221–243. DOI: 10.1016/S0927-6505(01)00152-9. arXiv: astro-ph/0108478 [astro-ph].

[81] E. Lorenz. "Status of the 17-m MAGIC telescope". In: *New Astron. Rev.* 48 (2004), pp. 339–344. DOI: 10.1016/j.newar.2003.12.059.

[82] Tracy R. Slatyer. "Indirect Detection of Dark Matter". In: *Theoretical Advanced Study Institute in Elementary Particle Physics: Anticipating the Next Discoveries in Particle Physics*. 2018, pp. 297–353. DOI: 10.1142/9789813233348_0005. arXiv: 1710.05137 [hep-ph].

[83] M. Aguilar et al. "First Result from the Alpha Magnetic Spectrometer on the International Space Station: Precision Measurement of the Positron Fraction in Primary Cosmic Rays of 0.5–350 GeV". In: *Phys. Rev. Lett.* 110 (2013), p. 141102. DOI: 10.1103/PhysRevLett.110.141102.

[84] M. G. Aartsen et al. "Search for dark matter annihilations in the Sun with the 79-string IceCube detector". In: *Phys. Rev. Lett.* 110.13 (2013), p. 131302. DOI: 10.1103/PhysRevLett.110.131302. arXiv: 1212.4097 [astro-ph.HE].

[85] K. Choi et al. "Search for neutrinos from annihilation of captured low-mass dark matter particles in the Sun by Super-Kamiokande". In: *Phys. Rev. Lett.* 114.14 (2015), p. 141301. DOI: 10.1103/PhysRevLett.114.141301. arXiv: 1503.04858 [hep-ex].

[86] Mark W. Goodman and Edward Witten. "Detectability of Certain Dark Matter Candidates". In: *Phys. Rev.* D31 (1985), p. 3059. DOI: 10.1103/PhysRevD.31.3059.

[87] A. Drukier and Leo Stodolsky. "Principles and Applications of a Neutral Current Detector for Neutrino Physics and Astronomy". In: *Phys. Rev.* D30 (1984), p. 2295. DOI: 10.1103/PhysRevD.30.2295.

[88] URL: https://cpb-us-w2.wpmucdn.com/sites.brown.edu/dist/7/57/files/2019/10/Screenshot-from-2019-10-22-17-11-47.png.

[89] Martin C. Smith et al. "The RAVE Survey: Constraining the Local Galactic Escape Speed". In: *Mon. Not. Roy. Astron. Soc.* 379 (2007), pp. 755–772. DOI: 10.1111/j.1365-2966.2007.11964.x. arXiv: astro-ph/0611671 [astro-ph].

[90] Marc Schumann. "Direct Detection of WIMP Dark Matter: Concepts and Status". In: *J. Phys.* G46.10 (2019), p. 103003. DOI: 10.1088/1361-6471/ab2ea5. arXiv: 1903.03026 [astro-ph.CO].

[91] P. Salucci et al. "The dark matter density at the Sun's location". In: *Astron. Astrophys.* 523 (2010), A83. DOI: 10.1051/0004-6361/201014385. arXiv: 1003.3101 [astro-ph.GA].

[92] Asantha Cooray and Ravi K. Sheth. "Halo Models of Large Scale Structure". In: *Phys. Rept.* 372 (2002), pp. 1–129. DOI: 10.1016/S0370-1573(02)00276-4. arXiv: astro-ph/0206508 [astro-ph].

[93] G. Angloher et al. "Limits on Dark Matter Effective Field Theory Parameters with CRESST-II". In: *Eur. Phys. J.* C79.1 (2019), p. 43. DOI: 10.1140/epjc/s10052-018-6523-4. arXiv: 1809.03753 [hep-ph].

[94] Mariangela Lisanti. "Lectures on Dark Matter Physics". In: *Proceedings, Theoretical Advanced Study Institute in Elementary Particle Physics: New Frontiers in Fields and Strings (TASI 2015): Boulder, CO, USA, June 1-26, 2015*. 2017, pp. 399–446. DOI: 10.1142/9789813149441_0007. arXiv: 1603.03797 [hep-ph].

[95] V. A. Bednyakov and F. Simkovic. "Nuclear spin structure in dark matter search: The Finite momentum transfer limit". In: *Phys. Part. Nucl.* 37 (2006), S106–S128. DOI: 10.1134/S1063779606070057. arXiv: hep-ph/0608097 [hep-ph].

[96] P. Klos et al. "Large-scale nuclear structure calculations for spin-dependent WIMP scattering with chiral effective field theory currents". In: *Phys. Rev.* D88.8 (2013). [Erratum: Phys. Rev.D89,no.2,029901(2014)], p. 083516. DOI: 10.1103/PhysRevD.89.029901,10.1103/PhysRevD.88.083516. arXiv: 1304.7684 [nucl-th].

[97] Gerard Jungman, Marc Kamionkowski, and Kim Griest. "Supersymmetric dark matter". In: *Phys. Rept.* 267 (1996), pp. 195–373. DOI: 10.1016/0370-1573(95)00058-5. arXiv: hep-ph/9506380 [hep-ph].

[98] J. Engel, S. Pittel, and P. Vogel. "Nuclear physics of dark matter detection". In: *International Journal of Modern Physics E* 1 (1992), pp. 1–37. DOI: 10.1142/S0218301392000023.

[99] V. A. Bednyakov and F. Simkovic. "Nuclear spin structure in dark matter search: The Zero momentum transfer limit". In: *Phys. Part. Nucl.* 36 (2005). [Fiz. Elem. Chast. Atom. Yadra36,257(2005)], pp. 131–152. arXiv: hep-ph/0406218 [hep-ph].

[100] Timothy Cohen, Daniel J. Phalen, and Aaron Pierce. "On the Correlation Between the Spin-Independent and Spin-Dependent Direct Detection of Dark Matter". In: *Phys. Rev.* D81 (2010), p. 116001. DOI: 10.1103/PhysRevD.81.116001. arXiv: 1001.3408 [hep-ph].

[101] Marat Freytsis and Zoltan Ligeti. "On dark matter models with uniquely spin-dependent detection possibilities". In: *Phys. Rev.* D83 (2011), p. 115009. DOI: 10.1103/PhysRevD.83.115009. arXiv: 1012.5317 [hep-ph].

[102] Samuel K. Lee et al. "Effect of Gravitational Focusing on Annual Modulation in Dark-Matter Direct-Detection Experiments". In: *Phys. Rev. Lett.* 112.1 (2014), p. 011301. DOI: 10.1103/PhysRevLett.112.011301. arXiv: 1308.1953 [astro-ph.CO].

[103] R. Bernabei et al. "First model independent results from DAMA/LIBRA-phase2". In: *Nucl. Phys. Atom. Energy* 19.4 (2018), pp. 307–325. DOI: 10.15407/jnpae2018.04.307. arXiv: 1805.10486 [hep-ex].

[104] Gaurav Tomar et al. "Is a WIMP explanation of the DAMA modulation effect still viable?" In: *J. Phys. Conf. Ser.* 1468.1 (2020), p. 012015. DOI: 10.1088/1742-6596/1468/1/012015. arXiv: 1911.12601 [hep-ph].

[105] URL: https://www.nap.edu/resource/13204/deps_063545.pdf.

[106] V. Chepel and H. Araujo. "Liquid noble gas detectors for low energy particle physics". In: *JINST* 8 (2013), R04001. DOI: 10.1088/1748-0221/8/04/R04001. arXiv: 1207.2292 [physics.ins-det].

[107] C. E. Aalseth et al. "DarkSide-20k: A 20 tonne two-phase LAr TPC for direct dark matter detection at LNGS". In: *Eur. Phys. J. Plus* 133 (2018), p. 131. DOI: 10.1140/epjp/i2018-11973-4. arXiv: 1707.08145 [physics.ins-det].

[108] C. E. Aalseth et al. "Cryogenic Characterization of FBK RGB-HD SiPMs". In: *JINST* 12.09 (2017), P09030. DOI: 10.1088/1748-0221/12/09/P09030. arXiv: 1705.07028 [physics.ins-det].

[109] K. Abe et al. "XMASS detector". In: *Nucl. Instrum. Meth.* A716 (2013), pp. 78–85. DOI: 10.1016/j.nima.2013.03.059. arXiv: 1301.2815 [physics.ins-det].

[110] P. -A. Amaudruz et al. "Design and Construction of the DEAP-3600 Dark Matter Detector". In: *Astropart. Phys.* 108 (2019), pp. 1–23. DOI: 10.1016/j.astropartphys.2018.09.006. arXiv: 1712.01982 [astro-ph.IM].

[111] XiGuang Cao et al. "PandaX: A Liquid Xenon Dark Matter Experiment at CJPL". In: *Sci. China Phys. Mech. Astron.* 57 (2014), pp. 1476–1494. DOI: 10.1007/s11433-014-5521-2. arXiv: 1405.2882 [physics.ins-det].

[112] E. Aprile et al. "The XENON1T Dark Matter Experiment". In: *Eur. Phys. J.* C77.12 (2017), p. 881. DOI: 10.1140/epjc/s10052-017-5326-3. arXiv: 1708.07051 [astro-ph.IM].

[113] D. S. Akerib et al. "The Large Underground Xenon (LUX) Experiment". In: *Nucl. Instrum. Meth.* A704 (2013), pp. 111–126. DOI: 10.1016/j.nima.2012.11.135. arXiv: 1211.3788 [physics.ins-det].

[114] M. Bossa. "DarkSide-50, a background free experiment for dark matter searches". In: *JINST* 9 (2014), p. C01034. DOI: 10.1088/1748-0221/9/01/C01034.

[115] F. Aubin et al. "Discrimination of nuclear recoils from alpha particles with superheated liquids". In: *New J. Phys.* 10 (2008), p. 103017. DOI: 10.1088/1367-2630/10/10/103017. arXiv: 0807.1536 [physics.ins-det].

[116] C. Amole et al. "Dark Matter Search Results from the Complete Exposure of the PICO-60 C_3F_8 Bubble Chamber". In: *Phys. Rev.* D100.2 (2019), p. 022001. DOI: 10.1103/PhysRevD.100.022001. arXiv: 1902.04031 [astro-ph.CO].

[117] Q. Arnaud et al. "Spherical Proportional Counter: A review of recent developments". In: *J. Phys. Conf. Ser.* 1029.1 (2018), p. 012006. DOI: 10.1088/1742-6596/1029/1/012006.

[118] Q. Arnaud et al. "First results from the NEWS-G direct dark matter search experiment at the LSM". In: *Astropart. Phys.* 97 (2018), pp. 54–62. DOI: 10.1016/j.astropartphys.2017.10.009. arXiv: 1706.04934 [astro-ph.IM].

[119] A. Brossard. "Spherical proportional counters; development, improvement and understanding". In: *Nucl. Instrum. Meth.* A936 (2019), pp. 412–415. DOI: 10.1016/j.nima.2018.11.037.

[120] R. Agnese et al. "Projected Sensitivity of the SuperCDMS SNOLAB experiment". In: *Phys. Rev.* D95.8 (2017), p. 082002. DOI: 10.1103/PhysRevD.95.082002. arXiv: 1610.00006 [physics.ins-det].

[121] E. Armengaud et al. "A search for low-mass WIMPs with EDELWEISS-II heat-and-ionization detectors". In: *Phys. Rev.* D86 (2012), p. 051701. DOI: 10.1103/PhysRevD.86.051701. arXiv: 1207.1815 [astro-ph.CO].

[122] A. H. Abdelhameed et al. "First results from the CRESST-III low-mass dark matter program". In: *Phys. Rev.* D100.10 (2019), p. 102002. DOI: 10.1103/PhysRevD.100.102002. arXiv: 1904.00498 [astro-ph.CO].

[123] Stephen J. Asztalos et al. "Searches for astrophysical and cosmological axions". In: *Ann. Rev. Nucl. Part. Sci.* 56 (2006), pp. 293–326. DOI: 10.1146/annurev.nucl.56.080805.140513.

[124] Klaus Ehret et al. "New ALPS Results on Hidden-Sector Lightweights". In: *Phys. Lett.* B689 (2010), pp. 149–155. DOI: 10.1016/j.physletb.2010.04.066. arXiv: 1004.1313 [hep-ex].

[125] Jason H. Steffen and Amol Upadhye. "The GammeV suite of experimental searches for axion-like particles". In: *Mod. Phys. Lett.* A24 (2009), pp. 2053–2068. DOI: 10.1142/S0217732309031727. arXiv: 0908.1529 [hep-ex].

[126] Federico Della Valle et al. "The PVLAS experiment: measuring vacuum magnetic birefringence and dichroism with a birefringent Fabry–Perot cavity". In: *Eur. Phys. J.* C76.1 (2016), p. 24. DOI: 10.1140/epjc/s10052-015-3869-8. arXiv: 1510.08052 [physics.optics].

[127] Peter W. Graham et al. "Experimental Searches for the Axion and Axion-Like Particles". In: *Ann. Rev. Nucl. Part. Sci.* 65 (2015), pp. 485–514. DOI: 10.1146/annurev-nucl-102014-022120. arXiv: 1602.00039 [hep-ex].

[128] Javier Redondo. "Solar axion flux from the axion-electron coupling". In: *JCAP* 1312 (2013), p. 008. DOI: 10.1088/1475-7516/2013/12/008. arXiv: 1310.0823 [hep-ph].

[129] W. C. Haxton and K. Y. Lee. "Red giant evolution, metallicity and new bounds on hadronic axions". In: *Phys. Rev. Lett.* 66 (1991), pp. 2557–2560. DOI: 10.1103/PhysRevLett.66.2557.

[130] M. Krcmar et al. "Search for solar axions using Li-7". In: *Phys. Rev.* D64 (2001), p. 115016. DOI: 10.1103/PhysRevD.64.115016. arXiv: hep-ex/0104035 [hep-ex].

[131] K. Jakovcic et al. "A Search for solar hadronic axions using ^{83}Kr". In: *Radiat. Phys. Chem.* 71 (2004), pp. 793–794. DOI: 10.1016/j.radphyschem.2004.04.095. arXiv: nucl-ex/0402016 [nucl-ex].

[132] V. Anastassopoulos et al. "New CAST Limit on the Axion-Photon Interaction". In: *Nature Phys.* 13 (2017), pp. 584–590. DOI: 10.1038/nphys4109. arXiv: 1705.02290 [hep-ex].

[133] F. T. Avignone III et al. "Experimental search for solar axions via coherent Primakoff conversion in a germanium spectrometer". In: *Phys. Rev. Lett.* 81 (1998), pp. 5068–5071. DOI: 10.1103/PhysRevLett.81.5068. arXiv: astro-ph/9708008 [astro-ph].

[134] R. Bernabei et al. "Search for solar axions by Primakoff effect in NaI crystals". In: *Phys. Lett.* B515 (2001), pp. 6–12. DOI: 10.1016/S0370-2693(01)00840-1.

[135] Z. Ahmed et al. "Search for Axions with the CDMS Experiment". In: *Phys. Rev. Lett.* 103 (2009), p. 141802. DOI: 10.1103/PhysRevLett.103.141802. arXiv: 0902.4693 [hep-ex].

[136] E. Armengaud et al. "Axion searches with the EDELWEISS-II experiment". In: *JCAP* 11 (2013), p. 067. DOI: 10.1088/1475-7516/2013/11/067. arXiv: 1307.1488 [astro-ph.CO].

[137] A. V. Derbin et al. "Constraints on the axion-electron coupling constant for solar axions appearing owing to bremsstrahlung and the Compton process". In: *JETP Lett.* 95 (2012). [Pisma Zh. Eksp. Teor. Fiz.95,379(2012)], pp. 339–344. DOI: 10.1134/S002136401207003X. arXiv: 1206.4142 [hep-ex].

[138] A. Ljubicic et al. "Search for hadronic axions using axioelectric effect". In: *Phys. Lett. B* 599 (2004), pp. 143–147. DOI: 10.1016/j.physletb.2004.08.038. arXiv: hep-ex/0403045.

[139] G. Bellini et al. "Search for Solar Axions Produced in $p(d, {}^3\mathrm{He})\mathrm{A}$ Reaction with Borexino Detector". In: *Phys. Rev.* D85 (2012), p. 092003. DOI: 10.1103/PhysRevD.85.092003. arXiv: 1203.6258 [hep-ex].

[140] P. Belli et al. "Search for Li-7 solar axions using resonant absorption in LiF crystal: Final results". In: *Phys. Lett.* B711 (2012), pp. 41–45. DOI: 10.1016/j.physletb.2012.03.067.

[141] A. V. Derbin et al. "New limit on the mass of 14.4-keV solar axions emitted in an M1 transition in Fe-57 nuclei". In: *Phys. Atom. Nucl.* 74 (2011). [Yad. Fiz.74,620(2011)], pp. 596–602. DOI: 10.1134/S1063778811040041.

[142] A. V. Derbin et al. "Search for resonant absorption of solar axions emitted in an M1 transition in Fe-57 nuclei". In: *JETP Lett.* 85 (2007). [Pisma Zh. Eksp. Teor. Fiz.85,15(2007)], pp. 12–16. DOI: 10.1134/S0021364007010031.

[143] Yu. M. Gavrilyuk et al. "New Constraints on the Axion–Photon Coupling Constant for Solar Axions". In: *JETP Lett.* 107.10 (2018). [Pisma Zh. Eksp. Teor. Fiz.107,no.10,617(2018)], pp. 589–594. DOI: 10.1134/S0021364018100090.

[144] A. V. Derbin et al. "Search for Solar Axions Produced by Primakoff Conversion Using Resonant Absorption by Tm-169 Nuclei". In: *Phys. Lett.* B678 (2009), pp. 181–185. DOI: 10.1016/j.physletb.2009.06.016. arXiv: 0904.3443 [hep-ph].

[145] P. Sikivie. "Experimental Tests of the Invisible Axion". In: *Phys. Rev. Lett.* 51 (1983). [Erratum: Phys. Rev. Lett.52,695(1984)], pp. 1415–1417. DOI: 10.1103/PhysRevLett.51.1415,10.1103/PhysRevLett.52.695.2.

[146] S. J. Asztalos et al. "An Improved RF cavity search for halo axions". In: *Phys. Rev.* D69 (2004), p. 011101. DOI: 10.1103/PhysRevD.69.011101. arXiv: astro-ph/0310042 [astro-ph].

[147] S. J. Asztalos et al. "A SQUID-based microwave cavity search for dark-matter axions". In: *Phys. Rev. Lett.* 104 (2010), p. 041301. DOI: 10.1103/PhysRevLett.104.041301. arXiv: 0910.5914 [astro-ph.CO].

[148] Allen Caldwell et al. "Dielectric Haloscopes: A New Way to Detect Axion Dark Matter". In: *Phys. Rev. Lett.* 118.9 (2017), p. 091801. DOI: 10.1103/PhysRevLett.118.091801. arXiv: 1611.05865 [physics.ins-det].

[149] P. Brun et al. "A new experimental approach to probe QCD axion dark matter in the mass range above 40 μeV". In: *Eur. Phys. J.* C79.3 (2019), p. 186. DOI: 10.1140/epjc/s10052-019-6683-x. arXiv: 1901.07401 [physics.ins-det].

[150] C. W. Fabjan and F. Gianotti. "Calorimetry for particle physics". In: *Rev. Mod. Phys.* 75 (2003), pp. 1243–1286. DOI: 10.1103/RevModPhys.75.1243.

[151] N. E. Booth, B. Cabrera, and E. Fiorini. "Low-temperature particle detectors". In: *Ann. Rev. Nucl. Part. Sci.* 46 (1996), pp. 471–532. DOI: 10.1146/annurev.nucl.46.1.471.

[152] H.E. Hall, P.J. Ford, and K. Thompson. "A helium-3 dilution refrigerator". In: *Cryogenics* 6.2 (1966), pp. 80–88. ISSN: 0011-2275. DOI: https://doi.org/10.1016/0011-2275(66)90034-8. URL: http://www.sciencedirect.com/science/article/pii/0011227566900348.

[153] Dan McCammon. "Thermal equilibrium calorimeters: An Introduction". In: (2005), pp. 1–34. DOI: 10.1007/10933596_1. arXiv: physics/0503045 [physics.ins-det].

[154] B. Alpert et al. "HOLMES - The Electron Capture Decay of ^{163}Ho to Measure the Electron Neutrino Mass with sub-eV sensitivity". In: *Eur. Phys. J.* C75.3 (2015), p. 112. DOI: 10.1140/epjc/s10052-015-3329-5. arXiv: 1412.5060 [physics.ins-det].

[155] L. Gastaldo et al. "The Electron Capture ^{163}Ho Experiment ECHo: an overview". In: *J. Low Temp. Phys.* 176.5-6 (2014), pp. 876–884. DOI: 10.1007/s10909-014-1187-4. arXiv: 1309.5214 [physics.ins-det].

[156] P.C.-O. Ranitzsch et al. "Development of Metallic Magnetic Calorimeters for High Precision Measurements of Calorimetric ^{187}Re and ^{163}Ho Spectra". In: *J. Low Temp. Phys.* 167.5-6 (2012). Ed. by Christian Enss, Andreas Fleischmann, and Loredana Gastaldo, pp. 1004–1014. DOI: 10.1007/s10909-012-0556-0.

[157] Ning Wang et al. "Electrical and thermal properties of neutron-transmutation-doped Ge at 20 mK". In: *Physical Review B* 41 (6 Feb. 1990), pp. 3761–3768. DOI: 10.1103/PhysRevB.41.3761. URL: https://link.aps.org/doi/10.1103/PhysRevB.41.3761.

[158] E. E. Haller. "Isotopically engineered semiconductors". In: *Journal of Applied Physics* 77.7 (1995), pp. 2857–2878. DOI: 10.1063/1.358700. eprint: https://doi.org/10.1063/1.358700. URL: https://doi.org/10.1063/1.358700.

[159] K. D. Irwin. "An application of electrothermal feedback for high resolution cryogenic particle detection". In: *Applied Physics Letters* 66.15 (1995), pp. 1998–2000. DOI: 10.1063/1.113674. eprint: https://doi.org/10.1063/1.113674. URL: https://doi.org/10.1063/1.113674.

[160] Teresa Marrodán Undagoitia and Ludwig Rauch. "Dark matter direct-detection experiments". In: *Journal of Physics G* 43.1 (2016), p. 013001. DOI: 10.1088/0954-3899/43/1/013001. arXiv: 1509.08767 [physics.ins-det].

[161] C. Arnaboldi et al. "CUORE: A Cryogenic underground observatory for rare events". In: *Nucl. Instrum. Meth.* A518 (2004), pp. 775–798. DOI: 10.1016/j.nima.2003.07.067. arXiv: hep-ex/0212053 [hep-ex].

[162] J. M. Lamarre et al. "Planck Pre-Launch Status: The HFI Instrument, from Specification to Actual Performance". In: *Astron. Astrophys.* 520 (2010), A9. DOI: 10.1051/0004-6361/200912975.

[163] Dan McCammon. "Semiconductor thermistors". In: *Appl. Phys.* 99 (2005), pp. 35–61. DOI: 10.1007/10933596_2. arXiv: physics/0503086 [physics.ins-det].

[164] Nahuel Ferreiro Iachellini. "Increasing the sensitivity to low mass dark matter in CRESST-III with a new DAQ and signal processing". PhD thesis. Munich U., 2019. URL: https://edoc.ub.uni-muenchen.de/23762/.

[165] P. A. R. Ade et al. "Antenna-coupled TES bolometers used in BICEP2, Keck array, and SPIDER". In: *Astrophys. J.* 812.2 (2015), p. 176. DOI: 10.1088/0004-637X/812/2/176. arXiv: 1502.00619 [astro-ph.IM].

[166] G. Angloher et al. "Commissioning Run of the CRESST-II Dark Matter Search". In: *Astropart. Phys.* 31 (2009), pp. 270–276. DOI: 10.1016/j.astropartphys.2009.02.007. arXiv: 0809.1829 [astro-ph].

[167] J. Rothe et al. "TES-Based Light Detectors for the CRESST Direct Dark Matter Search". In: *J. Low. Temp. Phys.* 193.5-6 (2018), pp. 1160–1166. DOI: 10.1007/s10909-018-1944-x.

[168] M. Kiefer et al. "In-situ study of light production and transport in phonon/light detector modules for dark matter search". In: *Nucl. Instrum. Meth.* A821 (2016), pp. 116–121. DOI: 10.1016/j.nima.2016.03.035. arXiv: 1503.07806 [astro-ph.IM].

[169] F. Pröbst et al. "Model for cryogenic particle detectors with superconducting phase transition thermometers". In: *Journal of Low Temperature Physics* 100.1 (June 1995), pp. 69–104. ISSN: 1573-7357. DOI: 10.1007/BF00753837. URL: https://doi.org/10.1007/BF00753837.

[170] R. Strauss et al. "A detector module with highly efficient surface-alpha event rejection operated in CRESST-II Phase 2". In: *The European Physical Journal C* 75.8 (2015), p. 352. DOI: 10.1140/epjc/s10052-015-3572-9. arXiv: 1410.1753.

[171] R. Strauss et al. "A prototype detector for the CRESST-III low-mass dark matter search". In: *Nucl. Instrum. Meth.* A845 (2017), pp. 414–417. DOI: 10.1016/j.nima.2016.06.060. arXiv: 1802.08639 [astro-ph.IM].

[172] E. Armengaud et al. "Searching for low-mass dark matter particles with a massive Ge bolometer operated above-ground". In: *Phys. Rev.* D99.8 (2019), p. 082003. DOI: 10.1103/PhysRevD.99.082003. arXiv: 1901.03588 [astro-ph.GA].

[173] Chris Kouvaris and Josef Pradler. "Probing sub-GeV Dark Matter with conventional detectors". In: *Phys. Rev. Lett.* 118.3 (2017), p. 031803. DOI: 10.1103/PhysRevLett.118.031803. arXiv: 1607.01789 [hep-ph].

[174] Rouven Essig et al. "Relation between the Migdal Effect and Dark Matter-Electron Scattering in Isolated Atoms and Semiconductors". In: *Phys. Rev. Lett.* 124.2 (2020), p. 021801. DOI: 10.1103/PhysRevLett.124.021801. arXiv: 1908.10881 [hep-ph].

[175] Tanner Trickle et al. "Multi-Channel Direct Detection of Light Dark Matter: Theoretical Framework". In: *JHEP* 03 (2020), p. 036. DOI: 10.1007/JHEP03(2020)036. arXiv: 1910.08092 [hep-ph].

[176] G. Angloher et al. "Exploring CEνNS with NUCLEUS at the Chooz nuclear power plant". In: *Eur. Phys. J.* C79.12 (2019), p. 1018. DOI: 10.1140/epjc/s10052-019-7454-4. arXiv: 1905.10258 [physics.ins-det].

[177] Luca Pattavina, Nahuel Ferreiro Iachellini, and Irene Tamborra. "RES-NOVA: A new neutrino observatory based on archaeological lead". In: (2020). arXiv: 2004.06936 [astro-ph.HE].

[178] A. V. Derbin et al. "Search for solar axions generated by the Primakoff effect with resonance absorption by 169Tm". In: *Bulletin of the Russian Academy of Sciences: Physics* 74.4 (Apr. 2010), pp. 481–486. ISSN: 1934-9432. DOI: 10.3103/S106287381004012X. URL: https://doi.org/10.3103/S106287381004012X.

[179] A. H. Abdelhameed et al. "First results on sub-GeV spin-dependent dark matter interactions with ^{7}Li". In: *Eur. Phys. J.* C79.7 (2019), p. 630. DOI: 10.1140/epjc/s10052-019-7126-4. arXiv: 1902.07587 [astro-ph.IM].

[180] C. Boehm and Pierre Fayet. "Scalar dark matter candidates". In: *Nuclear Physics B* 683 (2004), pp. 219–263. DOI: 10.1016/j.nuclphysb.2004.01.015. eprint: 0305261.

[181] A. Liam Fitzpatrick et al. "The Effective Field Theory of Dark Matter Direct Detection". In: *Journal of Cosmology and Astroparticle Physics* 1302 (2013), p. 004. DOI: 10.1088/1475-7516/2013/02/004. arXiv: 1203.3542.

[182] E. Aprile et al. "First results on the scalar WIMP-pion coupling, using the XENON1T experiment". In: *Physical Review Letters* 122.7 (2019), p. 071301. DOI: 10.1103/PhysRevLett.122.071301. arXiv: 1811.12482.

[183] D. S. Akerib et al. "Results of a search for sub-GeV dark matter using 2013 LUX data". In: (2018). arXiv: 1811.11241.

[184] K. Miuchi et al. "First results from dark matter search experiment with LiF bolometer at Kamioka underground laboratory". In: *Astroparticle Physics* 19 (2003), pp. 135–144. DOI: 10.1016/S0927-6505(02)00192-5. arXiv: 0204411.

[185] Q. Arnaud et al. "Optimizing EDELWEISS detectors for low-mass WIMP searches". In: *Physical Review D* 97.2 (2018), p. 022003. DOI: 10.1103/PhysRevD.97.022003. arXiv: 1707.04308.

[186] Andriy Kurylov and Marc Kamionkowski. "Generalized analysis of weakly interacting massive particle searches". In: *Physical Review D* 69 (2004), p. 063503. DOI: 10.1103/PhysRevD.69.063503. arXiv: 0307185.

[187] John Ellis and Ricardo A. Flores. "Elastic supersymmetric relic-nucleus scattering revisited". In: *Physics Letters B* 263.2 (1991), pp. 259–266. ISSN: 0370-2693. DOI: https://doi.org/10.1016/0370-2693(91)90597-J.

[188] O.P. Barinova et al. "First test of Li2MoO4 crystal as a cryogenic scintillating bolometer". In: *Nuclear Instruments and Methods in Physics Research Section A: Accelerators, Spectrometers, Detectors and Associated Equipment* 613.1 (2010), pp. 54–57. ISSN: 0168-9002. DOI: https://doi.org/10.1016/j.nima.2009.11.059.

[189] N. Casali et al. "Discovery of the ^{151}Eu α decay". In: *Journal of Physics G* 41 (2014), p. 075101. DOI: 10.1088/0954-3899/41/7/075101. arXiv: 1311.2834.

[190] M. Martinez et al. "Scintillating bolometers for fast neutron spectroscopy in rare events searches". In: *Journal of Physics: Conference Series* 375 (2012), p. 012025. DOI: 10.1088/1742-6596/375/1/012025.

[191] F. A. Danevich et al. "Growth and characterization of a $Li_2Mg_2(MoO_4)_3$ scintillating bolometer". In: *Nuclear Instruments and Methods* 889 (2018), pp. 89–96. DOI: 10.1016/j.nima.2018.01.101. arXiv: 1802.01888.

[192] Juris Meija et al. "Isotopic compositions of the elements 2013 (IUPAC Technical Report)". In: *Pure and Applied Chemistry* 88 (Jan. 2016), pp. 293–306. DOI: 10.1515/pac-2015-0503.

[193] J. I. Collar. "Search for a nonrelativistic component in the spectrum of cosmic rays at Earth". In: *Physical Review D* 98.2 (2018), p. 023005. DOI: 10.1103/PhysRevD.98.023005,10.1103/PHYSREVD.98.023005. arXiv: 1805.02646.

[194] E. Armengaud et al. "Development of ^{100}Mo-containing scintillating bolometers for a high-sensitivity neutrinoless double-beta decay search". In: *Eur. Phys. J.* C77.11 (2017), p. 785. DOI: 10.1140/epjc/s10052-017-5343-2. arXiv: 1704.01758 [physics.ins-det].

[195] R. Agnese et al. "Low-mass dark matter search with CDMSlite". In: *Physical Review D* 97.2 (2018), p. 022002. DOI: 10.1103/PhysRevD.97.022002. arXiv: 1707.01632.

[196] D. S. Akerib et al. "Limits on spin-dependent WIMP-nucleon cross section obtained from the complete LUX exposure". In: *Physical Review Letters* 118.25 (2017), p. 251302. DOI: 10.1103/PhysRevLett.118.251302. arXiv: 1705.03380 [astro-ph.CO].

[197] H. Jiang et al. "Limits on Light Weakly Interacting Massive Particles from the First 102.8 kg $\times$ day Data of the CDEX-10 Experiment". In: *Physical Review Letters* 120.24 (2018), p. 241301. DOI: 10.1103/PhysRevLett.120.241301. arXiv: 1802.09016.

[198] E. Aprile et al. "Constraining the spin-dependent WIMP-nucleon cross sections with XENON1T". In: (2019). arXiv: 1902.03234 [astro-ph.CO].

[199] Changbo Fu et al. "Spin-Dependent Weakly-Interacting-Massive-Particle–Nucleon Cross Section Limits from First Data of PandaX-II Experiment". In: *Physical Review Letters* 118.7 (2017). [Erratum: Phys. Rev. Lett.120,no.4,049902(2018)], p. 071301. DOI: 10.1103/PhysRevLett.120.049902,10.1103/PhysRevLett.118.071301. arXiv: 1611.06553.

[200] C. Amole et al. "Dark Matter Search Results from the Complete Exposure of the PICO-60 C_3F_8 Bubble Chamber". In: (2019). arXiv: 1902.04031.

[201] AF Pacheco and D Strottman. "Nuclear-structure corrections to estimates of the spin-dependent WIMP-nucleus cross section". In: *Physical Review D* 40.6 (1989), p. 2131.

[202] J. D. Lewin and P. F. Smith. "Review of mathematics, numerical factors, and corrections for dark matter experiments based on elastic nuclear recoil". In: *Astroparticle Physics* 6 (1996), pp. 87–112. DOI: 10.1016/S0927-6505(96)00047-3.

[203] Katherine Freese, Mariangela Lisanti, and Christopher Savage. "Colloquium: Annual modulation of dark matter". In: *Reviews of Modern Physics* 85 (2013), pp. 1561–1581. DOI: 10.1103/RevModPhys.85.1561. arXiv: 1209.3339.

[204] Samuel K. Lee, Mariangela Lisanti, and Benjamin R. Safdi. "Dark-Matter Harmonics Beyond Annual Modulation". In: *Journal of Cosmology and Astroparticle Physics* 1311 (2013), p. 033. DOI: 10.1088/1475-7516/2013/11/033. arXiv: 1307.5323.

[205] G. Angloher et al. "Results on MeV-scale dark matter from a gram-scale cryogenic calorimeter operated above ground". In: *The European Physical Journal C* 77.9 (2017), p. 637. DOI: 10.1140/epjc/s10052-017-5223-9. arXiv: 1707.06749 [astro-ph.CO].

[206] L. Cardani et al. "Development of a Li_2MoO_4 scintillating bolometer for low background physics". In: *Journal of Instrumentation* 8 (2013), P10002. DOI: 10.1088/1748-0221/8/10/P10002. arXiv: 1307.0134 [physics.ins-det].

[207] C. M. Lederer et al. "Energy levels of ^{237}Np (I). The alpha decay of ^{241}Am". In: *Nuclear Physics A* 84 (1966), pp. 481–504. DOI: 10.1016/0029-5582(66)91010-8.

[208] T. B. Bekker et al. "Aboveground test of an advanced Li_2MoO_4 scintillating bolometer to search for neutrinoless double beta decay of ^{100}Mo". In: *Astroparticle Physics* 72 (2016), pp. 38–45. DOI: 10.1016/j.astropartphys.2015.06.002.

[209] V. I. Tretyak. "Semi-empirical calculation of quenching factors for ions in scintillators". In: *Astroparticle Physics* 33 (2010), pp. 40–53. DOI: 10.1016/j.astropartphys.2009.11.002. arXiv: 0911.3041.

[210] M. Mancuso et al. "A Low Nuclear Recoil Energy Threshold for Dark Matter Search with CRESST-III Detectors". In: *Journal of Low Temperature Physics* 193.3 (2018), pp. 441–448. ISSN: 1573-7357. DOI: 10.1007/s10909-018-1948-6. URL: https://doi.org/10.1007/s10909-018-1948-6.

[211] S. Yellin. "Finding an upper limit in the presence of unknown background". In: *Physical Review D* 66 (2002), p. 032005. DOI: 10.1103/PhysRevD.66.032005. arXiv: 0203002.

[212] S. Yellin. "Extending the optimum interval method". In: (2007). arXiv: 0709.2701.

[213] D. Kerr F. J.; Lynden-Bell. "Review of galactic constants". In: *Monthly Notices of the Royal Astronomical Society* 221 (1986), pp. 1023–1038. DOI: 10.1093/mnras/221.4.1023.

[214] Torsten Bringmann and Maxim Pospelov. "Novel direct detection constraints on light dark matter". In: *Physical Review Letters* 122.17 (2019), p. 171801. DOI: 10.1103/PhysRevLett.122.171801. arXiv: 1810.10543.

[215] A. H. Abdelhameed et al. "Cryogenic characterization of a $LiAlO_2$ crystal and new results on spin-dependent dark matter interactions with ordinary matter". In: *Eur. Phys. J.* C80.9 (2020), p. 834. DOI: 10.1140/epjc/s10052-020-8329-4. arXiv: 2005.02692 [physics.ins-det].

[216] E. et al. Bertoldo. "Lithium-Containing Crystals for Light Dark Matter Search Experiments." In: *Journal of Low Temperature Physics* 199 (2020), pp. 510–518. DOI: https://doi.org/10.1007/s10909-019-02287-3.

[217] G. Angloher et al. "Results on light dark matter particles with a low-threshold CRESST-II detector". In: *The European Physical Journal C* 76.1 (2016), p. 25. DOI: 10.1140/epjc/s10052-016-3877-3. arXiv: 1509.01515 [astro-ph.CO].

[218] A. Aliane et al. "First test of a Li_2WO_4(Mo) bolometric detector for the measurement of coherent neutrino-nucleus scattering". In: *Nucl. Instrum. Meth.* A949 (2020), p. 162784. DOI: 10.1016/j.nima.2019.162784.

[219] Takayuki Yanagida et al. "Comparative Studies of Optical and Scintillation Properties between $LiGaO_2$ and $LiAlO_2$ Crystals". In: *Journal of the Physical Society of Japan* 86.9 (2017), p. 094201. DOI: 10.7566/JPSJ.86.094201.

[220] J. Engel et al. "Response of mica to weakly interacting massive particles". In: *Physical Review C* 52 (1995), pp. 2216–2221. DOI: 10.1103/PhysRevC.52.2216. arXiv: 9504322 [hep-ph].

[221] B. Cockayne and B. Lent. "The Czochralski growth of single crystal lithium aluminate, LiAlO2". In: *Journal of Crystal Growth* 54.3 (1981), pp. 546–550. ISSN: 0022-0248. DOI: https://doi.org/10.1016/0022-0248(81)90511-X. URL: http://www.sciencedirect.com/science/article/pii/002202488190511X.

[222] R. Bertram and D. Klimm. "Assay measurements of oxide materials by thermogravimetry and ICP-OES". In: *Thermochimica Acta* 419.1 (2004), pp. 189–193. ISSN: 0040-6031. DOI: https://doi.org/10.1016/j.tca.2004.03.003. URL: http://www.sciencedirect.com/science/article/pii/S004060310400108X.

[223] Boža Veličkov et al. "Effects of the Li-evaporation on the Czochralski growth of γ-LiAlO2". In: *Journal of Crystal Growth* 310.1 (2008), pp. 214–220. ISSN: 0022-0248. DOI: https://doi.org/10.1016/j.jcrysgro.2007.09.046. URL: http://www.sciencedirect.com/science/article/pii/S0022024807008317.

[224] R. et al. Strauss. "Energy-dependent light quenching in CaWO4 crystals at mK temperatures." In: *The European Physical Journal C* 74 (2014). DOI: https://doi.org/10.1140/epjc/s10052-014-2957-5.

[225] Strauss et al. "Results of Quenching Factor Measurements of CaWO4 at mK Temperatures for the Direct Dark Matter Search Experiment CRESST." In: *Journal of Low Temperature Physics* 176 (2014), pp. 905–910. DOI: https://doi.org/10.1007/s10909-013-1075-3.

[226] E. Gatti and P. F. Manfredi. "Processing the Signals From Solid State Detectors in Elementary Particle Physics". In: *La Rivista del Nuovo Cimento* 9N1 (1986), pp. 1–146. DOI: 10.1007/BF02822156.

[227] M. Mancuso et al. "A method to define the energy threshold depending on noise level for rare event searches". In: *Nuclear Instruments and Methods in Physics Research Section A* 940 (2019), pp. 492–496. DOI: 10.1016/j.nima.2019.06.030. arXiv: 1711.11459 [physics.ins-det].

[228] E. Aprile et al. "Search for Light Dark Matter Interactions Enhanced by the Migdal effect or Bremsstrahlung in XENON1T". In: *Physical Review Letters* 123.24 (2019), p. 241803. DOI: 10.1103/PhysRevLett.123.241803. arXiv: 1907.12771 [hep-ex].

[229] M. Ambrosio et al. "Vertical muon intensity measured with MACRO at the Gran Sasso Laboratory". In: *Physical Review D* 52 (1995), pp. 3793–3802. DOI: 10.1103/PhysRevD.52.3793.

[230] G. Angloher et al. "Quasiparticle Diffusion in CRESST Light Detectors". In: *Journal of Low Temperature Physics* 184.1-2 (2016), pp. 323–329. DOI: 10.1007/s10909-016-1512-1.

[231] R. Strauss et al. "Beta/gamma and alpha backgrounds in CRESST-II Phase 2". In: *Journal of Cosmology and Astroparticle Physics* 1506.06 (2015), p. 030. DOI: 10.1088/1475-7516/2015/06/030. arXiv: 1410.4188 [physics.ins-det].

[232] R. Strauss et al. "The ν-cleus experiment: A gram-scale fiducial-volume cryogenic detector for the first detection of coherent neutrino-nucleus scattering". In: *The European Physical Journal C* 77 (2017), p. 506. DOI: 10.1140/epjc/s10052-017-5068-2. arXiv: 1704.04320 [physics.ins-det].

[233] E. Bertoldo et al. "A test of bolometric properties of Tm-containing crystals as a perspective detector for a solar axion search". In: *Nucl. Instrum. Meth.* A949 (2020), p. 162924. DOI: 10.1016/j.nima.2019.162924. arXiv: 1905.12952 [physics.ins-det].

[234] Jihn E. Kim. "Weak Interaction Singlet and Strong CP Invariance". In: *Phys. Rev. Lett.* 43 (1979), p. 103. DOI: 10.1103/PhysRevLett.43.103.

[235] Mikhail A. Shifman, A. I. Vainshtein, and Valentin I. Zakharov. "Can Confinement Ensure Natural CP Invariance of Strong Interactions?" In: *Nucl. Phys.* B166 (1980), pp. 493–506. DOI: 10.1016/0550-3213(80)90209-6.

[236] A. R. Zhitnitsky. "On Possible Suppression of the Axion Hadron Interactions. (In Russian)". In: *Sov. J. Nucl. Phys.* 31 (1980). [Yad. Fiz.31,497(1980)], p. 260.

[237] Michael Dine, Willy Fischler, and Mark Srednicki. "A Simple Solution to the Strong CP Problem with a Harmless Axion". In: *Phys. Lett.* 104B (1981), pp. 199–202. DOI: 10.1016/0370-2693(81)90590-6.

[238] A. V. Derbin et al. "Search for resonant absorption of solar axions by atomic nuclei". In: *Bull. Russ. Acad. Sci. Phys.* 71.6 (2007), pp. 832–840. DOI: 10.3103/S1062873807060160.

[239] A. V. Derbin et al. "Constraints on the axion-electron coupling for solar axions produced by Compton process and bremsstrahlung". In: *Phys. Rev.* D83 (2011), p. 023505. DOI: 10.1103/PhysRevD.83.023505. arXiv: 1101.2290 [hep-ex].

[240] E. Arik et al. "Probing eV-scale axions with CAST". In: *JCAP* 0902 (2009), p. 008. DOI: 10.1088/1475-7516/2009/02/008. arXiv: 0810.4482 [hep-ex].

[241] E. Armengaud et al. "Conceptual Design of the International Axion Observatory (IAXO)". In: *JINST* 9 (2014), T05002. DOI: 10.1088/1748-0221/9/05/T05002. arXiv: 1401.3233 [physics.ins-det].

[242] F. T. Avignone et al. "Search for Axions From the 1115-kev Transition of ^{65}Cu". In: *Phys. Rev.* D37 (1988), pp. 618–630. DOI: 10.1103/PhysRevD.37.618.

[243] Shigetaka Moriyama. "A Proposal to search for a monochromatic component of solar axions using Fe-57". In: *Phys. Rev. Lett.* 75 (1995), pp. 3222–3225. DOI: 10.1103/PhysRevLett.75.3222. arXiv: hep-ph/9504318 [hep-ph].

[244] A. V. Derbin et al. "Tm-Containing Bolometers for Resonant Absorption of Solar Axions". In: *Proceedings, 11th Patras Workshop on Axions, WIMPs and WISPs (Axion-WIMP 2015): Zaragoza, Spain, June 22-26, 2015*. 2015, pp. 201–205. DOI: 10.3204/DESY-PROC-2015-02/derbin_alexander.

[245] Jörg Körner et al. "Spectroscopic investigations of thulium doped YAG and YAP crystals between 77 K and 300 K for short-wavelength infrared lasers". In: *Journal of Luminescence* 202 (2018), pp. 427–437. ISSN: 0022-2313. DOI: https://doi.org/10.1016/j.jlumin.2018.05.070. URL: http://www.sciencedirect.com/science/article/pii/S0022231318300024.

[246] John B. Gruber et al. "Spectra and energy levels of Tm^{3+}:$Y_3Al_5O_{12}$". In: *Phys. Rev. B* 40 (14 Nov. 1989), pp. 9464–9478. DOI: 10.1103/PhysRevB.40.9464. URL: https://link.aps.org/doi/10.1103/PhysRevB.40.9464.

[247] C. Arpesella. "A low background counting facility at laboratori nazionali del Gran Sasso". In: *Applied Radiation and Isotopes* 47.9 (1996). Proceedings of the International Committee for Radionuclide Metrology Conference on Low-level Measurement Techniques, pp. 991–996. ISSN: 0969-8043. DOI: https://doi.org/10.1016/S0969-8043(96)00097-8. URL: http://www.sciencedirect.com/science/article/pii/S0969804396000978.

[248] Matthias Laubenstein. "Screening of materials with high purity germanium detectors at the Laboratori Nazionali del Gran Sasso". In: *Int. J. Mod. Phys.* A32.30 (2017), p. 1743002. DOI: 10.1142/S0217751X17430023.

[249] D. Budjas et al. "Highly Sensitive Gamma-Spectrometers of GERDA for Material Screening: Part 2". In: (2007). arXiv: 0812.0768 [physics.ins-det].

[250] Melissa Boswell et al. "MaGe-a Geant4-based Monte Carlo Application Framework for Low-background Germanium Experiments". In: *IEEE Trans. Nucl. Sci.* 58 (2011), pp. 1212–1220. DOI: 10.1109/TNS.2011.2144619. arXiv: 1011.3827 [nucl-ex].

[251] M. Heisel, F. Kaether, and H. Simgen. "Statistical analysis of low-level material screening measurements via gamma-spectroscopy". In: *Applied Radiation and Isotopes* 67.5 (2009). 5th International Conference on Radionuclide Metrology - Low-Level Radioactivity Measurement Techniques ICRM-LLRMT'08, pp. 741–745. ISSN: 0969-8043. DOI: https://doi.org/10.1016/j.apradiso.2009.01.028. URL: http://www.sciencedirect.com/science/article/pii/S0969804309000281.

[252] Fedor A. Danevich et al. "On the alpha activity of natural tungsten isotopes". In: *Phys. Rev.* C67 (2003), p. 014310. DOI: 10.1103/PhysRevC.67.014310. arXiv: nucl-ex/0211013 [nucl-ex].

[253] C. Cozzini et al. "Detection of the natural alpha decay of tungsten". In: *Phys. Rev.* C70 (2004), p. 064606. DOI: 10.1103/PhysRevC.70.064606. arXiv: nucl-ex/0408006 [nucl-ex].

[254] Yu. G. Zdesenko et al. "Scintillation properties and radioactive contamination of $CaWO_4$ crystal scintillators". In: *Nucl. Instrum. Meth.* A538 (2005), pp. 657–667. DOI: 10.1016/j.nima.2004.09.030.

[255] F.A. Danevich et al. "Effect of recrystallisation on the radioactive contamination of CaWO4 crystal scintillators". In: *Nuclear Instruments and Methods in Physics Research Section A: Accelerators, Spectrometers, Detectors and Associated Equipment* 631.1 (2011), pp. 44–53. ISSN: 0168-9002. DOI: https://doi.org/10.1016/j.nima.2010.11.118. URL: http://www.sciencedirect.com/science/article/pii/S0168900210026653.

[256] G. Angloher et al. "Results from the first cryogenic NaI detector for the COSINUS project". In: *Journal of Instrumentation* 12.11 (2017), P11007. URL: http://stacks.iop.org/1748-0221/12/i=11/a=P11007.

[257] *Nuclear Data Services*. https://www-nds.iaea.org/relnsd/vcharthtml/VChartHTML.html.

[258] A. H. Abdelhameed et al. "New limits on the resonant absorption of solar axions obtained with a ^{169}Tm-containing cryogenic detector". In: *Eur. Phys. J.* C80.5 (2020), p. 376. DOI: 10.1140/epjc/s10052-020-7943-5. arXiv: 2004.08121 [hep-ex].

[259] William A. Bardeen and S. -H. H. Tye. "Current Algebra Applied to Properties of the Light Higgs Boson". In: *Phys. Lett.* 74B (1978), pp. 229–232. DOI: 10.1016/0370-2693(78)90560-9.

[260] A V Derbin et al. "Recent Results of Search for Solar Axions Using Resonant Absorption by 83Kr nuclei". In: *Journal of Physics: Conference Series* 934 (Dec. 2017), p. 012018. DOI: 10.1088/1742-6596/934/1/012018. URL: https://doi.org/10.1088%2F1742-6596%2F934%2F1%2F012018.

[261] David B. Kaplan. "Opening the Axion Window". In: *Nucl. Phys.* B260 (1985), pp. 215–226. DOI: 10.1016/0550-3213(85)90319-0.

[262] Mark Srednicki. "Axion Couplings to Matter. 1. CP Conserving Parts". In: *Nucl. Phys.* B260 (1985), pp. 689–700. DOI: 10.1016/0550-3213(85)90054-9.

[263] K. van Bibber et al. "A Practical Laboratory Detector for Solar Axions". In: *Phys. Rev.* D39 (1989), p. 2089. DOI: 10.1103/PhysRevD.39.2089.

[264] R. J. Creswick et al. "Theory for the direct detection of solar axions by coherent Primakoff conversion in germanium detectors". In: *Phys. Lett.* B427 (1998), pp. 235–240. DOI: 10.1016/S0370-2693(98)00183-X. arXiv: hep-ph/9708210 [hep-ph].

[265] K. Zioutas et al. "First results from the CERN Axion Solar Telescope (CAST)". In: *Phys. Rev. Lett.* 94 (2005), p. 121301. DOI: 10.1103/PhysRevLett.94.121301. arXiv: hep-ex/0411033 [hep-ex].

[266] Maxim Pospelov, Adam Ritz, and Mikhail B. Voloshin. "Bosonic super-WIMPs as keV-scale dark matter". In: *Phys. Rev.* D78 (2008), p. 115012. DOI: 10.1103/PhysRevD.78.115012. arXiv: 0807.3279 [hep-ph].

[267] Paolo Gondolo and Georg G. Raffelt. "Solar neutrino limit on axions and keV-mass bosons". In: *Phys. Rev. D* 79 (10 May 2009), p. 107301. DOI: 10.1103/PhysRevD.79.107301. URL: https://link.aps.org/doi/10.1103/PhysRevD.79.107301.

[268] D. Kekez et al. "Search for solar hadronic axions produced by a bremsstrahlung-like process". In: *Phys. Lett.* B671 (2009), pp. 345–348. DOI: 10.1016/j.physletb.2008.12.033. arXiv: 0807.3482 [hep-ex].

[269] T. W. Donnelly et al. "Do Axions Exist?" In: *Phys. Rev.* D18 (1978), p. 1607. DOI: 10.1103/PhysRevD.18.1607.

[270] V. Mateu and A. Pich. "V(us) determination from hyperon semileptonic decays". In: *JHEP* 10 (2005), p. 041. DOI: 10.1088/1126-6708/2005/10/041. arXiv: hep-ph/0509045 [hep-ph].

[271] A. Airapetian et al. "The Beam-charge azimuthal asymmetry and deeply virtual compton scattering". In: *Phys. Rev.* D75 (2007), p. 011103. DOI: 10.1103/PhysRevD.75.011103. arXiv: hep-ex/0605108 [hep-ex].

[272] V. Yu. Alexakhin et al. "The Deuteron Spin-dependent Structure Function g1(d) and its First Moment". In: *Phys. Lett.* B647 (2007), pp. 8–17. DOI: 10.1016/j.physletb.2006.12.076. arXiv: hep-ex/0609038 [hep-ex].

[273] Anja Tanzke. "Low-Threshold Detectors for Low-Mass Direct Dark Matter Search with CRESST-III". Dissertation. München: Technische Universiät München, 2017.

[274] Adrian Ayala et al. "Revisiting the bound on axion-photon coupling from Globular Clusters". In: *Phys. Rev. Lett.* 113.19 (2014), p. 191302. DOI: 10.1103/PhysRevLett.113.191302. arXiv: 1406.6053 [astro-ph.SR].

[275] D. S. Akerib et al. "First Searches for Axions and Axionlike Particles with the LUX Experiment". In: *Phys. Rev. Lett.* 118.26 (2017), p. 261301. DOI: 10.1103/PhysRevLett.118.261301. arXiv: 1704.02297 [astro-ph.CO].

[276] Georg Raffelt and Achim Weiss. "Red giant bound on the axion - electron coupling revisited". In: *Phys. Rev.* D51 (1995), pp. 1495–1498. DOI: 10.1103/PhysRevD.51.1495. arXiv: hep-ph/9410205 [hep-ph].

Acknowledgments

The work presented in this thesis would had never seen the light of the day without the presence and the help of numerous people. I will now try to do my best to mention all of them.
Many thanks to Prof. Dr. Otmar Biebel for offering me his precious time and wise advise throughout all these years of research.
A special thanks to Dr. Federica Petricca, an incredible boss, tough and supportive in the right mix, which helped me to find my way in the intricate quest to explore the unknown.
A thanks to Dr. Stefan Kluth for his precious annual advises.
A thanks from the deep of my heart to Dr. Michele Mancuso, the best mentor I could have desired to meet. Not only you taught me most of the things I know now while treating me as your peer, but you were always keen to engage in new ideas. It was a pleasure spending an endless amount of hours looking after cryostats with you and not even once I felt bored or out of place.
Thanks to Dr. Nahuel Ferreiro-Iachellini for providing a great company in the office and for all the help with my work.
Many thanks to all the other members of the CRESST group in Munich: Abhijit, Ahmed, Antonio, Dieter, Dominik, Franz, Gonzalo, Johannes, Lucia, Philipp, and Raimund. It was a real pleasure working with you all and it always felt like being in a large family.
Thanks also to all the other colleagues, especially the ones working in Gran Sasso with which I had many professional adventures.
A final thanks to all the people from the Max Planck Institute: they all contribute to a great work environment and they organize the best Christmas parties!

In these years living in Munich, I was also blessed as I met people with whom I spent great moments. This is the time to try to thank them all.
Thanks to Matteo Capozi for turning me into a southerner from Ironhill. Thanks to the crew of focaccia nights: Ludovic, Edoardo, Victor, and Giacomo. Thanks to Giovanni for the long drives and even longer conversations. Thanks to the Mancuso family for all the good memories. A special thanks to Sebastian who helped me in multiple occasions and shared many dinners with me. Thanks also to Benedikt with whom I can always have unique conversations about everything. Finally, thanks to Nina and David: you made my last months in Munich truly special.

Per finire, un ringraziamento a mamma e papà, a cui devo tutto. Nonostante la lontananza, vi ho sempre sentito vicini.